

Copyright

by

Bonggu Shim

2006

The Dissertation Committee for Bonggu Shim
certifies that this is the approved version of the following dissertation:

**Time-Resolved Study of Third Harmonic Generation
from Anisotropically Expanding Clusters**

Committee:

Michael C. Downer, Supervisor

John W. Keto

Manfred Fink

Charles Chiu

Michael F. Becker

**Time-Resolved Study of Third Harmonic Generation
from Anisotropically Expanding Clusters**

by

Bonggu Shim, BS

Dissertation

Presented to the Faculty of the Graduate School of

The University of Texas at Austin

in Partial Fulfillment

of the Requirements

for the Degree of

Doctor of Philosophy

The University of Texas at Austin

August 2006

Dedicated to the Memory of my parents and father-in-law who
loved me so much and are in my heart.

Acknowledgments

This work was possible due to many people. Most significantly, I thank my research supervisor Dr. Michael Downer, who has supported me for my graduate work and has guided me in developing my research skills and insight of physics. When I struggled, he gave me nice suggestions (most of his suggestions turned out to be major breakthroughs), waiting patiently. When I had good results, he discussed the results with me for several hours and motivated me to do more. Without his patience, creativity and enthusiasm, this work would be absolutely impossible.

I thank Dr. Todd Ditmire and his student, Gregory Hays. Dr. Ditmire gave me guidance in this research as a true pioneer of the atomic cluster science and his numerous journals about cluster-laser interaction motivated me to do third harmonic generation simulation. I enjoyed a lot working with Gregory Hays. His knowledge and experience about physics, laser science and humor are incorporated in this dissertation and were crucial to our experimental success.

I thank my committee members, Dr. John keto, Dr. Manfred Fink, Dr. Charles Chiu, and Dr. Michael Becker for reading this dissertation carefully and suggestion. Especially, Dr. John keto taught me about vacuum systems and cluster generation when I was a beginning graduate student who had no background in experimental science. I thank to Dr. Boris Breizman, Dr. Alex Arefiev and Dr. Kay Hoffmann for useful discussions and their help.

For my long time colleagues, Rafal Zdagzaj, Nicholas Matlis, Franklin Grigsby,

and Ben Bowes, thank you. We really worked hard during our laser upgrade. I appreciate their help and great suggestions. Thanks to former members of our group, Dr. Andy Rundquist, Dr. Stephen Paul LeBlanc, and Dr. Erhard Gaul for their teaching. For the future generation of our lab, Peng dong and Xiaohui Gao, good luck and you have already shown us a bright future of our lab. I thank to current and former surface group members, Peter Figliozzi, Liangfeng Sun, Dr. Yongqiang An, Jinhee Kwon, Robert Ehlert, Jens Rafaelson, Dr. Ramon Carrilles-Jamies, Dr. Kui Wu, Dr. Daeyoung Lim, Dr. Yingying Jiang, Dr. Mikal Grimes, Dr. Yunsik Lee. I also thank to all the Ditmire's group members for their help and Jack Clifford and machine shop staff for supplying nicely machined equipments.

Special thanks to my undergraduate advisor, Dr. Jae-hyung Lee for giving me courage and recommending me to study abroad here. I have been surrounded by many good people. Thanks to Friday soccer members for great friendship, cold beer time. I also thank countless many friends in physics, especially to Yunpil Shim who was a college-mate and shared an apartment for 4 years here, and to Junkoo Hahn, Dr. Munhun Hong back in Korea for their friendship.

I am deeply grateful to my sisters for their love, support and sacrifice. I also thank to my mother-in-law and bother-in-laws for their support. Finally, I would like to thank Youjung, my wife. For her love, dedication, support and patience, I cannot thank enough.

BONGGU SHIM

The University of Texas at Austin

August 2006

Time-Resolved Study of Third Harmonic Generation from Anisotropically Expanding Clusters

Publication No. _____

Bonggu Shim, Ph.D.

The University of Texas at Austin, 2006

Supervisor: Michael C. Downer

Time-resolved Third Harmonic Generation (THG) from expanding argon gas clusters has been studied. A 400 nm pump ($I_{pump} \sim 1 \times 10^{15}$ W/cm²) beam ionizes a gas jet composed of atomic clusters and residual gases. An 800 nm, 100 fs probe then generates third harmonic radiation from expanding clusters with controlled delays. The measured THG is sharply peaked at earlier delays than broad absorption resonances. Simulations show that the nonlinear susceptibility $\chi^{(3)}$ of the individual clusters and the THG coherence length of the clustered plasma medium are optimized nearly simultaneously as the pre-heated clusters expand, and both contribute to the observed THG enhancement.

We also measured THG anisotropy from expanding clusters. When reso-

nantly enhanced, THG becomes temporarily anisotropic – *i.e.* a probe polarized perpendicular to the pump generates third-harmonic more efficiently than one polarized parallel – thereby characterizing the anisotropy of cluster expansion. By contrast, the linear optical response was isotropic.

The physical mechanisms contributing to enhanced THG are scalable to relativistic probe intensity (limited only by pre-pulses in the laser system) and to high-order harmonic generation extending to the soft x-ray regime.

Contents

Acknowledgments	v
Abstract	vii
List of Tables	xii
List of Figures	xiii
Chapter 1 Introduction	1
Chapter 2 Theory and simulation of third harmonic generation from a clustered jet	7
2.1 Uniformly expanding nano-plasma model	7
2.1.1 Cluster ionization mechanism	8
2.1.2 Cluster heating mechanism	9
2.1.3 Cluster expansion mechanism	11
2.2 Fluid model and empirically modified nano-plasma model	12
2.3 Laser-cluster interaction simulation	15
2.4 Extension to Third Harmonic Generation	20
2.4.1 Theory	20
2.4.2 Simulation	23

Chapter 3	Terawatt laser system	27
3.1	Oscillator, Stretcher, and Regenerative amplifier	27
3.2	Pre-amplifier and Power-amplifier	30
3.3	Compressor	34
Chapter 4	Time-resolved experiment in a clustered jet	39
4.1	Characterization of a supersonic gas jet	39
4.1.1	Empirical parametrization of cluster size	39
4.1.2	Rayleigh scattering measurement	41
4.1.3	Gas jet atomic density measurement	43
4.1.4	Conclusion	48
4.2	Pump-probe absorption and third harmonic generation experiment .	50
4.3	Analysis: comparison with simulation results	62
4.4	Anisotropy of THG from a clustered plasma.	72
Chapter 5	Conclusions and Future experiments	77
Appendix A	Theory of Kerr-lens mode locking	80
A.1	Introduction	80
A.2	KLM zone	81
A.3	Beam size calculation in the oscillator cavity	84
A.4	Conclusion	86
Appendix B	Atomic density and index of refraction in a clustered jet	92
Appendix C	pump-probe experiments using a different nozzle	94
Appendix D	Two-beam second-harmonic generation from a clustered gas jet	100
Bibliography		105

List of Tables

4.1	Ar cluster radius vs backing pressure at $T_0 = 293$ K.	41
4.2	Ar cluster parameters with the backing pressure P_0 from 20 to 60 bars using a conical nozzle (620 μm orifice and $\sim 5^\circ$ half expansion angle)(Ref.[31]). η is the condensation rate, R is the average cluster radius, $\delta R/R$ is the relative width of radius statistical distribution and $N_{\#}$ is the number of atoms per cluster.	41

List of Figures

1.1	Plasma density gradient at the solid surface. Resonantly enhanced field drives strong nonlinear electron motion near the critical surface.	2
1.2	Electric field inside of a dipole cluster.	3
1.3	Cluster expansion and Mie resonance. An initially solid density plasma in a cluster passes through a Mie resonance during expansion and a uniform plasma eventually forms.	4
2.1	Effect of electron temperature dependence on imaginary linear polarizability in calculation of the modified nano-plasma model when a 30 nm radius Ar cluster is irradiated by a single 800nm, 100 fs with intensity 10^{15} W/cm ²	14
2.2	Nano-plasma and modified nano-plasma simulation results of 10 nm Ar cluster subject to 100 fs, 800nm laser with peak intensity 1×10^{16} W/cm ² (a) Laser temporal profile. (b) Electron density. (c) Cluster radius. (d) Electron temperature.	17
2.3	Average charge state of cluster ions. (a) Cluster case which is subject to field ionization + collisional ionization. (b) Gas Ar charge state.	18
2.4	Time evolution of imaginary polarizability of the 10nm cluster. . . .	18

2.5	Simulation results of 30 nm Ar cluster subject to 100 fs, 800nm laser with peak intensity 1×10^{16} W/cm ² (a) Electron density. (b) Electron temperature. (c) cluster imaginary polarizability.	19
2.6	Third harmonic generation mechanism from clusters proposed by Fomyts'kyi <i>et al.</i> [27]. (a) Ion nonuniformity and anharmonic potential growth in the expanding cluster (b) Third harmonic generation from cold electron core oscillation in the cluster.	21
2.7	Calculated time evolution of $ \chi^{(3)} $ and $Im(\gamma(800nm))$ of the gas jet with different clusters, irradiated by 100 fs, 400 nm laser with peak intensity 1×10^{15} W/cm ²	24
2.8	Time evolution of the THG coherence length	25
2.9	Real refractive index of 800nm and 266nm for the 20nm clustered jet.	26
3.1	Kerr-lens modelocked Ti:Sapphire oscillator.	28
3.2	Pulse stretcher.	29
3.3	Regenerative amplifier.	29
3.4	Pre-amplifier and power-amplifier	31
3.5	Calculated pre-amp energy for each pass	32
3.6	Calculated power-amp energy for each pass	33
3.7	Thermal lens compensation calculation in the pre-amplifier. The red lines represent the crystal position. (a) collimated regenerative amplifier output. A diverging lens (f= -20cm) is located at 104.5 cm and a focusing lens (f= 50cm) at 137.3 cm. (b) slowly diverging beam to compensate for the thermal lensing. The focusing lens was moved closer to the diversing lens by 6.8 cm. (c) beam propagation with 35 m focal length thermal lenses in the 6 pass pre-amplifier.	35
3.8	Expanded and collimated pre-amplifier mode. $1/e^2$ diameters are shown in the horizontal and vertical lineout.	36

3.9	Compressor.	37
3.10	Single-shot autocorrelation trace for the pre-amplifier.	37
3.11	Expanded and collimated power-amplifier mode.	38
3.12	Single-shot autocorrelation trace for the power-amplifier.	38
4.1	Backing pressure vs the condensation rate from Table 4.2 [31].	42
4.2	90 ⁰ Rayleigh scattering set-up and scattering CCD image.	43
4.3	Backing pressure vs 90 ⁰ scattering signal. Fit (Red solid curve) scales as $P_0^{2.77}$ and blue dotted curve is the Hagen's prediction	44
4.4	Mach-Zehnder interferometry set-up.	44
4.5	Fringe shift at 600 psi backing pressure using Mach-Zehnder interfer- ometry	45
4.6	(a) Raw phase shift before fitting for 600 psi Ar. (b) Super-Gaussian fitted phase shift for 600 psi Ar. (c) Example super-Gaussian fit for the phase shift.	46
4.7	Cylindrically symmetric gas jet and Abel's transformation. The gas jet flow is normal to the paper.	47
4.8	Gas jet density profile 2.5 mm downstream from the nozzle at various backing pressures.	48
4.9	Two color pump-probe experimental set-up.	50
4.10	Measured pump mode.	51
4.11	Measured probe mode.	52
4.12	(a) THG: three probe (ω) photons are absorbed and one 3ω photon is generated. (b) FWM: two pump (2ω) photons are absorbed and one ω probe photon, one 3ω photon are created.	53
4.13	Non-collinear pump-probe geometry and momentum conservation.	54

4.14	(a) Pump-weak probe THG vs absorption with 20nm average radius clusters. (b) Helium (160 psi) 3ω signal-check with $I_{pump} \sim I_{probe} \sim 8 \times 10^{14}$ W/cm ² . (c) Collinear Helium (200psi) 3ω signal-check. . .	55
4.15	(a) Time-dependent, probe THG from jet of 20nm average radius Ar clusters ionized and heated by pump at intensity 10^{15} W/cm ² , for various probe intensities with parallel pump and probe polarizations. (b) Power law dependence of early THG peak. (c) Power law dependence of delayed THG peak.	57
4.16	Pump-strong probe THG vs absorption with the probe intensity 10^{15} W/cm ²	58
4.17	Pump-probe THG vs absorption with 20nm argon clusters (600 psi backing pressure) at the jet center.	58
4.18	Pump-probe THG vs absorption with 10nm argon clusters (200 psi backing pressure) at the jet center.	59
4.19	Probe mode measurement set-up.	60
4.20	Time-resolved probe refraction measurements from the 20 nm clustered jet. The peak intensity was 1.0×10^{15} W/cm ² for both pump and probe. (a) Beam radius change. (b) Examples of probe modes.	61
4.21	Time-resolved THG spectrum from the 20nm clustered jet. The pump and the probe peak intensity was 1.0×10^{15} W/cm ²	63
4.22	Probe absorption data (open squares) and calculation (red solid curve) when the ratio of monomer/cluster density was 92 % monomers, 8 % clusters.	64
4.23	Ionization rate. Ionization occurs twice in each laser cycle.	66
4.24	Calculation of ionization currents of monomer gases from the gas jet (0.85×10^{18} cm ⁻³ monomer + 0.15×10^{18} cm ⁻³ clustered gas) irradiated by a single 800 nm, 100 fs laser pulse with different intensities.	68

4.25	THG simulation considering both ionization and heating by the probe. (a) Time dependent THG by 800nm probe pulses of indicated intensities. (b) Probe intensity dependence of calculated THG at $\Delta t = 300$ fs.	70
4.26	Time dependent $ J_{3\omega}(L) ^2$ (dashed curve) and $ \chi^{(3)} $ (solid curve) with $I_{probe} = 10^{15}W/cm^2$ and $\Delta t = 300$ fs after the pump excitation ($I_{pump} = 10^{15}W/cm^2$, 400 nm), considering ionization and heating by both pump and probe.	71
4.27	THG anisotropy in hydrodynamically expanding clusters from 600 psi backing pressure with parallel (filled squares) or perpendicular (filled circles) polarizations. Each THG data point represents an average over 100 shots. Probe absorption was same for parallel (open squares) and perpendicular (open circles) pump and probe polarization. Each absorption data point was taken using imaged probe modes onto a CCD camera with 50 shot averages.	74
4.28	THG anisotropy in higher intensities.	74
4.29	Optical Kerr effect measurement set-up.	75
4.30	Kerr effect data.	76
5.1	Phase matching calculation with 80 % of 20 nm radius clusters and 20 % of monomers in $1 \times 10^{18} \text{ cm}^{-3}$ density argon gas jet.	78
5.2	Phase matching calculation with 70 % of 80 nm radius clusters and 30 % of monomers in $1 \times 10^{18} \text{ cm}^{-3}$ density argon gas jet.	79
A.1	Typical Kerr-lens modelocking (KLM) oscillator configuration.	81
A.2	KLM resonator configuration and ABCD matrices for the formula A.2	82
A.3	Distance measurement in the our KLM cavity.	83

A.4	Kerr-Lens Sensitivity calculation for (a) tangential plane and (b) sagittal plane.	83
A.5	(a) CW oval-shape mode (b) Modelocked round mode.	84
A.6	Beam radii for CW and KLM without gain guiding; 0 is the outcoupler position.	87
A.7	Beam radii inside the Kerr medium with the same parameter as in Fig. A.6.	88
A.8	Beam radii for CW and KLM with gain guiding; 0 is the output coupler position.	89
A.9	Beam radii with gain in the forward direction inside the Kerr medium.	90
A.10	Beam radii with gain in the backward direction inside the Kerr medium.	91
C.1	Collinear pump (400nm)-probe (800nm) absorption using a subsonic nozzle. The peak intensity was about 1×10^{16} W/cm ² for pump and 2×10^{16} W/cm ² for probe. Cluster radii were 12, 16, 20 nm for 400, 600, 800 psi backing pressures.	95
C.2	Collinear pump (400nm)-probe (800nm) 3ω measurements. (a) Ar cluster (800psi) 3ω measurement shows a wide temporal peak near at $\Delta t = 0$. The peak is combination of Third Harmonic Generation (THG), Four Wave Mixing (FWM), and Sum Frequency Generation (SFG). The peak intensity was 1.5×10^{14} W/cm ² for pump and 1.5×10^{13} W/cm ² for probe. (b) Reference Helium (800 psi-unclustering gas) FWM signal near at $\Delta t = 0$. The peak intensity was 5×10^{13} W/cm ² for 400nm and 1×10^{13} W/cm ² for 800nm.	96
C.3	Noncollinear pump (400nm)-probe (800nm) geometry to separate FWM, SFG, and THG signals spatially using momentum conservation. . . .	97
C.4	Noncollinear THG pump intensity scan results using Ar clusters (800 psi).	98

D.1	Two-beam SHG experimental set-up using glass samples. Both fundamental beam (800 nm, 100 fs) intensity was 5×10^{11} W/cm ² . . .	101
D.2	Position scan of two-beam SHG using glass samples. (a) 0.9 mm corning glass sample. (b) 3 mm unknown glass sample.	102
D.3	Two-beam SHG spectrum from a glass sample (blue curve) and 24 nm radius argon clusters (red curve). Ar lamp emission lines (black curve) compares fluorescence from Ar clusters. Both fundamental beam (800 nm, 100 fs) intensity was 3×10^{13} W/cm ² . For SHG from the glass sample, we used the fundamental intensity at 5×10^{11} W/cm ²	103

Chapter 1

Introduction

High-order Harmonic generation (HHG) has been an active research area because it provides a source of ultrafast coherent radiation from near ultraviolet to soft x-ray pulses. High-order harmonics can be generated from monomer gases [1, 2, 3], solid surfaces [4, 5], and atomic clusters [6].

Monomer gas targets have been widely used to produce coherent, collimated odd-harmonic radiation [7, 8] with pulse durations as short as 100 attoseconds [9]. Harmonic generation in gas targets occurs when ionized electrons, oscillating for a fraction of an optical cycle in an intense laser field, collide with the parent ion during their return motion [10, 11]. The low conversion efficiency below 30 nm ($\leq 10^{-7}$) [3], however, has inhibited widespread applications and spurred continuing research into methods to improve conversion efficiency. Harmonics from a solid target plasma have been generated with relatively high efficiency ($10^{-4} - 10^{-5}$) at lower energies (~ 200 nm) [4]. In this case, harmonic generation is caused by strong nonlinear electron motion near the critical surface where the driving laser frequency (ω) matches the plasma frequency (ω_p) [5]. The incident laser pulse penetrates the sharp surface density gradient, created by its leading edge or a pre-pulse, then reaches the critical surface where it resonantly drives electrons [12] (Figure 1.1). But the solid target

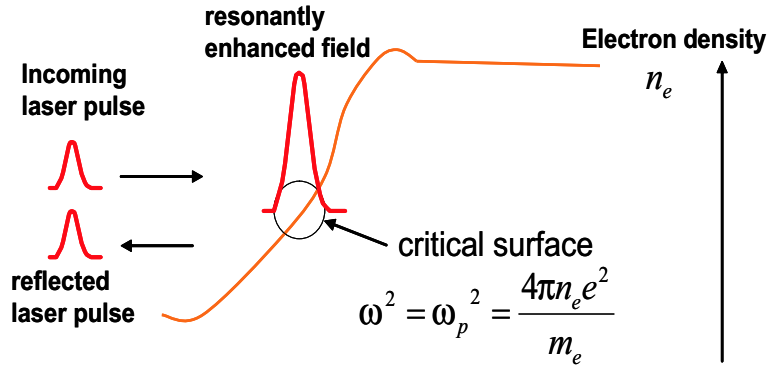


Figure 1.1: Plasma density gradient at the solid surface. Resonantly enhanced field drives strong nonlinear electron motion near the critical surface.

leaves debris which can potentially damage optics in the target chamber. Moreover HHG from it has limited spatial coherence [4]. Finally, interaction is limited to a skin depth, thus precluding any possibility of harmonic growth over an extended interaction length.

Atomic clusters can form in subsonic and supersonic gas jets backed by high pressure following adiabatic expansion into a vacuum chamber and subsequent cooling and condensation [13]. These Van der Waals bonded clusters, containing $10^2 - 10^7$ atoms, provide clean targets with local solid density, but leave negligible debris after laser interaction and enable extended interaction length. Donnelly *et al.* [6] first observed that harmonics from atomic clusters could be generated to higher order, and with less saturation, than from a monomer gas plasma. They attributed these properties to the local solid (multiple-well) potential experienced by an electron in a cluster. However, overall efficiency of harmonic generation by a single short laser pulse was no greater than from the corresponding monomer gas of equivalent average density. Moreover a single pulse provides no means of controlling the harmonic generation process.

In subsequent research, the expansion dynamics of clusters following laser

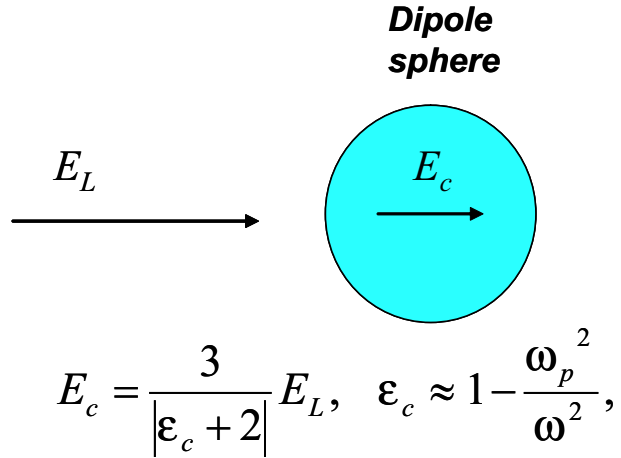


Figure 1.2: Electric field inside of a dipole cluster.

excitation was explored using two pulse pump-probe experiments. In part to interpret such experiments, Ditmire *et al.* [14] developed the uniformly expanding nano-plasma model in which the cluster is treated as a spherical dipole plasma because its radius is smaller than a laser wavelength. For a uniform cluster, the field inside is then given by [15],

$$E_c = \frac{3E_L}{|\epsilon_c + 2|}, \quad (1.1)$$

where E_L is the driving laser field and $\epsilon_c \simeq 1 - \omega_p^2/\omega^2$ is the dielectric constant of the ionized cluster (see Figure 1.2). Upon ionization, the plasma frequency initially exceeds the optical frequency because of the high electron density, so, the interior of the cluster is shielded from the laser field by a large dielectric constant. As the cluster expands by Coulomb explosion (for fully-ionized clusters) and/or hydrodynamic pressure (for slightly-ionized clusters), the plasma frequency decreases and eventually passes through a Mie resonance ($\epsilon_c \simeq -2$). Instead of $\omega_p \simeq \omega$ as in an extended solid target, the resonance of a dipole cluster occurs when $\omega_p \simeq \sqrt{3}\omega$ because of the spherical geometry (Figure 1.3). This model has successfully explained resonances of linear absorption, scattering [16, 17] and production of high energy ions [18] and

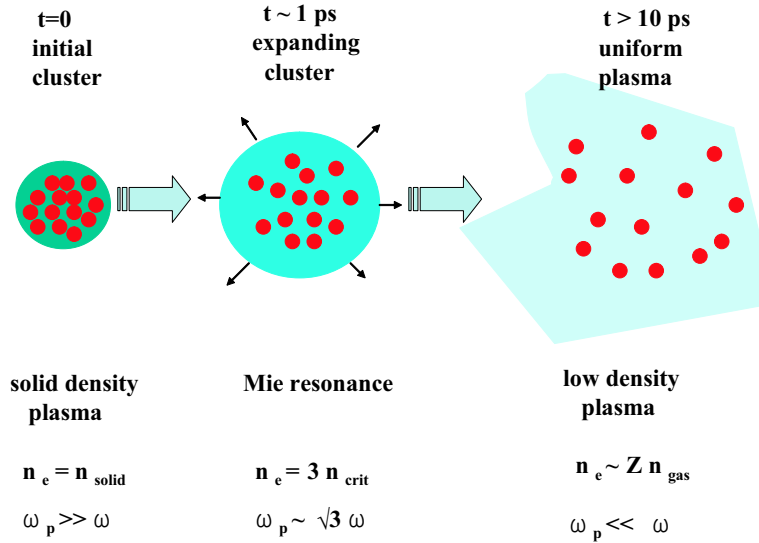


Figure 1.3: Cluster expansion and Mie resonance. An initially solid density plasma in a cluster passes through a Mie resonance during expansion and a uniform plasma eventually forms.

electrons [19] in expanding clusters. However, a shortcoming of the model is that it predicts a much shorter duration absorption and scattering resonance than is observed. In addition, prior to the present work, no pump-probe measurements of nonlinear optical dynamics were available to compare with this model.

Later, a more sophisticated hydrodynamic model by Milchberg *et al.* [20] showed that cluster expansion is nonuniform. In particular, an electron density gradient forms inside the cluster during expansion. Then, the Mie resonance resembles the case of a solid surface ($\omega \simeq \omega_p$). The electric field inside the cluster is also nonuniform, and particularly sharply enhanced near the critical surface. A ponderomotive force in the cluster pushes the electron and ion plasma away from the resonance region and slows cluster expansion. As a result, the resonance lasts longer than predicted by the uniformly expanding model. This model explained the linear optical properties of hydrodynamically expanding clusters more accurately than the

uniform density model [21, 22].

Despite shortcomings, the uniformly expanding nano-plasma model remains attractive because of its simplicity. Recently, a modified model that retains uniform density, but modifies the electron-ion collisional frequency and the cluster ion mass empirically to fit the cluster polarizability data, was proposed [23, 24]. This model correctly yields a slow Mie resonance, consistent with observations and with the hydrodynamic model of Milchberg *et al.* [20]. Because of its computational simplicity, this model more easily analyzes experiments that involve extended time delays (several ps) and/or modifications (focusing, defocusing) to pulse propagation through the clustered plasma than the fully hydrodynamic model.

Meanwhile, the theory of nonlinear optical response of clustered plasmas has recently advanced significantly. Clustered plasmas were proposed theoretically as a unique nonlinear medium in which *both* phase-matching [25, 26] *and* resonantly-enhanced odd-order ($n = 3, 5, \dots$) nonlinear susceptibility $\chi^{(n)}$ [27, 28] (nonlinear Mie resonance) could be achieved at selected cluster sizes and densities. Ion and/or electron density nonuniformity must develop for the nonlinear resonance to occur. Moreover to achieve phase-matching, residual monomer gas plasma must accompany the clustered plasma. Controlled resonance enhancement of the complex *linear* susceptibility $\chi^{(1)}$ (linear resonance) was demonstrated [16, 21] by pre-expanding clusters with an ionizing/heating pulse, and explained using models of exploding clustered plasma [14, 20]. However, experiments that achieved nonlinear resonance and/or phase-matching have not yet been realized.

The motivation of this research is to verify the third harmonic Mie resonance in the expanding nano-clusters and to check the possible phase-matching of THG from a gas jet plasma composed of ionized clusters and residual gas. This study will suggest a path to controlled enhancement of n^{th} -order harmonic generation, since $\chi^{(n)}$ undergoes an analogous resonant enhancement during cluster expansion, while

simultaneous variations in $\chi^{(1)}$ can potentially optimize phase-matching. We also report that, while resonantly enhanced, THG becomes temporarily anisotropic, – *i.e.* a probe polarized perpendicular to the pump generates third-harmonic more efficiently than one polarized parallel – thus demonstrating the anisotropy of cluster expansion [29]. The linear optical response, by contrast, is isotropic within experimental error. This THG anisotropy suggests that perpendicular pump and probe polarizations will also generate more efficient high harmonics from exploding clusters.

Chapter 2

Theory and simulation of third harmonic generation from a clustered jet

In this chapter, I discuss the theory and simulation of laser-cluster interaction based on the uniformly expanding nano-plasma model [14] and empirically modified nano-plasma model [23]. I developed a self-consistent THG computer code using the Runge-Kutta method with an adaptive stepsize control [30] based on these models. Gas jet measurements and simulations discussed in Chapter 4 show that the jet plume is composed of mostly unclustered Ar gases ($\sim 80\%$) [31]. Therefore, I included the THG contribution from unclustered monomers in the code.

2.1 Uniformly expanding nano-plasma model

The uniformly expanding nano-plasma model first proposed by Ditmire *et al.* [14] has successfully explained several experimental results [16, 17, 18, 19, 32]. There are three key mechanisms in this model : (1) Ionization (Optical field and collisional

ionization), (2) Cluster heating (Inverse Bremsstrahlung) and (3) Cluster expansion (hydrodynamic expansion and Coulomb explosion).

2.1.1 Cluster ionization mechanism

The first mechanism is optical field ionization which generates seed electrons for further collisional ionization. With our experimental condition ($I_{pump} \sim 1 \times 10^{15}$ W/cm²), tunneling ionization is important and takes place at the cycle-averaged tunneling rate derived by Ammosov, Delone and Krainov (ADK) [33, 14],

$$W_{ADK} = \frac{\omega_a (2l+1)(l+|m|)!}{2 \cdot 2^{|m|} |m|! (l+|m|)!} \left(\frac{2e}{n^*}\right)^{2n^*} \frac{1}{2\pi n^*} \frac{I_p}{I_h} \left[2\left(\frac{I_p}{I_h}\right)^{1.5} \frac{E_a}{E_0}\right]^{2n^*-|m|-1} \times \exp\left[-\frac{2}{3}\left(\frac{I_p}{I_h}\right)^{1.5} \frac{E_a}{E_0}\right], \quad (2.1)$$

where ω_a is the atomic frequency (4.1×10^{16} s⁻¹), l is the angular momentum and m the magnetic quantum numbers of electronic state from which the electron is removed, I_p is the ionization potential in eV, I_h is the ionization potential of hydrogen (13.6 eV), n^* is the effective principal number ($n^* = Z(I_p/I_h)^{-0.5}$), Z is the charge state of an ionized ion, E_a is the atomic electric field (5.1×10^9 V/m), and E_0 is the laser electric field.

Once seed electrons are formed by field ionization, collisional ionization grows because of local solid density in the cluster. There are two collisional ionization mechanisms. First, inelastic collisions between ions and thermalized electrons induce ionization. The impact ionization rate is given by Lotz' formula [34]

$$W_{thermal} = (3 \times 10^{-6}) n_e \frac{q_i}{I_p (kT_e)^{1/2}} \int_{I_p/kT_e}^{\infty} \frac{e^{-x}}{x} dx, \quad (2.2)$$

where n_e is the electron density in cm⁻³, q_i is the number of electrons in the outer shell of ions, and kT_e is the electron temperature. Second, electrons driven by the

intense laser pulse collide with ions and ionize them. This cycle-averaged rate is

$$W_{laser} = n_e \frac{a_i q_i}{2\pi I_p (m_e U_p)^{1/2}} \left[\left(3 + \frac{I_p}{U_p} + \frac{3}{32} \left(\frac{I_p}{U_p} \right)^2 \right) \ln \left(\frac{1 + \sqrt{1 - I_p/2U_p}}{1 - \sqrt{1 - I_p/2U_p}} \right) - \left(\frac{7}{2} + \frac{3I_p}{8U_p} \right) \sqrt{1 - I_p/2U_p} \right], \quad (2.3)$$

where a_i is an experimentally determined constant equal to $4.5 \times 10^{-14} \text{ cm}^2 \text{ eV}^2$, m_e is the electron mass, and $U_p = e^2 E_c^2 / 4m_e \omega^2$ is the ponderomotive energy of the laser. The formula is valid only for $2U_p > I_p$. These collisional ionization mechanisms quickly produce an overdense clustered plasma even with modest laser intensity ($\gtrsim 10^{14} \text{ W/cm}^2$).

2.1.2 Cluster heating mechanism

Electron heating by the laser is dominated by inverse Bremsstrahlung (collisional heating). The cycle averaged heating rate per unit volume for the cluster is

$$\frac{\partial U}{\partial t} = \frac{\omega}{8\pi} \text{Im}(\varepsilon_c) |E_c|^2, \quad (2.4)$$

where ω is the driving laser frequency, ε_c is the cluster dielectric constant, and E_c is the laser field in the cluster (Eq. 1.1) For the dielectric constant, the Drude model for a plasma was used

$$\varepsilon_c = 1 - \frac{\omega_p^2}{\omega(\omega + i\nu)}, \quad (2.5)$$

where ω_p is the cluster plasma frequency ($\omega_p = \sqrt{4\pi n_e e^2 / m_e}$), and ν is the electron-ion collisional frequency. Then, the heating rate becomes

$$\begin{aligned} \frac{\partial U}{\partial t} &= \frac{9\omega^2 \omega_p^2 \nu}{8\pi} \frac{E_L^2}{9\omega^2(\omega^2 + \nu^2) + \omega_p^2(\omega_p^2 - \nu^2)} \\ &= \frac{9}{8\pi} E_L^2 \frac{(\omega_p/\omega)^2 \nu}{\left((\omega_p/\omega)^2 - 3 \right)^2 + (3\nu/\omega)^2}. \end{aligned} \quad (2.6)$$

The equation shows that the resonance occurs when $\omega_p = \sqrt{3}\omega$. Here, the electron-ion collisional frequency (ν) is an important parameter because it determines the rate of heating of electrons and the temporal width of the resonance. For example, near the resonance, the Eq. 2.6 is proportional to $1/\nu$, therefore, a larger collisional frequency gives a smaller and broader resonance curve.

Ditmire *et al.* [14] used the collisional frequency with the Standard Coulomb formulas of Silin [35]

$$\begin{aligned}\nu &= \frac{4}{9} \sqrt{\frac{2\pi}{3}} \frac{Z^2 e^4 n_i}{m_e^{1/2} (kT_e)^{3/2}} \ln \Lambda, & v_{osc} \ll v_{kT_e} \\ \nu &= \frac{16Z^2 e n_i m_e \omega^3}{E_0^3} \left(\ln \left[\frac{e E_0}{2m_e \omega v_{kT_e}} \right] + 1 \right) \ln \Lambda, & v_{osc} \gg v_{kT_e}\end{aligned}\quad (2.7)$$

where n_i is the ion density in the cluster, v_{osc} is the quiver velocity of electrons, v_{kT_e} is the thermal velocity of electrons, and $\ln \Lambda$ is the Coulomb logarithm. For the intermediate case when $v_{osc} \approx v_{kT_e}$, the numerical integration of the general equation in Ref [35] was used. Zweiback *et al.* [17] used the weak field limit of Silin's formula (*i.e.* Spitzer's formula) [36]

$$\nu = 2 \times 10^{-6} \frac{Z n_e \ln \Lambda}{(kT_e)^{3/2}}, \quad (2.8)$$

in the uniformly expanding plasma model. The shortcoming of this formula is that it predicts somewhat narrowly-peaked resonances, which are not observed in large clusters. I will discuss this further when I present the empirically modified nanoplasma model and simulation [23] in the Section 2.2 and 2.3.

2.1.3 Cluster expansion mechanism

There are two mechanisms for cluster expansion. First, hydrodynamic expansion is driven by hot electron pressure in the cluster. The heated electrons start to expand, then pull the heavy ions. The ideal gas equation gives electron pressure

$$P_e = n_e k T_e, \quad (2.9)$$

where n_e is the electron density in the cluster, and kT_e is the electron temperature of the cluster electrons. Second, Coulomb explosion is driven by charge build-up in the cluster. After ionization, some hot electrons escape the Coulomb barrier formed by ions, leaving a net positive charge in the cluster. The resulting repulsive Coulomb force cause the cluster to expand. The Coulomb pressure is

$$P_{Coul} = \frac{Q^2 e^2}{8\pi r_c^4}, \quad (2.10)$$

where r_c is the cluster radius, and Q is the built-up charge in the cluster due to electron escape. Then, the cluster radius equation becomes

$$\frac{\partial^2 r_c}{\partial^2 t} = 3 \left(\frac{P_e + P_{Coul}}{n_i m_i} \right) \frac{1}{r_c}, \quad (2.11)$$

where n_i is the ion density in the cluster, m_i is the ion mass.

To calculate the accumulated charge (Q) in the cluster, the free stream rate of electrons was calculated using [14]

$$W_{FS} = n_e \frac{2\sqrt{2\pi}}{\sqrt{m_e k T_e}} (K_{esc} + k T_e) \exp\left(-\frac{K_{esc}}{k T_e}\right) \times \begin{cases} \frac{\lambda_e}{4r_c} (12r_c^2 - \lambda_e^2) & \text{for } \lambda_e < 2r_c \\ 4r_c^2 & \text{for } \lambda_e > 2r_c, \end{cases} \quad (2.12)$$

where λ_e is the mean free path

$$\lambda_e = \frac{(kT_e)^2}{4\pi n_e e^4 (Z+1) \ln\Lambda}, \quad (2.13)$$

K_{esc} is the minimum kinetic energy for the electron to escape from the cluster:

$$K_{esc} = \frac{(Q+1)e^2}{r_c}. \quad (2.14)$$

During cluster expansion, the electron thermal energy is converted to kinetic energy. As a result, electron temperature decreases at the rate

$$\frac{\partial T_e}{\partial t} = -2 \frac{T_e}{r_c} \frac{\partial r_c}{\partial t}. \quad (2.15)$$

2.2 Fluid model and empirically modified nano-plasma model

After the nano-plasma was proposed by Ditmire *et al.* [14] and successfully applied to experiments, Milchberg *et al.* [20] developed the hydrodynamic fluid model in which electron density becomes nonuniform in the cluster during expansion. According to the fluid model, the optical field inside an expanding cluster like that at a solid surface, becomes resonantly enhanced only at the critical surface ($\omega \simeq \omega_p$) (see Fig. 1.1), not uniform throughout the cluster. In this case, the nonlinear ponderomotive force (F_P)

$$F_P = -\frac{e^2}{4m_e\omega^2} \frac{\partial |E_c(r)|^2}{\partial r}, \quad (2.16)$$

where $E_c(r)$ is the spatially varying electric field inside the cluster, and r is the radial coordinate, becomes important. This force does not depend on the sign of charge because of the e^2 term and, therefore, pushes both electrons and ions away from

the resonance region [20, 12]. As a result, expansion is slower and resonance longer-lasting than predicted by the nano-plasma model. Experimental results [21, 22] were quantitatively analyzed using this model.

Nevertheless, the hydrodynamic fluid model is computationally intensive. Therefore, as an intermediate approach, Gupta *et al.* [23] developed the empirically modified nano-plasma model which maintained uniform density inside the cluster, but compensated for errors in the time scale of Mie resonances by empirically adjusting the electron-ion collisional frequency (ν) and the ion mass (m_i) to match the linear polarizability predicted by the fluid code. The empirically found electron-ion collisional frequency is

$$\nu = 15 \frac{\omega}{T_e^{1/4}}, \quad (2.17)$$

where T_e is the electron temperature in the cluster in eV , and ω is the optical frequency of the driving laser pulse. Upon laser excitation, the electron temperature rises sharply ($T_e \geq 1keV$) because of the efficient absorption of laser energy by the clusters. The Spitzer collision frequency (Eq. 2.8) used in the nano-plasma model depends more strongly than Eq. 2.17 on the electron temperature ($\nu \propto T_e^{-1.5}$). As a result, the dielectric function (Eq. 2.5) sweeps more quickly through Mie resonances than observed as the clusters evolve. However the modified collision frequency (Eq. 2.17) slows the sweep through Mie resonances, in better agreement with experiments and the fluid model.

I varied Eq. 2.17 by changing the temperature dependence and ran a simulation to check the effect (Simulation results are discussed in detail in Section 2.2). Fig. 2.1 is an example calculation of imaginary linear polarizability of a 30nm cluster related to laser absorption (see Eq. 2.23) when it is irradiated by a single 800 nm, 100 fs pulse with intensity 10^{15} W/cm². The collision frequency with stronger dependence on the electron temperature (*e.g.* $\nu = 15 \frac{\omega}{T_e^{1/2}}$) shows larger polarizability and more delayed linear Mie resonance. However small variation in

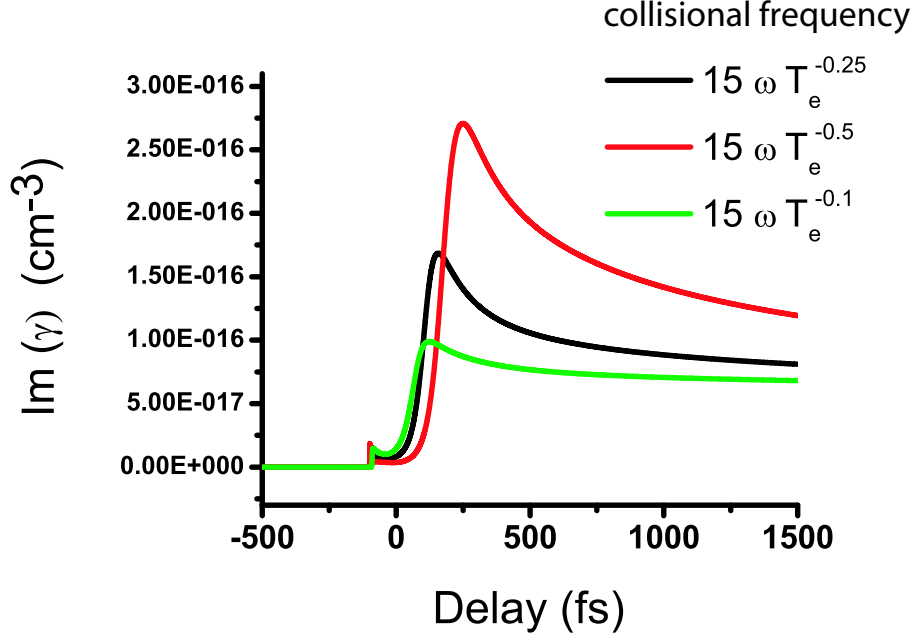


Figure 2.1: Effect of electron temperature dependence on imaginary linear polarizability in calculation of the modified nano-plasma model when a 30 nm radius Ar cluster is irradiated by a single 800nm, 100 fs with intensity 10^{15} W/cm 2 .

the temperature dependence (*e.g.* $T_e^{-0.3}$ instead of $T_e^{-0.25}$) should equally work and simulation results would not deviate much from those of the hydrodynamic model. Finally, Gupta *et al.* modified the cluster radius expansion equation Eq. 2.11 to

$$\frac{\partial^2 r_c}{\partial^2 t} = 5 \left(\frac{P_e}{n_i m_i} \right) \frac{1}{r_c}, \quad (2.18)$$

dropping the Coulomb pressure P_{Coul} , as appropriate for a quasi-neutral cluster. Except for the modification in the collisional frequency, their empirical adjustments only affect the time a Mie resonance occurs and the resonance width, not the magnitude of cluster polarizability.

2.3 Laser-cluster interaction simulation

Here I present self-consistent simulation results using the nano-plasma and modified nano-plasma models. The ionization equations are

$$\frac{\partial N_i}{\partial t} = -W_i N_i + W_{i-1} N_{i-1}, \quad (2.19)$$

$$\frac{\partial N_e}{\partial t} = \sum_i i \frac{\partial N_i}{\partial t} - W_{FS}, \quad (2.20)$$

$$Z = \frac{\sum_i i N_i}{\sum_i N_i}, \quad (2.21)$$

where N_i is the number of ions of the i th charge state in the cluster, $W_i = W_{ADK} + W_{thermal} + W_{laser}$ is the ionization rate from the i th charge state to the $(i + 1)$ th charge state, N_e is the electron number in the cluster, W_{FS} is the electron escape rate (see Eq. 2.12), and Z is the average charge state of the cluster ions.

The electron temperature equation is [14, 37]

$$\frac{\partial T_e}{\partial t} = \frac{2}{3} \frac{1}{n_e} \frac{\omega}{8\pi} \text{Im}(\varepsilon_c) |E_c|^2 - 2 \frac{T_e}{r_c} \frac{\partial r_c}{\partial t} - \frac{T_e - T_i}{\tau_{eq}} - \frac{W_{FS} T_e}{N_e}, \quad (2.22)$$

where n_e is the electron density in the expanding cluster, T_i is the ion temperature, and τ_{eq} is the electron-ion equilibrium time ($\tau_{eq} = \frac{3m_e m_i}{8\sqrt{2} n_i Z^2 e^2 \ln \Lambda} \left(\frac{kT_e}{m_e} + \frac{kT_i}{m_i} \right)^{3/2}$). Here, the first term is inverse Bremsstrahlung (Eq. 2.4), the second term is loss from cluster expansion, the most important cooling mechanism, the third term is the heat transfer from electrons to ions, and the last term is energy loss from hot electron escape. The cluster radius expansion term is evaluated using Eq. 2.11.

I solved the coupled differential equations numerically using the Runge-Kutta adaptive step size control method for computational accuracy and efficiency [30]. For the nano-plasma model, I used the Spitzer formula (see Eq. 2.8) and put the upper limit at twice the laser frequency ($\nu \leq 2\omega$) because electrons in the cluster collectively oscillate in the strong laser field, therefore it is not reasonable to have

collisional frequency much larger than the driving laser frequency [14]. For the modified model, I used Eq. 2.17 for the electron-ion collision frequency and 100 a.m.u. for the ion mass to match our absorption data, which will be presented in Chapter 4. I assumed $T_e = 10 \text{ eV}$ and $T_i = 0 \text{ eV}$ for the initial electron and ion temperatures.

Fig. 2.2 shows a sample calculation of several cluster parameters. A 10 nm radius cluster was irradiated by a single 100 fs, 800 nm laser pulse with peak intensity $1 \times 10^{16} \text{ W/cm}^2$. Black solid curves show the calculation from the nano-plasma model and red dotted curves show calculation from the modified nano-plasma model. As is shown in Fig. 2.2(b), the clustered plasma forms quickly as the laser intensity exceeds the Ar ionization threshold ($I_{th} \sim 1 \times 10^{14} \text{ W/cm}^2$). When ionization saturates and the cluster expands (Fig. 2.2(c)), the electron density (n_e) reaches the resonance condition $n_e/n_{crit} \simeq 3$ with critical density $n_{crit} = m_e \omega^2 / 4\pi e^2$. At this point, the coupling between the cluster and the laser becomes strong, and inverse Bremsstrahlung generates hot electrons in the cluster (Fig. 2.2(d)). As discussed, the nano-plasma model predicts a sharper and narrower resonance than the modified model.

Because of strong collisional ionization, the average ion charge state inside the cluster ($Z \geq 10$) greatly exceeds that predicted only by ADK field ionization ($Z \sim 6$) at peak intensity $1 \times 10^{16} \text{ W/cm}^2$ (Fig. 2.3).

Fig. 2.4 shows the imaginary part of cluster polarizability

$$\gamma^{(1)} = \text{Im}\left(\frac{\varepsilon_c - 1}{\varepsilon_c + 2}\right)r_c^3, \quad (2.23)$$

which determines the laser absorption by clusters in the jet. The nano-plasma model calculation shows a very narrow resonance peak like the electron temperature, which is not observed in experiments. By contrast, the modified model correctly yields a much broader resonance.

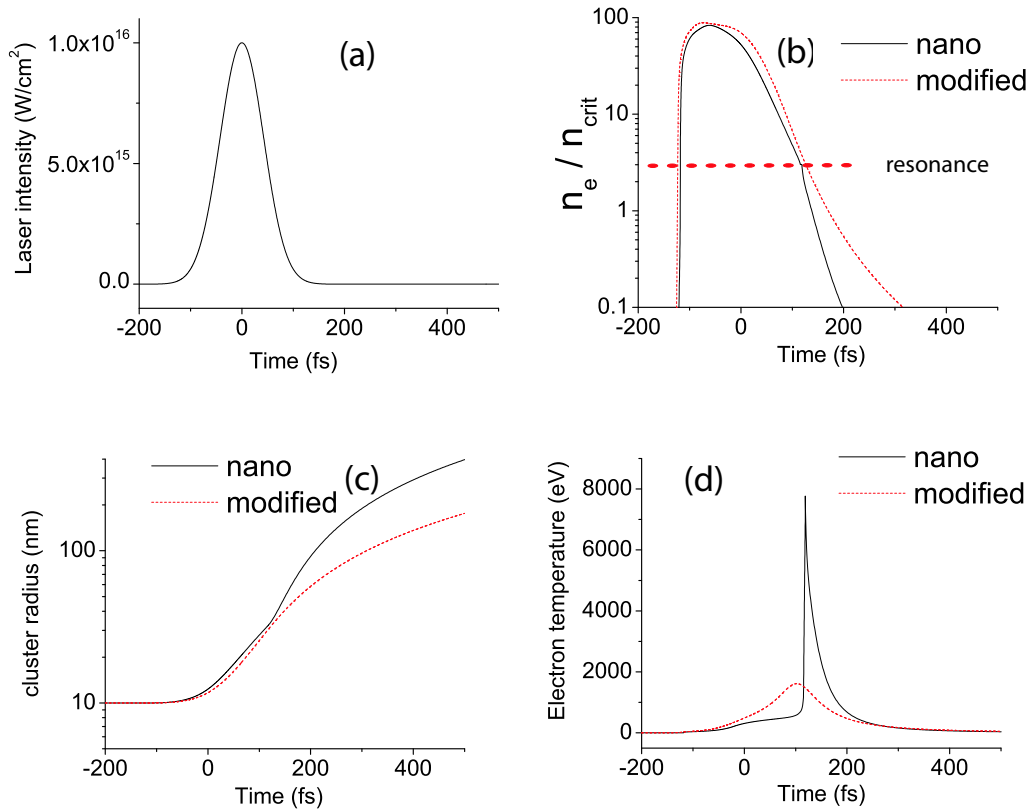


Figure 2.2: Nano-plasma and modified nano-plasma simulation results of 10 nm Ar cluster subject to 100 fs, 800nm laser with peak intensity 1×10^{16} W/cm² (a) Laser temporal profile. (b) Electron density. (c) Cluster radius. (d) Electron temperature.

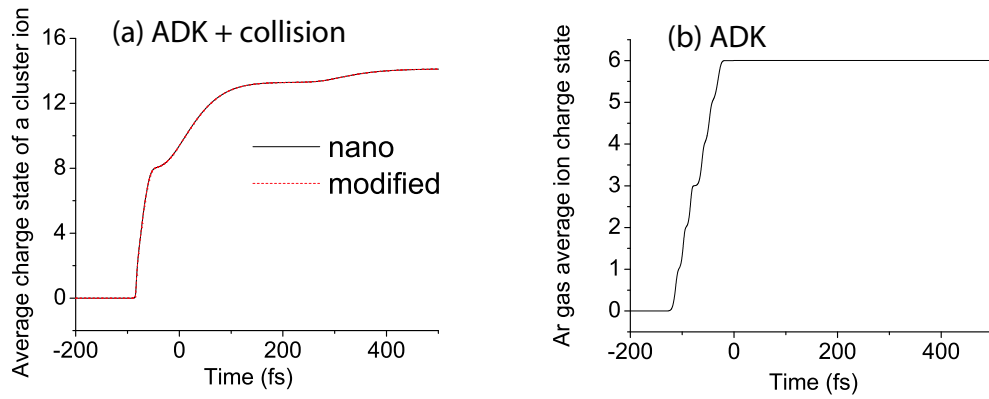


Figure 2.3: Average charge state of cluster ions. (a) Cluster case which is subject to field ionization + collisional ionization. (b) Gas Ar charge state.

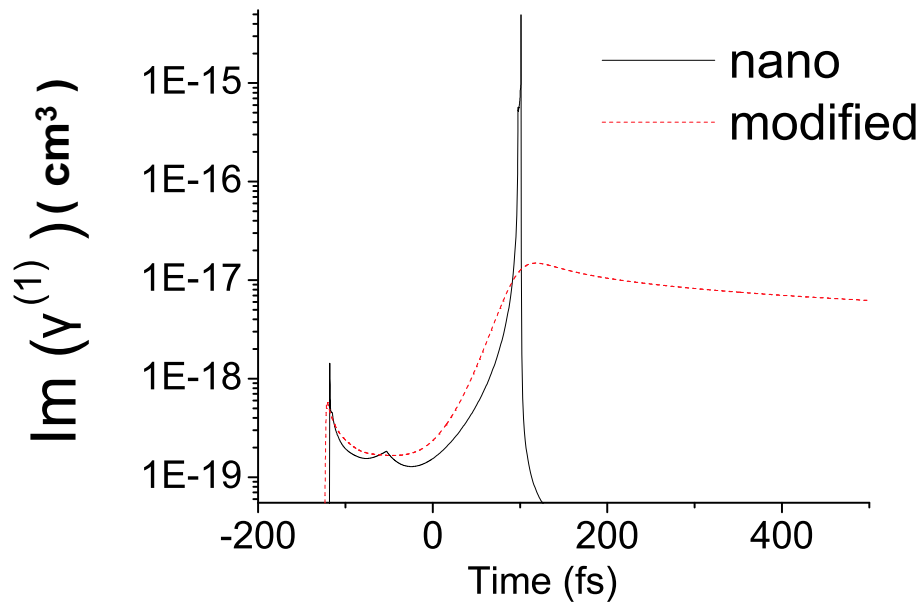


Figure 2.4: Time evolution of imaginary polarizability of the 10nm cluster.

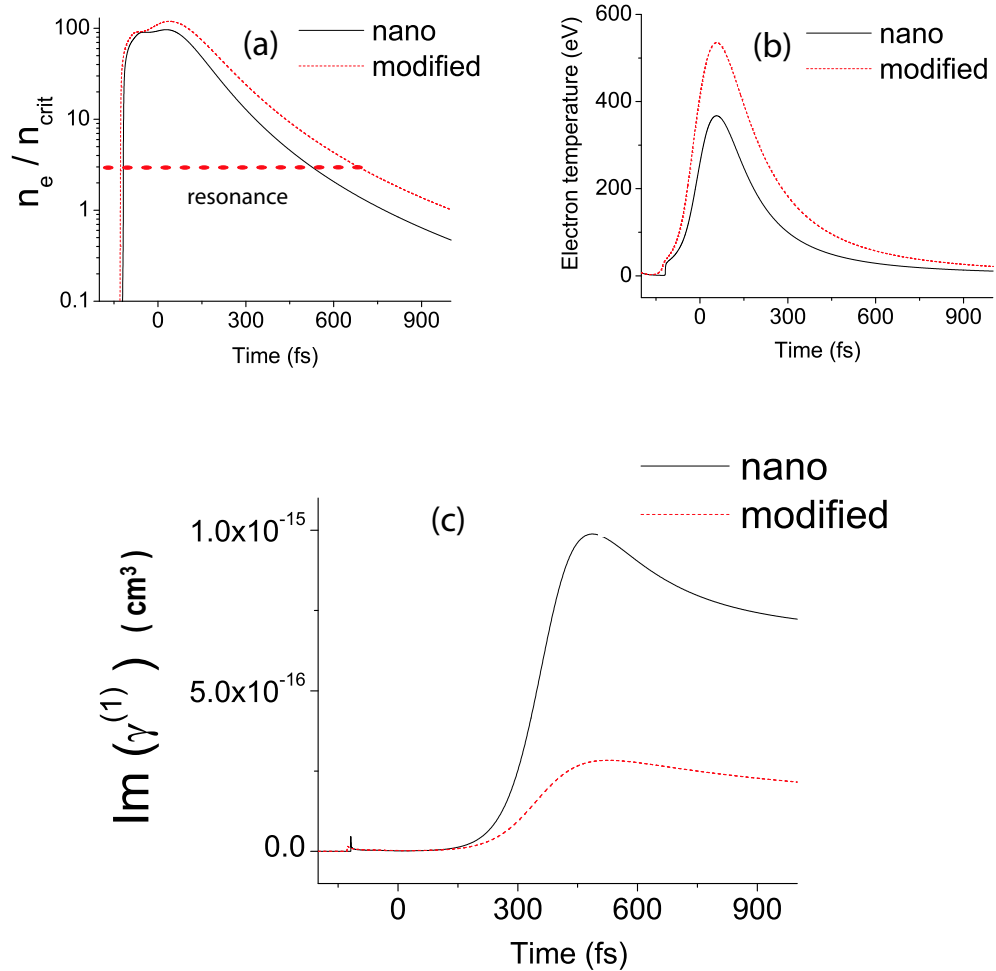


Figure 2.5: Simulation results of 30 nm Ar cluster subject to 100 fs, 800nm laser with peak intensity $1 \times 10^{16} \text{ W/cm}^2$ (a) Electron density. (b) Electron temperature. (c) cluster imaginary polarizability.

For large slowly-expanding clusters (30 nm radius), resonance is delayed until most of the heating laser pulse is past, resulting in a weak coupling between the laser and cluster. Therefore, the maximum electron temperature is smaller ($\leq 1 \text{ keV}$) than for smaller clusters. Using Eq. 2.5, Eq. 2.23 becomes

$$\gamma^{(1)} \simeq \frac{3\omega_p^2\omega\nu}{(3\omega^2 - \omega_p^2)^2 + 9(\omega\nu)^2} r_c^3, \quad (2.24)$$

which shows that the imaginary part of the cluster polarizability is proportional to $1/\nu$ near resonance ($\omega_p = \sqrt{3}\omega$). For the low electron temperature ($< 100\text{eV}$), the modified collisional frequency (Eq. 2.17) ($> 5\omega$) is larger than the upper limit for the nano-plasma model (2ω). Therefore, the cluster polarizability calculated from the nano-plasma model is overall bigger than the one calculated by the modified model (Fig. 2.5(c)).

2.4 Extension to Third Harmonic Generation

2.4.1 Theory

Fomyts'kyi *et al.* [27] recently proposed a model of third harmonic generation from a small cluster, in which a cold confined electron core oscillates nonlinearly against a nonuniform ion background in the strong laser field, generating third harmonic light (Fig. 2.6). Fomyts'kyi *et al.* treated the collective core oscillation as a nonlinear, anharmonic oscillator, in which the anharmonic potential arose from ion density nonuniformity growth produced during cluster expansion. The model predicts a strong resonant enhancement (nonlinear Mie resonance) of third harmonic generation when the frequency of the applied field equals to one third of the core eigenfrequency. Although this model over-simplifies the laser-cluster interaction, ignoring the electron density gradient and electron-ion collisions, I will follow its basic concept in my cluster jet simulation. In particular, I included the ion-electron

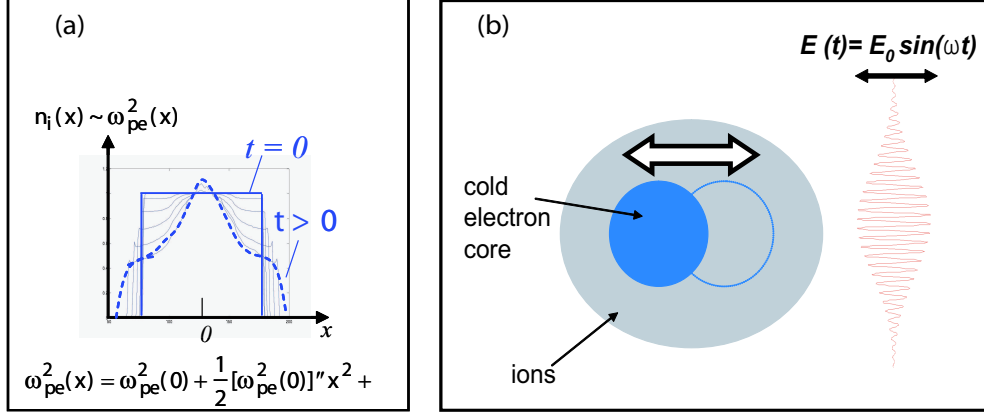


Figure 2.6: Third harmonic generation mechanism from clusters proposed by Fomyts'kyi *et al.* [27]. (a) Ion nonuniformity and anharmonic potential growth in the expanding cluster (b) Third harmonic generation from cold electron core oscillation in the cluster.

collisional frequency (ν) and adjusted a constant factor in the anharmonic strength term to fit the experimental data. I will discuss this adjustment in Chapter 4.

To calculate $\chi^{(3)}$, individual clusters were modeled as anharmonic oscillators with anharmonic strength

$$b = \varsigma \frac{\omega_p^2}{r^2}, \quad (2.25)$$

where ω_p is the plasma frequency in the cluster, r is a scale length (\leq cluster radius r_c) of ion density nonuniformity responsible for THG and ς is a geometrical constant of order unity or less [27, 38]. The electron equation of a motion is

$$\ddot{x} + \nu \dot{x} + \frac{\omega_p^2}{3} x - bx^3 = -\frac{eE_l(\omega)}{m_e}, \quad (2.26)$$

where ν is the electron-ion collisional frequency, e is the electron charge, E_l is the applied electric field with frequency ω , and m_e is the electron mass. Here, the factor $\frac{1}{3}$ in the resonance term ($\frac{\omega_p^2}{3}$) originates from the spherical geometry of the cluster.

The TH dipole moment of one cluster is then

$$p_{plasma}^{(3)} = -N_e e x^{(3)}(3\omega) = N_e \frac{e^4}{m_e^3} \zeta \frac{\omega_p^2}{r^2} \frac{E_l^3}{(\omega^2 - \frac{\omega_p^2}{3} + i\nu\omega)^3 ((3\omega)^2 - \frac{\omega_p^2}{3} + i\nu 3\omega)}, \quad (2.27)$$

where N_e is the ionized electron number in the cluster. The formula shows that the $\chi^{(3)}$ resonance is the product of the ω resonance ($\omega^2 - \frac{\omega_p^2}{3} + i\nu\omega$) and the 3ω resonance ($((3\omega)^2 - \frac{\omega_p^2}{3} + i\nu 3\omega)$).

We also included the contribution of un-ionized monomer gas, clusters and ions, which were neglected in Ref. [27]. Then, $\chi^{(3)}$ for the gas jet is

$$\begin{aligned} \chi^{(3)} &= n_c (p_{plasma}^{(3)} + \sum_{i=0} p_{atom-ion.cluster}^{(3)}) / E_l^3 + \sum_{i=0} (n_{mi} p_{gasi}^{(3)}) / E_l^3 \\ &= n_c N_e \frac{e^4}{m_e^3} \zeta \frac{\omega_p^2}{r^2} \frac{1}{(\omega^2 - \frac{\omega_p^2}{3} + i\nu\omega)^3 ((3\omega)^2 - \frac{\omega_p^2}{3} + i\nu 3\omega)} \\ &+ n_c \sum_{i=0} N_i \alpha_i^{(3)} \left(\frac{3}{\varepsilon_c + 2} \right)^3 + \sum_{i=0} (n_{mi} \alpha_i^{(3)}), \end{aligned} \quad (2.28)$$

where n_c is the cluster density in the gas jet, N_i is the number of neutral atoms or ions in the cluster, ε_c is the dielectric constant of the cluster, n_{mi} is the monomer ion density ($i = 0$ neutral atom) in the jet and $\alpha_i^{(3)}$ is the THG hyperpolarizability of Ar from Ref [39]. However, only $i = 0$ (unionized atoms) contributed significantly to $\chi^{(3)}$. The second term is the bound electron cluster contribution. The cluster dielectric constant (ε_c) is

$$\varepsilon_c = \varepsilon_{c.atomic} + \varepsilon_{c.plasma} = \frac{4\pi n_0 \alpha_0^{(1)}}{1 - \frac{4\pi n_0 \alpha_0^{(1)}}{3}} + 1 - \frac{\omega_p^2}{\omega(\omega + i\nu)}, \quad (2.29)$$

where n_0 is the neutral atomic density in the cluster, and $\alpha_0^{(1)}$ is the Ar atom polarizability. For nonrelativistic probe intensity, the contribution of the electron

plasma ionized from unclustered gas to $\chi^{(3)}$ can be neglected [40]. To evaluate THG coherence length, we calculated the refractive index of the gas jet for both 800 nm (fundamental) and 266 nm (third harmonic) using $n_{jet}(\omega) \approx 1 + 2\pi n_c \gamma^\omega + 2\pi n_m \alpha_0^{(1)} - \omega_{p.coro}^2/2\omega^2$. Here γ^ω is the cluster polarizability, $\alpha_0^{(1)}$ is the atomic polarizability of the monomers and $\omega_{p.coro}$ is the ionized coronal plasma frequency of unclustered ionized monomers. The coronal plasma is generated solely by ADK optical field ionization [33]. Empirical fits to optical absorption discussed in Chapter 4 and gas jet measurements by Dorchie *et al.* [31] demonstrate that approximately 15 % of Ar atoms condensed into clusters out of 10^{18} cm^{-3} total atomic density. Cluster/monomer ratio 0.15/0.85 was then used in the calculations. The modified nano-plasma model was used because it correctly describes the linear cluster polarizability.

2.4.2 Simulation

Fig. 2.7 shows the calculated time evolution of $|\chi^{(3)}|$ and imaginary cluster polarizability when the gas jet is interacting with 400 nm, 100 fs laser pulse with peak intensity $1 \times 10^{15} \text{ W/cm}^2$ (our pump condition). For simplicity, we put $\varsigma = 1$ and $r = r_c$. Independent of this assumption, the calculated $|\chi^{(3)}|$ reaches an earlier, sharper resonant enhancement than the imaginary linear polarizability which is related to the laser absorption. However, the “enhanced” $|\chi^{(3)}|$ is weaker than $|\chi^{(3)}(\Delta t < 0)|$ of the unexcited clusters by several orders of magnitude, suggesting that the relevant scale length r may be, in fact, much less than the cluster size based on our experiments. I will discuss this in Chapter 4 when I analyze the data.

According to the Fig. 2.7(a), smaller clusters yield stronger, sharper resonances for equivalent atomic density. This is because small clusters expand faster, so the ω resonance and the 3ω resonance (see Eq. 2.27) overlap more strongly in time, creating a double enhancement. However, smaller clusters are produced with

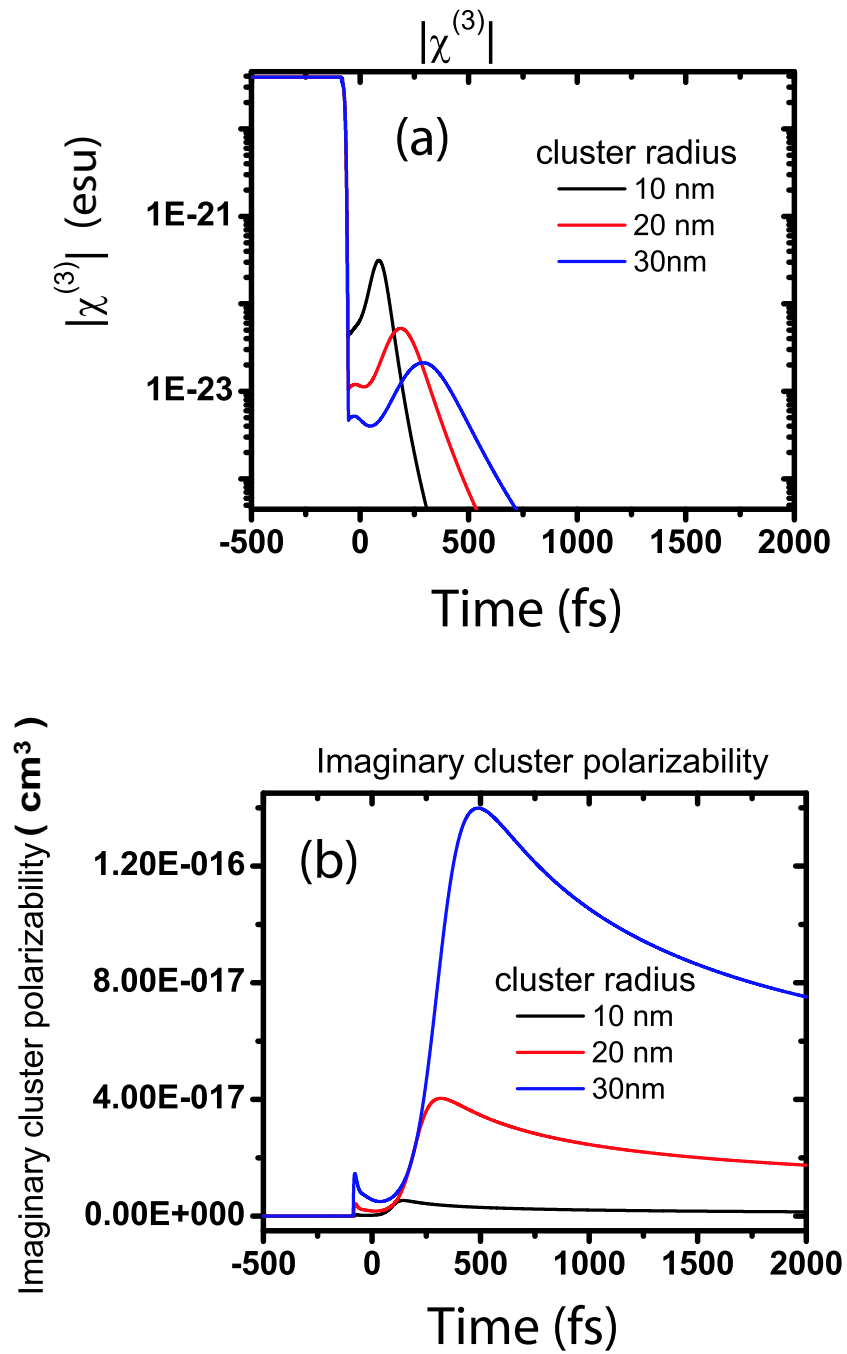


Figure 2.7: Calculated time evolution of $|\chi^{(3)}|$ and $Im(\gamma(800nm))$ of the gas jet with different clusters, irradiated by 100 fs, 400 nm laser with peak intensity 1×10^{15} W/cm^2 .

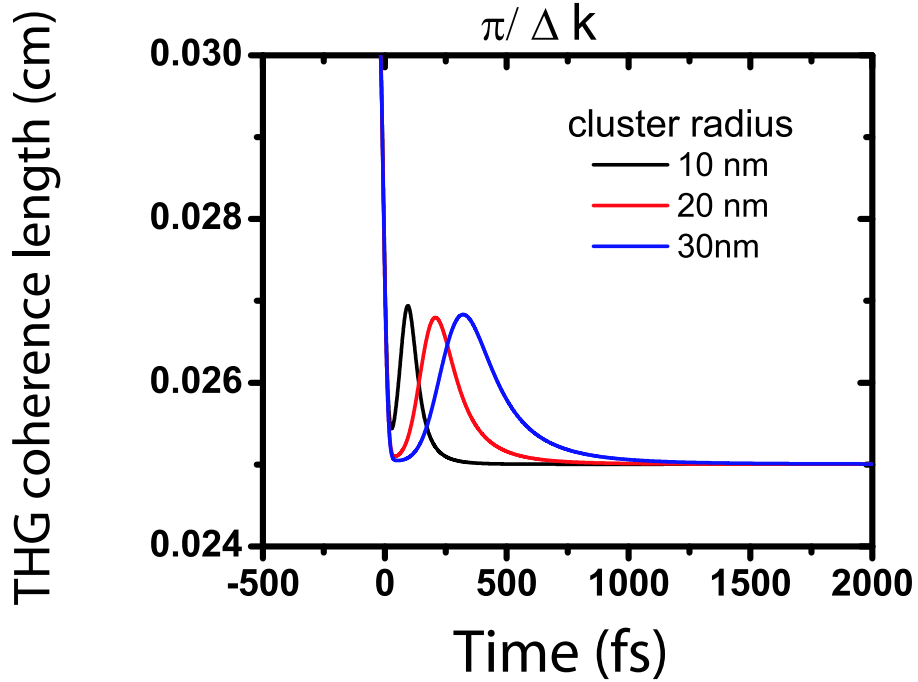


Figure 2.8: Time evolution of the THG coherence length

smaller backing pressure, which in turn produces smaller gas jet density (see Eq. 4.1) [13] and according to Ref. [31], a smaller fraction of Ar gas forming clusters. Therefore, I expect that in practice, the $|\chi^{(3)}|$ resonances of small clusters should be relatively less pronounced than indicated by the calculation. The calculated time scale shown in Fig. 2.7(a) is correct, but the absolute magnitude of the third order susceptibility of the gas jet will have to be re-scaled significantly when analyzing data. Fig. 2.7(b) shows that bigger clusters reach absorption resonances later than smaller clusters and the overall optical absorption is larger for bigger clusters.

Fig. 2.8 shows the THG coherence length which is defined by $l_c = \pi/\Delta k = c\pi/3\omega|n_{jet}(3\omega) - n_{jet}(\omega)|$. As ionization takes place, the coherence length decreases quickly, suggesting that the unionized medium is more phase-matched than the ionized gas jet plasma. However, surprisingly, the coherence length increases again

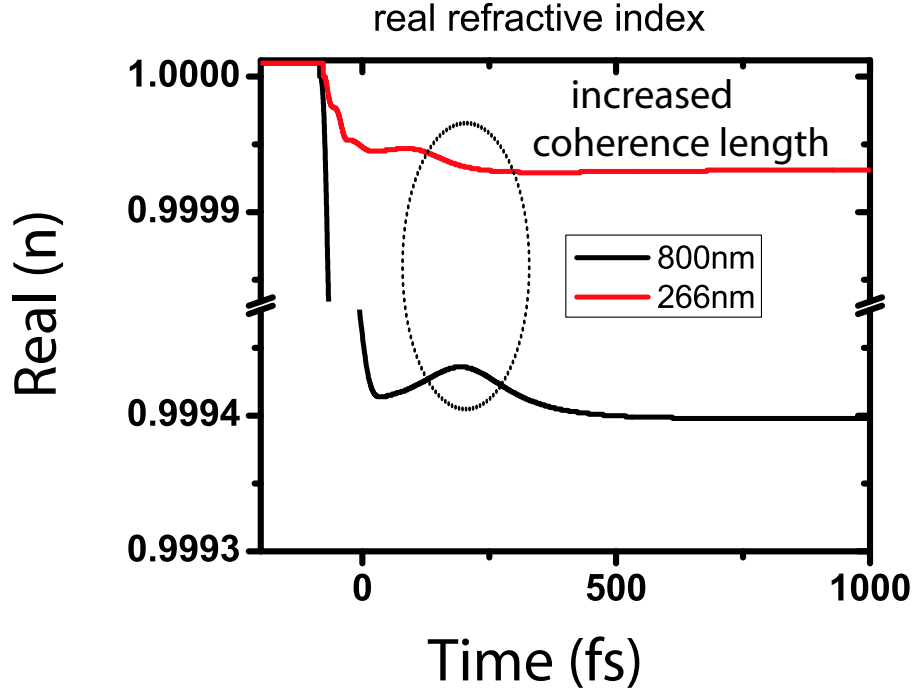


Figure 2.9: Real refractive index of 800nm and 266nm for the 20nm clustered jet.

and the local peak of l_c occurs almost simultaneously with the $\chi^{(3)}$ resonance. This temporally local, phase matching enhancement is related to the separate temporal evolution of $n_{jet}(3\omega)$ and $n_{jet}(\omega)$, shown in Fig. 2.9. A local increase in $n_{jet}(\omega)$ at $\Delta t \sim 200$ fs coincides with a local decrease in $n_{jet}(3\omega)$, thereby decreasing $|n_{jet}(3\omega) - n_{jet}(\omega)|$ and increasing l_c . Further increase of the coherence length should be possible by increasing the cluster fraction using cryo-cooling techniques [41, 42] or Xe (better clustering) gas [13].

Chapter 3

Terawatt laser system

Ultrafast, high-power laser technology has progressed remarkably over the last 20 years using the Chirped-Pulse Amplification (CPA) technique [43, 44, 45, 46]. In CPA, a weak ($\sim 10^{-9}$ J), short ($\sim 10^{-14}$ s) laser pulse is first generated from a modelocked oscillator, then chirped to several hundreds ps or even ns by a stretcher composed of optical gratings or fibers. The low-power stretched pulse is then safely amplified by factors of 10^6 - 10^9 in several stages. Finally, the amplified pulse is compressed back to ultrashort duration using a second set of gratings [47].

Our 1 TW (10^{12} W) system has been upgraded to 3 TW. In this chapter, I will mainly discuss a multi-pass amplifier which we built as part of this upgrade. Other stages (oscillator, stretcher, regenerative amplifier, compressor), described in Ref. [48], remain nearly unchanged except for minor modifications.

3.1 Oscillator, Stretcher, and Regenerative amplifier

Fig. 3.1 shows the our home-built Kerr Lens Modelocked (KLM) [49] Ti:Sapphire oscillator. A 532 nm CW laser (Millenia V from Spectra Physics) pumps a 10 mm long Brewster-cut Ti:Sapphire crystal. Two prisms compensate for the positive

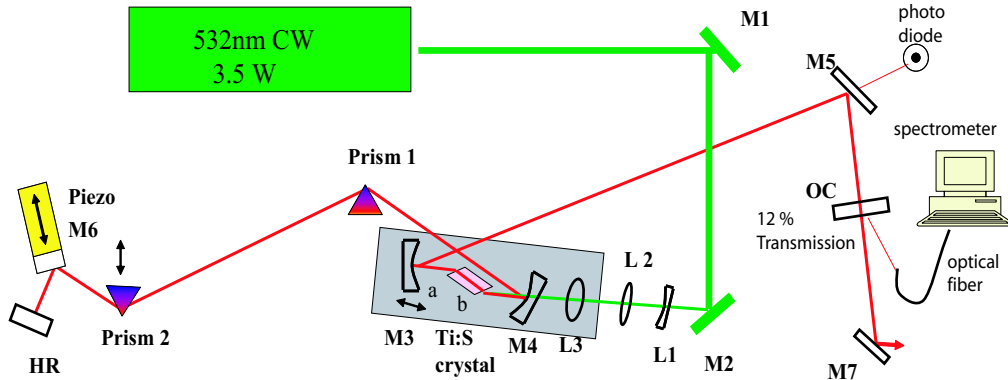


Figure 3.1: Kerr-lens modelocked Ti:Sapphire oscillator.

dispersion of the crystal [50, 51] and an output coupler (OC) transmits about 12% of the energy. A photodiode and a fiber-optic spectrometer diagnose the modelocking status and the spectrum, which is adjustable (from 10 nm to 60 nm bandwidth). During the laser upgrade, we renovated the oscillator by simulating its operation theoretically (see Appendix A) and modifying intracavity configuration for more stable modelocking experimentally. The pulse repetition rate is about 76 MHz and the energy of each pulse is about 9 nJ. We normally operate with a 30 nm bandwidth (30 fs transform-limited pulse).

The oscillator pulse is, then, expanded to 400-500 ps in the grating stretcher first designed by Lemoff and Barty [52]. A pair of antiparallel gratings (1200 lines/mm) and a telescope of two gold cylindrical mirrors (1 m curvature) give a positive dispersion (Fig. 3.2). The incidence angle is 61.9° and the beam after the first round trip is reflected back by an image inverter. The image inverter not only doubles the pulse expansion but also reduces spatial chirp and spectral divergence.

A regenerative amplifier (see Fig. 3.3) reduces repetition rate to 10 Hz by selecting an individual pulse from the 76 MHz pulse train. The gain is about 10^6 , therefore the energy increase to ≥ 1 mJ after about 30 round trips in the regen cavity.

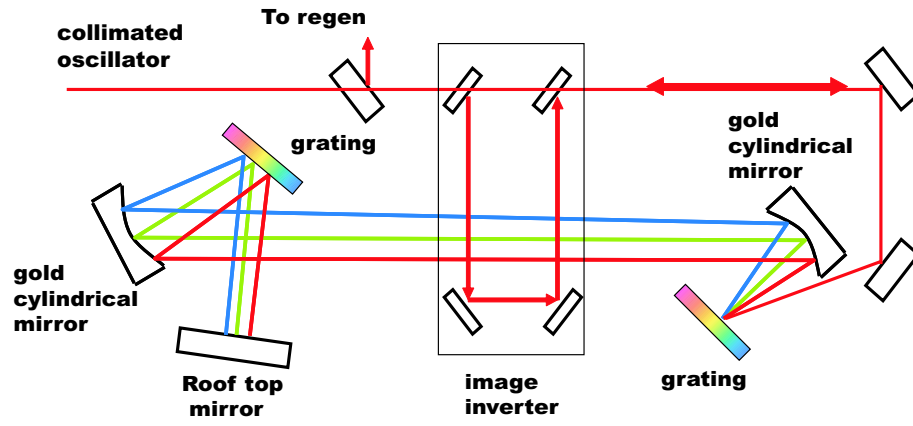


Figure 3.2: Pulse stretcher.

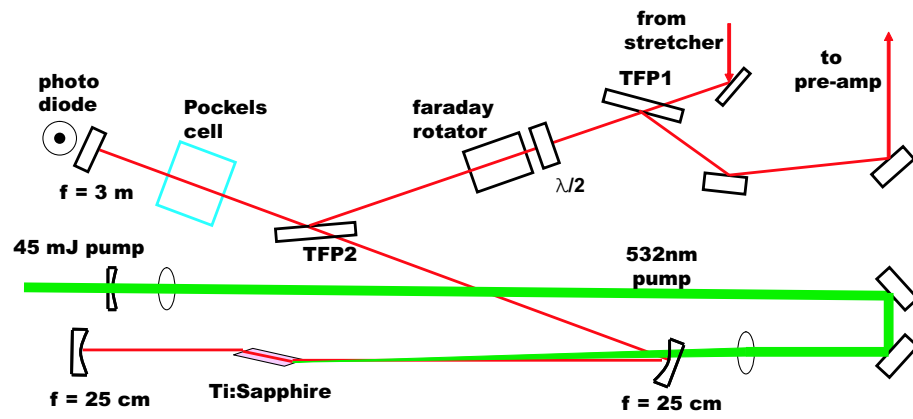


Figure 3.3: Regenerative amplifier.

This high gain regenerative amplifier has the advantage of filtering out higher-order transverse modes caused by aberration in the stretcher because the regen cavity selects a lowest order mode and stabilizes it by operating near gain saturation. A p-polarized (parallel to an optical table) seed pulse passes through a broadband Thin Film Polarizer (TFP1), a $\lambda/2$ waveplate and a Faraday rotator, and is rotated to s-polarization. Then, the beam reflects from TFP2 and double passes through a Pockels cell operated as a $\lambda/4$ plate, thereby rotating its polarization by 90° back to p-polarization so that it transmits through TFP2. During its first gain pass through a Ti:Sapphire crystal, the Pockels cell is switched to a $\lambda/2$ waveplate and the pulse is trapped in the cavity without polarization change. After about 30 round trips, the Pockels cell is returned to a $\lambda/4$ plate, so the trapped pulse again becomes s-polarized, reflects from TFP2, and exits the cavity. Because the combination of $\lambda/2$ waveplate and Faraday rotator does not change the polarization for the output path [53], TFP1 also reflects the s-polarized output and the beam proceeds to a pre-amplifier stage.

3.2 Pre-amplifier and Power-amplifier

Fig. 3.4 shows a 6 pass pre-amplifier and a 4 pass power-amplifier. A 600 mJ, 532nm Q-switched laser (~ 100 mJ Surelite from Continuum and ~ 500 mJ GCR4 from Spectra Physics) pumps a 1 cm long pre-amplifier crystal. The output energy after 6 pass is about 200 mJ, which was used after compression for the laser-cluster interaction experiment. After passing through a spatial filter, the beam can be further amplified, generating about 600-700 mJ, in a 4 pass power-amplifier. A 1 cm long crystal is pumped by a PRO350 Nd:YAG laser from Spectra Physics (pump energy ~ 1.1 J). To design the pre-amplifier and power-amplifier, we used simple models [54, 55, 56, 57] to analyze: (1) how much energy we can extract for a given pump energy, (2) how much a thermal lensing occurs during beam propagation

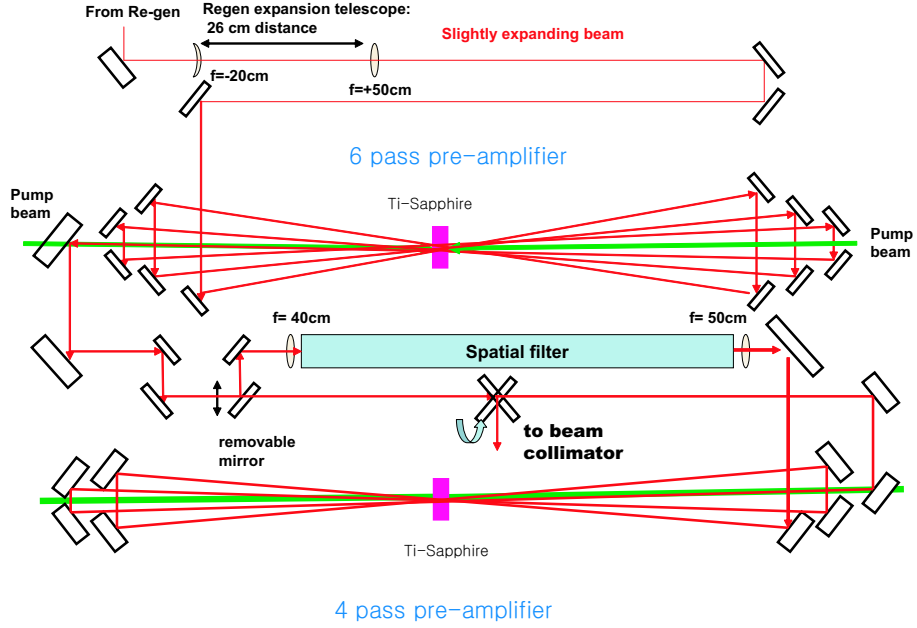


Figure 3.4: Pre-amplifier and power-amplifier

through temperature gradients in the pumped crystal.

For calculations of gain, I used measured pump parameters as follows: Fit the imaged pump beams with a super-Gaussian intensity function

$$I(r) = I_0 \exp[-(r/b)^c] , \quad (3.1)$$

where I_0 is the peak intensity, b is the $1/e$ radius, and c is the super-Gaussian order, showed that they have about 2.8 mm radius with the super-Gaussian order 4. It corresponds to about 3 J/cm² fluence and approximately 88 % of the pump beam was absorbed by the pre-amplifier crystal. For a 1-D gain model (*i.e.* neglecting focusing), we first calculated the number of atoms excited by pump absorption as a function of pump radius. Then, after considering both fluorescence loss from the crystal and the measured loss per pass ($\sim 3\%$) from the optics, the extracted energy was calculated using a Franz-Nodvik model [54, 55]. I assumed that the seed

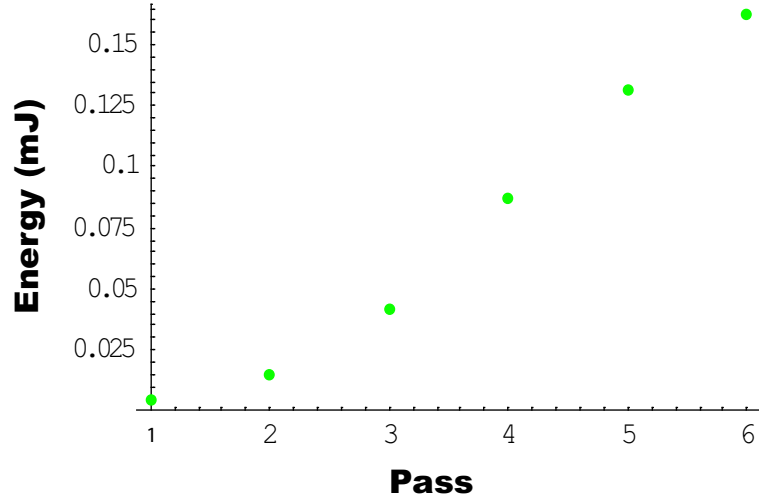


Figure 3.5: Calculated pre-amp energy for each pass

Gaussian beam (super-Gaussian order 2) had 1.2 mJ energy with 2.35 mm radius and was collimated during its propagation. Fig. 3.5 shows the calculated energy per pass from the pre-amplifier. For the power-amplifier, the seed Gaussian beam (5 mm radius) energy was put at 150 mJ because of loss in the spatial filter. The pump beam radius was 5 mm with super-Gaussian order 7, which corresponds to 1.55 J/cm² fluence. The loss per each pass was 5 %. The calculated energy (~ 160 (570) mJ for the pre(power)-amplifier) somewhat underestimates the measured energy (~ 180 -200 (600-700) mJ). We think that the discrepancy results from beam size changes caused by thermal lensing.

To remove heat from a Ti:Sapphire rod which is pumped by an intense Q-switched laser, cooling water flows along the cylindrical rod surface. As a result, a radial temperature gradient forms in the crystal. The steady-state radial temperature equation is [56]

$$\frac{d^2T}{dr^2} + \frac{1}{r} \frac{dT}{dr} + \frac{Q}{K} = 0, \quad (3.2)$$

where Q is the heat generated per unit volume, and K is the thermal conductivity

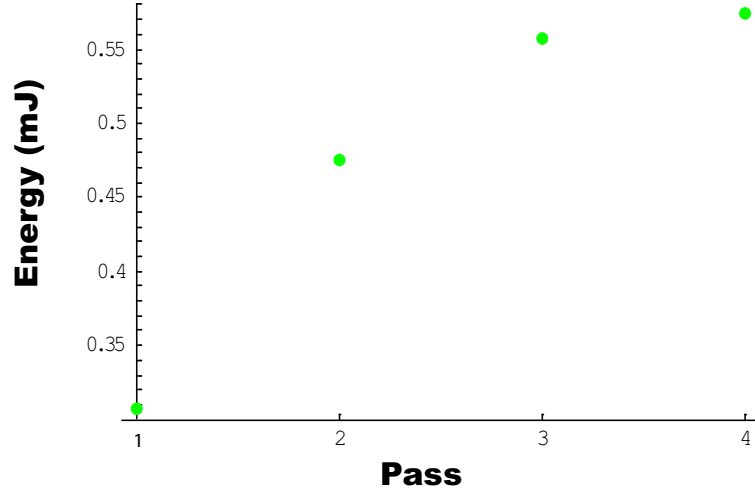


Figure 3.6: Calculated power-amp energy for each pass

(35 W/m⁰C for Ti:Sapphire). Assuming Q is uniform, the solution is

$$T(r) = T(r_0) + \frac{Q}{4K}(r_0^2 - r^2), \quad (3.3)$$

where $T(r_0)$ is the surface temperature of the rod. Because of the temperature gradient, the refractive index also varies radially as

$$n(r) = n(0) + (T(r) - T(0)) \left(\frac{dn}{dT} \right) = n(0) - \frac{Q}{4K} \frac{dn}{dT} r^2, \quad (3.4)$$

where $n(0)$ is the refractive index at the rod center, and $\frac{dn}{dT}$ is the thermal refractive coefficient ($13 \times 10^{-6} K^{-1}$ for Ti:Sapphire). A quadratic variation in index makes the medium function as a spherical lens [58]. More specifically, for the case of a nonuniform heating using the Q-switched laser pumping, the focal length of the thermal lens can be expressed by [56]

$$f_{th} = \frac{\pi K w_p^2}{P_H (dn/dT)} \left(\frac{1}{1 - \exp(\alpha l)} \right), \quad (3.5)$$

where w_p is the $1/e^2$ radius of the Gaussian pump beam, P_H is the fraction of the pump power involved in heating, and α is the absorption coefficient of the crystal. For the pre-amplifier, the pump beam (532 nm) has about $3\text{J}/\text{cm}^2$ fluence, 10 Hz repetition rate, and 3 mm radius. Therefore, P_H is

$$P_H \simeq (3\text{ J}/\text{cm}^2)(10\text{ s}^{-1})(\pi(3\text{ mm})^2)(1 - 532\text{ nm}/800\text{ nm}) \simeq 2.84\text{ Watts}, \quad (3.6)$$

and the focal length is about 30 m, which can affect the 6 pass pre-amplifier.

To counterbalance the thermal lensing, two lens ($f = -20\text{cm}$, $f = 50\text{cm}$) (see Fig. 3.4) were placed to diverge the regen output beam slowly as it enters the pre-amplifier. First, by measuring the regen beam propagation and adjusting the separation of two lenses (32.8 cm), the beam was collimated (Fig. 3.7 (a)). Then, we made the beam slowly diverging by moving the focusing lens ($f = 50\text{cm}$) closer to the first lens ($f = -20\text{cm}$) to reduce the thermal lensing effect ($f = 35\text{m}$) (Fig. 3.7 (b) and (c)). This method worked well enough that we were able to produce a pre-amplified beam of high energy ($\sim 200\text{ mJ}$) and good collimation (slowly converging beam). For the power-amplifier, we did not use the counterbalancing lens set because the focal length of the thermal lens is more than 80 m due to the lower pump fluence ($\sim 1\text{ J}/\text{cm}^2$) and it is only a 4 pass amplifier.

3.3 Compressor

The pre-amplifier beam was expanded to reduce the peak intensity and collimated, using a diverging lens ($f = -20\text{ cm}$) and a converging lens ($f = +75\text{ cm}$) set ($\times 3.75$ expansion) without a spatial filter. The diameter of the expanded beam is about 1.5 inches (πw_0 , 99 % of total energy) with a near Gaussian profile (Fig. 3.8). The pulse is re-compressed in a compressor (Fig. 3.9) in which two parallel gold-coated gratings (1200 lines/mm) are used with an incidence angle 69° . By adjusting

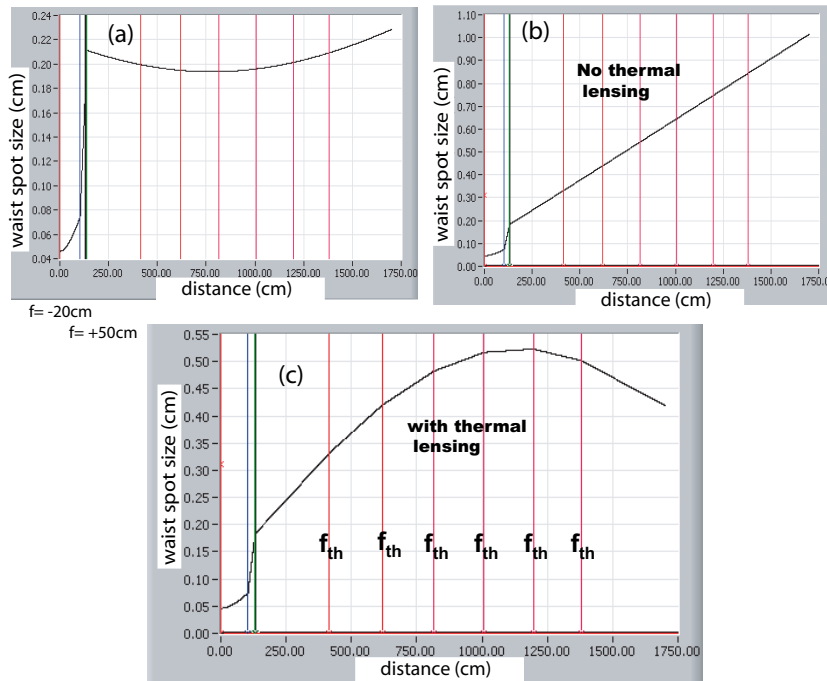


Figure 3.7: Thermal lens compensation calculation in the pre-amplifier. The red lines represent the crystal position. (a) collimated regenerative amplifier output. A diverging lens ($f = -20\text{cm}$) is located at 104.5 cm and a focusing lens ($f = 50\text{cm}$) at 137.3 cm. (b) slowly diverging beam to compensate for the thermal lensing. The focusing lens was moved closer to the diverging lens by 6.8 cm. (c) beam propagation with 35 m focal length thermal lenses in the 6 pass pre-amplifier.

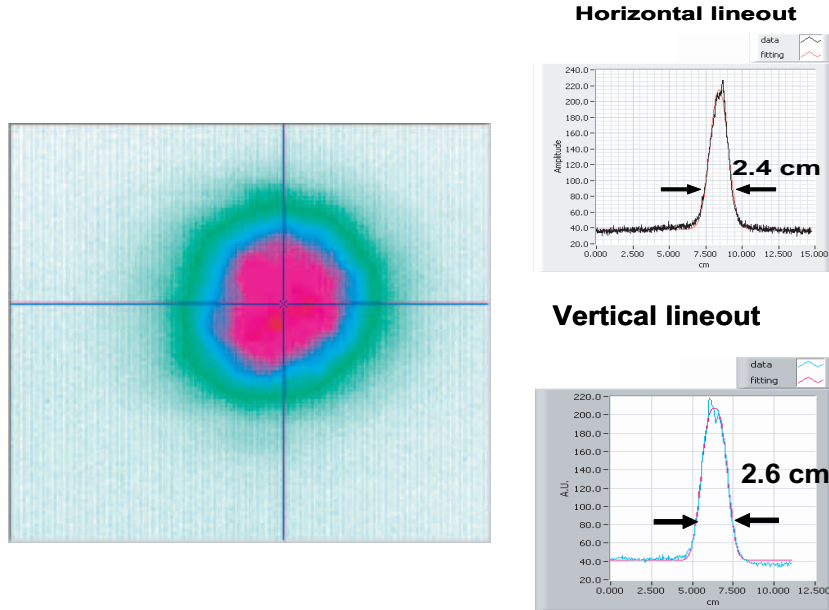


Figure 3.8: Expanded and collimated pre-amplifier mode. $1/e^2$ diameters are shown in the horizontal and vertical lineout.

separation of two gratings, we can minimize the pulse temporal width. A single-shot autocorrelation measurement shows that ~ 80 fs (FWHM) minimum pulse length can be achieved routinely (Fig. 3.10). The throughput of the compressor is about 40 %, yielding final energy ~ 80 mJ.

For expansion and collimation of the power-amplifier, a telescope of $f=+1.5\text{m}$, $f=+4\text{m}$ lens set ($\times 2.7$ expansion) combined with a spatial filter was used to reduce the diffraction pattern caused by a small power-amplifier crystal. The expanded beam diameter is about 1.3 inches (πw_0) with a flattop profile (see Fig. 3.11) and the energy is about 300 mJ. The minimum pulse width was measured as ~ 120 fs with the same incidence angle (69°) (Fig. 3.12).

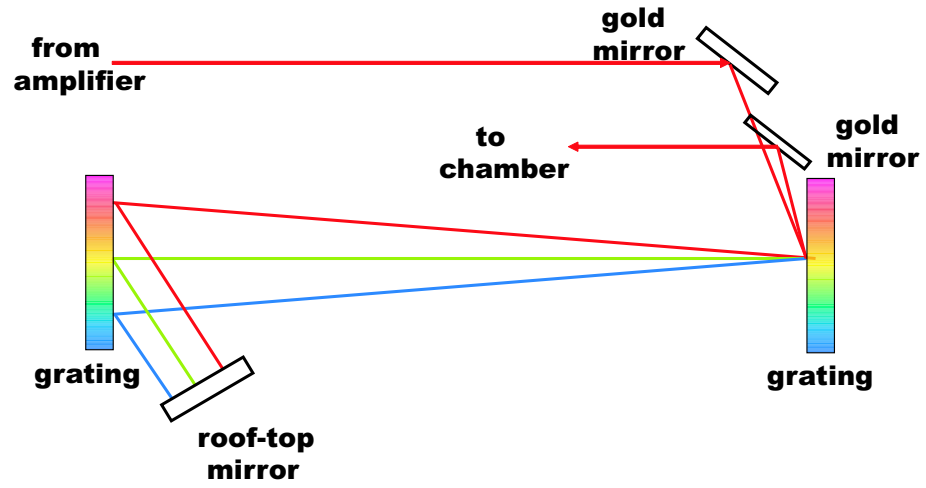


Figure 3.9: Compressor.

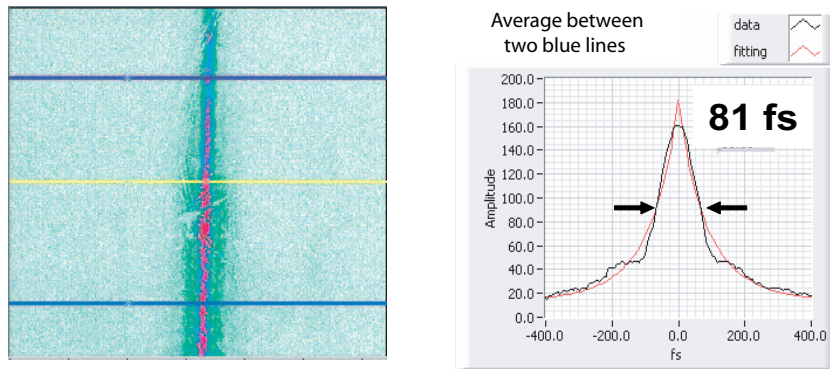


Figure 3.10: Single-shot autocorrelation trace for the pre-amplifier.

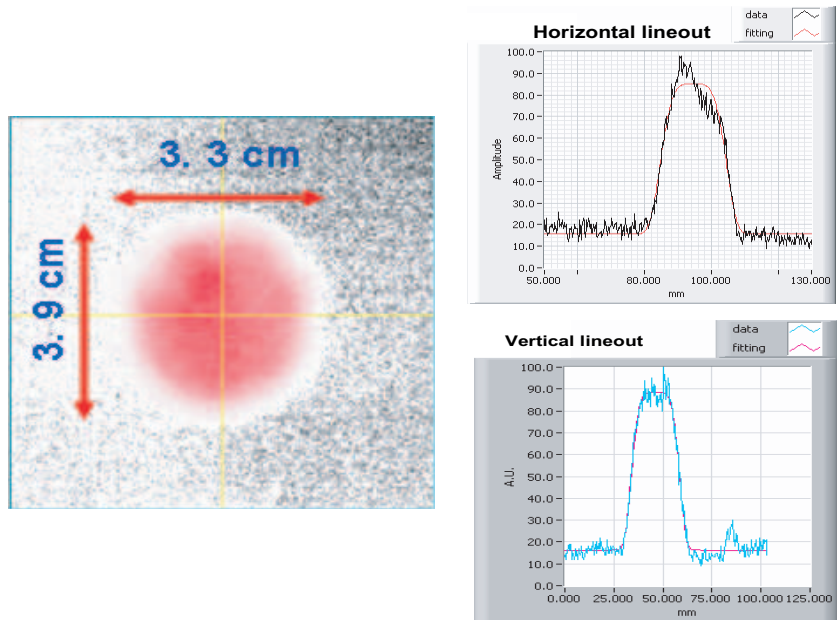


Figure 3.11: Expanded and collimated power-amplifier mode.

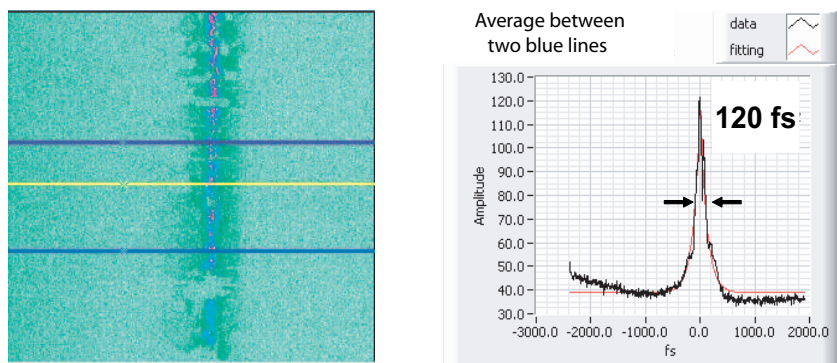


Figure 3.12: Single-shot autocorrelation trace for the power-amplifier.

Chapter 4

Time-resolved experiment in a clustered jet

4.1 Characterization of a supersonic gas jet

We used Mach-Zehnder interferometry and 90° Rayleigh scattering to characterize the atomic density and cluster size, respectively, of our supersonic gas jet. The second harmonic (532 nm) of a Q-switched Nd:YAG laser (PRO-350 from Spectra Physics), about 10 ns long, was used for these measurements. We maintained nozzle opening time at 1.5 ms for maximum scattered signal and low chamber pressure. Further increase of the opening time till 4 ms did not increase the scattered signal. We adjusted the delay of nozzle opening time with respect to the pulsed laser to obtain the optimal signal.

4.1.1 Empirical parametrization of cluster size

Clusters were formed by a Series-9 pulsed solenoid valve from Parker Hannifin (General Valve division) and a supersonic conical nozzle with 750 μm orifice and 11° half expansion angle backed by high pressure Ar gas. An empirical parameter for cluster

formation is the Hagen parameter [13, 41]

$$\Gamma^* = k \frac{(0.74d/\tan\alpha)^{0.85}}{T_0^{2.29}} P_0, \quad (4.1)$$

where k is a parameter depending on gas species ($k=1650$ for argon), d is the nozzle orifice diameter, α is half expansion angle, T_0 is gas temperature in Kelvin, and P_0 is the backing pressure in mbar. For our experimental condition ($P_0 \geq (200 \text{ psi} = 13.6 \text{ bar})$ and $\Gamma^* > 4000$), Hagen predicts that the number of monomers per cluster ($N_{\#}$) scales as

$$N_{\#} = 33 \left(\frac{\Gamma^*}{1000} \right)^{2.35}, \quad (4.2)$$

and it was assumed that almost 100 % of the atoms condensed into clusters [59, 60, 14]. However, the Hagen's formula was proposed based on measurements in continuous (CW) jet operation. Keto *et al.* [61] showed that the cluster size can be smaller than Hagen's prediction in pulsed jet operation with short nozzle opening time ($< 1\text{ms}$) and if the nozzle diameter is larger than maximum displacement of the nozzle plunger ($\sim 400 \mu\text{m}$). The lower condensation rate was also measured using Xe by Keto *et al.* [61].

Recent experiments, using a more complete gas jet characterization [31, 24], show that a larger portion ($\sim 80 \%$) of the Ar gas jet is left unclustered. Based on those measurements and analysis, Dorchie *et al.* [31] proposed a new scaling formula for Ar clusters under conditions similar to our jet:

$$N_{\#} = 100 \left(\frac{\Gamma^*}{1000} \right)^{1.8}. \quad (4.3)$$

This formula predicts a smaller number of atoms in the cluster than Hagen's prediction. As a result, the cluster radius r_c is smaller because $N_{\#} = \frac{4}{3}\pi r_c^3 n_{Ar,s}$, where $n_{Ar,s}$ is the solid Ar density ($\sim 2 \times 10^{22} \text{ cm}^{-3}$). Table 4.1 compares Ar cluster radii predicted by Eq. 4.2 and Eq. 4.3 at the given backing pressure and

room temperature.

Table 4.1: Ar cluster radius vs backing pressure at $T_0 = 293$ K.

Backing pressure (psi)	Radius by Hagena (nm)	Radius by Dorchie's (nm)
200	14	10
400	24	16
600	34	20
800	42	24

According to the analysis by Dorchie's *et al.*, more atoms condense into clusters with higher backing pressure (Table 4.2). However there is no general empirical relation between the Hagena parameter (Eq. 4.1) and the condensation rate (η).

Table 4.2: Ar cluster parameters with the backing pressure P_0 from 20 to 60 bars using a conical nozzle (620 μm orifice and $\sim 5^\circ$ half expansion angle)(Ref.[31]). η is the condensation rate, R is the average cluster radius, $\delta R/R$ is the relative width of radius statistical distribution and $N_\#$ is the number of atoms per cluster.

Backing pressure (bar)	η	R (nm)	$\delta R/R$ (%)	$N_\#$
20 (300psi)	0.207	18.3	14	6.14×10^5
40 (600psi)	0.235	27.5	12	1.97×10^6
60 (900psi)	0.253	34.8	11	3.87×10^6

4.1.2 Rayleigh scattering measurement

The Rayleigh scattering signal scales as the product of the density of clusters (N_c) and the scattering cross section of a cluster. The Rayleigh scattering cross section for a dipole sphere is [15]

$$\sigma = \frac{8\pi}{3} \frac{r_c^6}{\lambda^4} \left(\frac{\varepsilon_c - 1}{\varepsilon_c + 2} \right)^2, \quad (4.4)$$

where λ is the probing laser wavelength, and ε_c is the cluster dielectric constant. Therefore, the scattered signal scales as $\sim N_c r_c^6 \sim N_c N_\#^2$. Using the relation $N_c =$

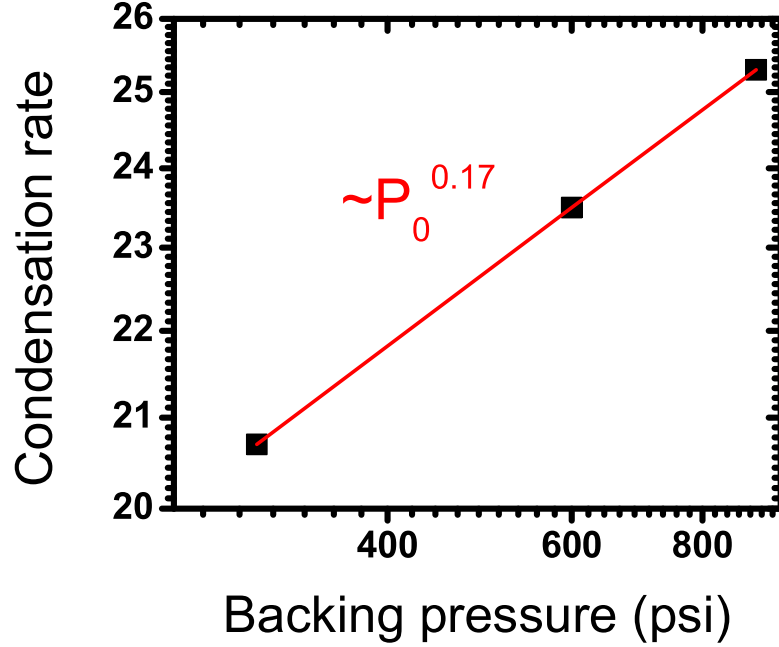


Figure 4.1: Backing pressure vs the condensation rate from Table 4.2 [31].

$N_0/N_{\#} = \eta N_{total}/N_{\#}$, where N_0 is the average density of atoms contained in clusters (excluding unclustered monomers), η is the condensation rate, and N_{total} is the total atomic (clustered atoms+monomers) density. If $\eta \sim 1$ [59, 60, 14], the signal should scale as $\sim N_0 N_{\#} \sim \eta P_0 N_{\#} \sim P_0^{3.35}$ for Hagena's prediction assuming constant temperature for different backing pressures. Fig. 4.1 shows that the condensation rate (η) from Table 4.2 scales as $P_0^{0.17}$, therefore the scattering signal for Dorchie's prediction should scale as $\sim \eta P_0 N_{\#} \sim P_0^{2.97}$, which is weaker than the scaling ($P_0^{3.35}$) predicted by Hagena.

The 532 nm beam with $\sim 200 \mu\text{J}$ energy was focused by a 1 m focal length lens after passing through a 5 mm aperture. The 90° scattering signal was collected by a f/2 lens and imaged onto a CCD camera (Figure 4.2). We took the data by

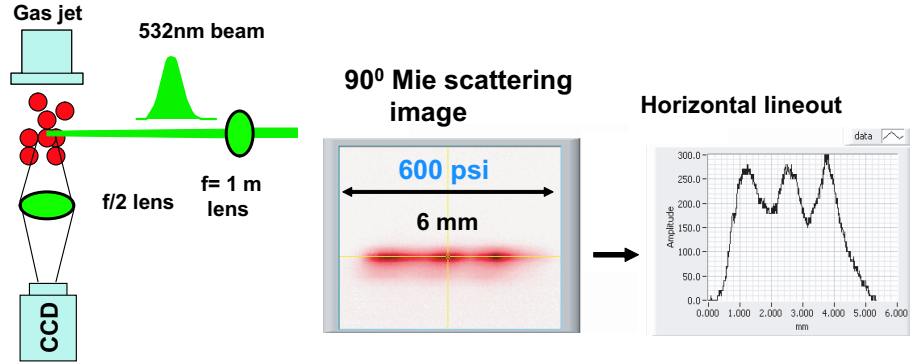


Figure 4.2: 90° Rayleigh scattering set-up and scattering CCD image.

integrating the scattered image spatially. Figure 4.3 shows that the scattered signal scales as $P_0^{2.77}$, which suggests that the Dorchie's prediction is more appropriate for our jet conditions.

4.1.3 Gas jet atomic density measurement

Figure 4.4 shows the Mach-Zehnder interferometry set-up. After dividing the input beam using a 50/50 beamsplitter (BS), a transmitted beam passed through the jet plume and a reflected beam passed through vacuum. Then, two beams were combined by another BS. We imaged the exit of the jet using a 16 cm focal length Achromat lens and a microscope objective ($\times 10$) onto a CCD camera. Fringe shifts were measured by comparing when the jet was turned on and when it was turned off (Figure 4.5).

The standard Abel inversion [63, 64, 65] was used to extract the refractive index of the gas jet from the measured phase shift. To minimize error caused by defects of imaging optics in the Abel inversion process, I used super-Gaussian fitting for the measured phase. This smooth, fitted data (red curve in Fig. 4.6) was used for calculating the refractive index of the jet.

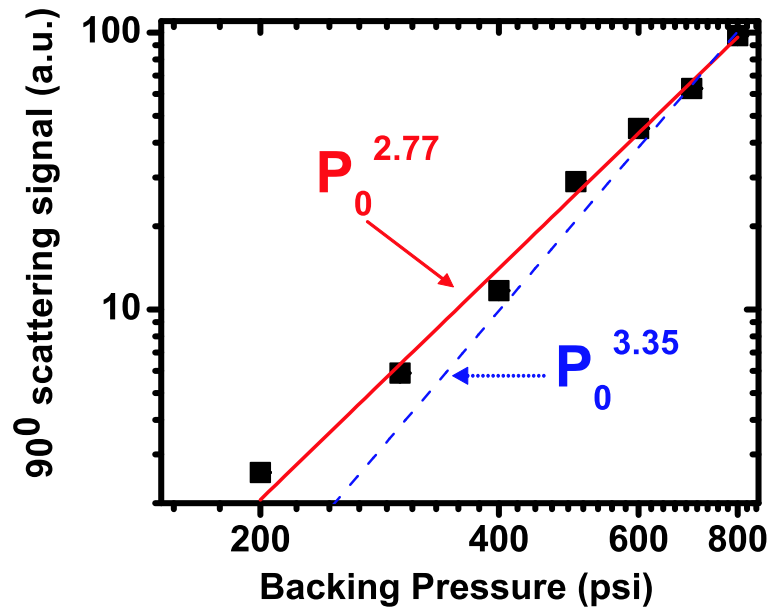


Figure 4.3: Backing pressure vs 90° scattering signal. Fit (Red solid curve) scales as $P_0^{2.77}$ and blue dotted curve is the Hagen's prediction

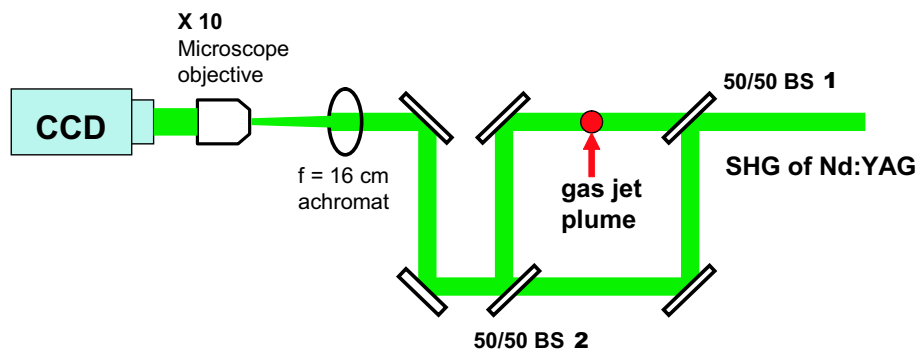


Figure 4.4: Mach-Zehnder interferometry set-up.

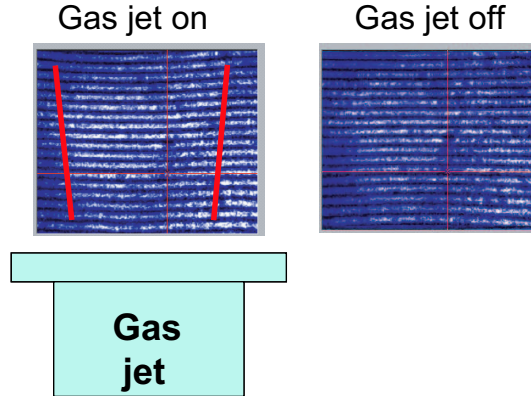


Figure 4.5: Fringe shift at 600 psi backing pressure using Mach-Zehnder interferometry .

According to Fig. 4.7, the phase shift in the interferometry is given by [63]

$$\Delta\phi(x) = 2 \left(\frac{2\pi}{\lambda} \right) \int_0^{y_0} (n(r) - 1) dy, \quad (4.5)$$

where λ is the wavelength of the probe laser, and $n(r)$ is the refractive index of the gas jet. After using the cylindrical coordinates and Abel's inversion, the refractive index can be written as

$$\Delta\phi(x) = 2 \left(\frac{2\pi}{\lambda} \right) \int_0^{r_0} \frac{(n(r) - 1)r}{\sqrt{r^2 - x^2}} dr, \quad (4.6)$$

$$2 \left(\frac{2\pi}{\lambda} \right) (n(r) - 1) = -\frac{1}{\pi} \int_r^{r_0} \frac{\phi(x)}{\sqrt{r^2 - x^2}} dx. \quad (4.7)$$

Dividing axes into small equidistant values such that $x_i = ir_0/n$ and $r_j = jr_0/n$ for $i, j = 0, 1, \dots, n - 1$, the refractive index (n_j) can be expressed by

$$n_j \equiv n(r = jr_0/n) = 1 + \frac{\lambda}{2\pi r_0} \sum_{i=0}^{i=n-1} a_{ji} \phi_i, \quad (4.8)$$

where a_{ji} is the coefficient from Ref. [65].

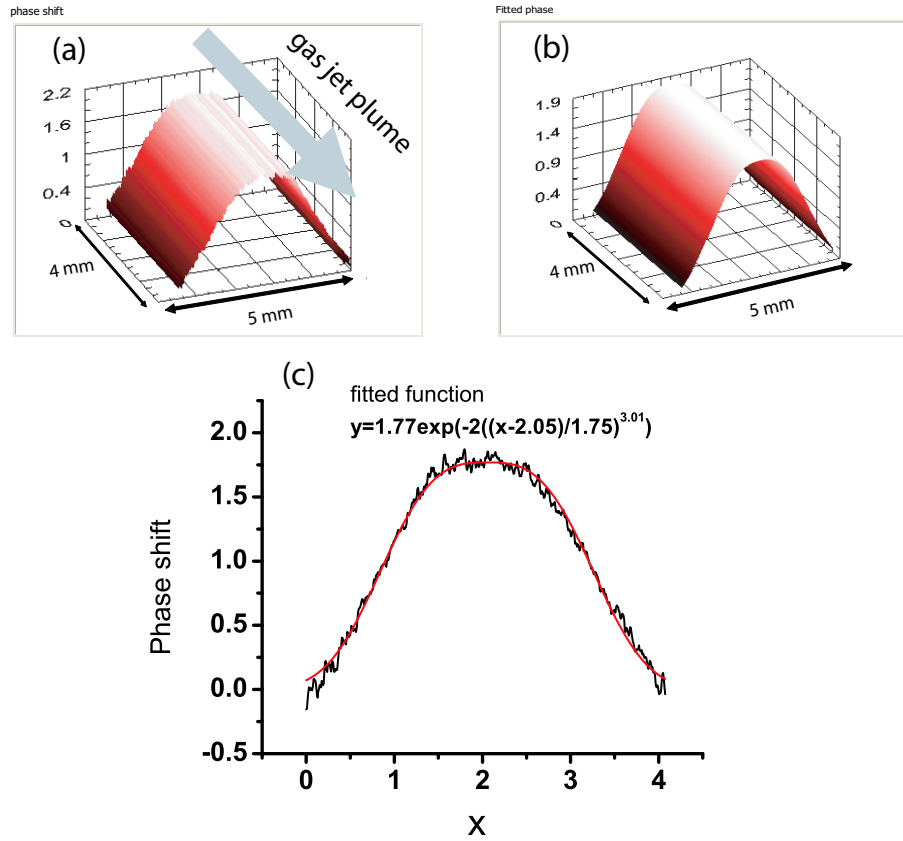


Figure 4.6: (a) Raw phase shift before fitting for 600 psi Ar. (b) Super-Gaussian fitted phase shift for 600 psi Ar. (c) Example super-Gaussian fit for the phase shift.

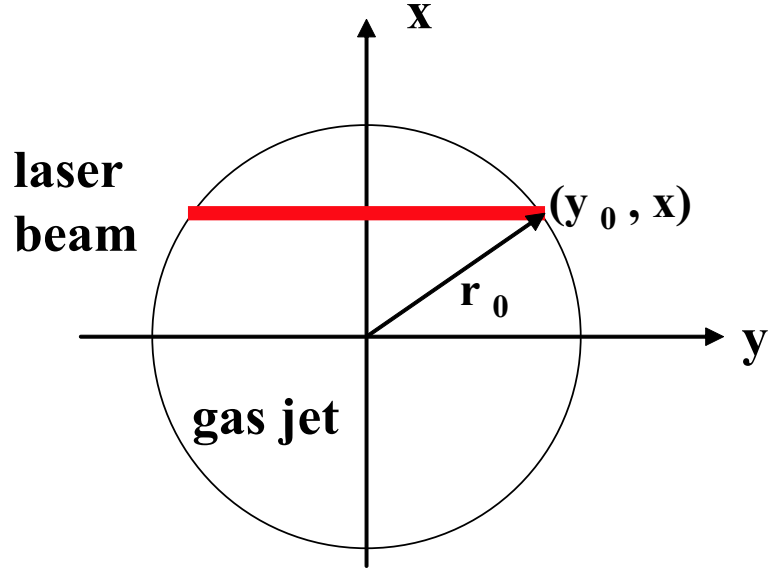


Figure 4.7: Cylindrically symmetric gas jet and Abel's transformation. The gas jet flow is normal to the paper.

Both clusters and unclustered monomers contribute to the phase shift. Then, the real refractive index change by the jet is

$$\Delta n_{jet}(r) = n_{jet}(r) - 1 = 2\pi N_g \alpha_g + 2\pi N_c \gamma_c, \quad (4.9)$$

where N_g the Ar gas density, α_g is the atomic Ar polarizability, N_c is the cluster density, and γ_c is one cluster polarizability. Simple algebra (See Appendix B) shows that the total atomic density defined by $N_{total} = N_g + N_c N_{\#}$ is

$$N_{total}(r) = \frac{\Delta n_{jet}(r)}{2\pi\alpha_g} = \frac{(n_{jet}(r) - 1)}{2\pi\alpha_g}. \quad (4.10)$$

Therefore, measured interferometry yields total atomic density information in the jet plume from the refractive index and the gas polarizability ($\alpha_g \sim 1.663 \times 10^{-24} \text{ cm}^{-3}$ for 532 nm) (Fig. 4.8). The maximum gas jet density was about 8×10^{18}

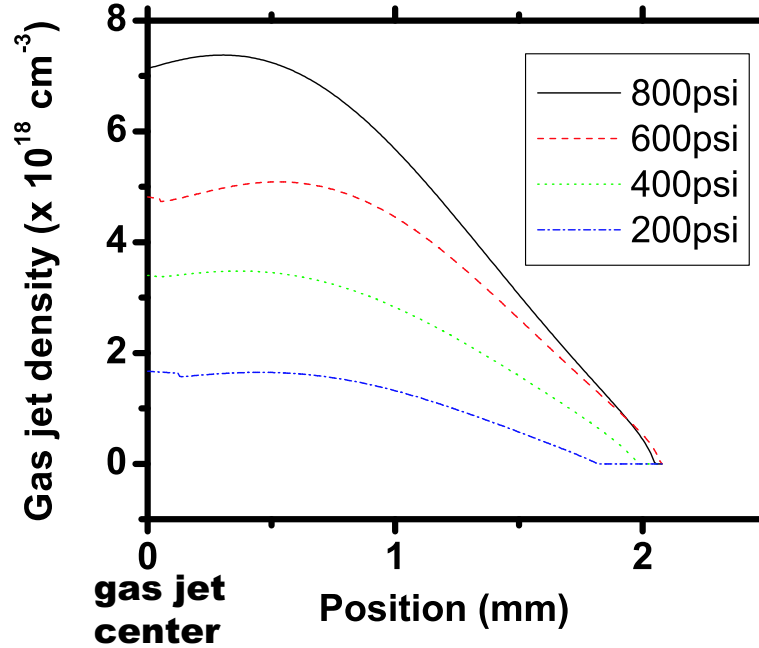


Figure 4.8: Gas jet density profile 2.5 mm downstream from the nozzle at various backing pressures.

cm^{-3} for 800 psi backing pressure and the minimum was about $2 \times 10^{18} \text{ cm}^{-3}$ for 200 psi backing pressure.

4.1.4 Conclusion

To determine the atomic density of the jet, cluster density and cluster size simultaneously, we need one more experiment or analysis. Dorchie *et al.* [31] performed a Rayleigh scattering measurement using a high pressure gas cell in which no clusters were formed as a reference to the cluster Rayleigh scattering. Then, they combined measurements (interferometry+Rayleigh scattering) with numerical simulations. To maintain a stationary regime, Dorchie *et al.* used few ms nozzle opening time like our case. Their analysis showed $\sim 80\%$ of the gas jet is nonclustered with conditions similar to our jet.

Kim *et al.* [66] also tried to determine the average sizes and density of clusters in a supersonic gas jet, using only two experiments (interferometry + Rayleigh scattering). For an incident laser beam propagating from r to $r+\Delta r$ in a clustered jet, one can obtain from Rayleigh scattering [15, 66]

$$r_c^6 N_c = \frac{1}{\pi k^4} \left(\frac{\varepsilon_c + 2}{\varepsilon_c - 1} \right)^2 \frac{\Delta E_{sca}}{E_{inc}} \frac{1}{\Delta r (\alpha^2 - \alpha^4/4)}, \quad (4.11)$$

where k is the wavenumber for an incident laser, E_{sca} is the scattered energy into a collecting lens (see Fig. 4.2), E_{inc} is the incident laser energy, α is the collection half-angle of the lens. From Eq. 4.9 and Eq. B.3, we get

$$r_c^3 N_c = \frac{\Delta n_{jet}(r) - \delta n_m}{2\pi} \left(\frac{\varepsilon_c + 2}{\varepsilon_c - 1} \right), \quad (4.12)$$

where $\delta n_m = 2\pi N_g \alpha_g$ is the index contribution of monomers. Assuming $\delta n_m=0$ and dividing Eq. 4.11 by Eq. 4.12, Kim *et al.* was able to predict average sizes of Ar clusters from $r_{c,ave} \equiv [r_c^6/r_c^3]^{1/3}$. However, their radius prediction based on measurements was too small ($4 \text{ nm} < r_{c,ave} < 7 \text{ nm}$) between 100 and 560 psi backing pressures. It is because dominant monomer contribution to the index change was neglected ($\delta n_m=0$). For example, if the index contribution of monomers is 90%, 7 nm radius for 560 psi becomes 15 nm, which reasonably agrees with Dorchie's prediction (see Table 4.1). Their measurements also indirectly confirms that most of Ar gases remain unclustered.

In our case, we used the probe absorption data and the modified nanoplasma model [23] which correctly quantifies the linear absorption by clusters. Single cluster dynamics ($\gamma_c(t)$) being determined by the model, we were able to determine the cluster density and residual gas density by analyzing the probe absorption data. I did not consider the size distribution of clusters [67, 68] specifically because the modified model can incorporate the distribution due to its empirical property. Our

analysis with 20 nm radius clusters (600 psi backing pressure) confirmed that > 80 % of the gas jet is composed of residual monomer gases, which I will discuss later.

4.2 Pump-probe absorption and third harmonic generation experiment

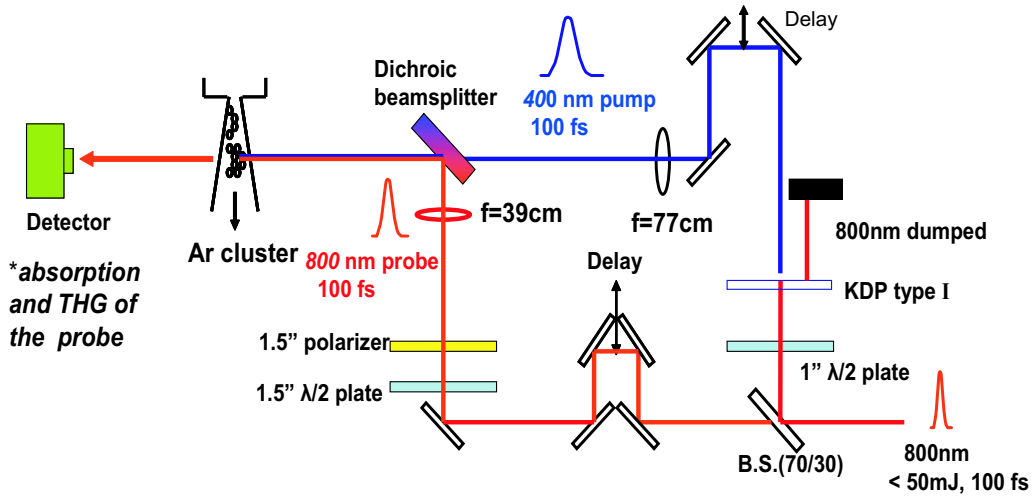


Figure 4.9: Two color pump-probe experimental set-up.

Time-resolved experiments have been performed with the Ti:Sapphire terawatt pre-amplifier is described in Chapter 3. Pump and probe beams were generated by beamsplitting the 800 nm pulse (100 fs, 1.5 inch πw_0 diameter). 400 nm, 100 fs pump pulses were generated by an 1 mm thick, type-I KDP crystal, and the remaining 800 nm served as the probe. In the probe line, we included a $\lambda/2$ plate and a thin polarizer to adjust the energy and polarization of the probe. However, all data discussed in this section were taken with parallel pump and probe polarization. I will discuss the case of perpendicular polarization in the next section. An adjustable delay consisting of two retro-reflecting mirrors mounted on a translational stage was added in the probe line. In the pump line, we inserted a 1 inch $\lambda/2$ plate

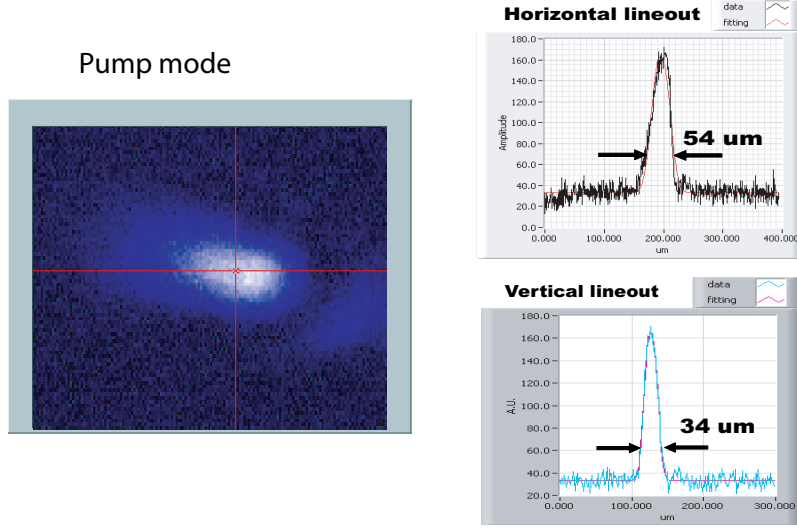


Figure 4.10: Measured pump mode.

as a polarization adjustment and as a soft aperture to generate a larger pump focus than probe focus in the interaction region. Clusters formed in the pulsed supersonic Ar gas jet described in the previous section, backed with 600 psi argon. Under these conditions, $\sim 20\%$ of the Ar atoms condensed into clusters of 20 nm average radius (see Table 4.1), while the rest remained as unclustered monomers [31]. Pump and probe beams were focused into the jet by separate singlet lenses and combined by a dichroic beamsplitter (Fig. 4.9). Focused beam diameters ($1/e^2$) are approximately $40\ \mu\text{m}$ for the pump and $30\ \mu\text{m}$ for the probe (Figs. 4.10 and 4.11).

Peak pump intensity was maintained at $I_{pump} = 10^{15}\ \text{W}/\text{cm}^2$, while probe intensity was varied over the range $2 \times 10^{13} \leq I_{probe} \leq 8 \times 10^{15}\ \text{W}/\text{cm}^2$. Non-linear interactions in the jet generated the third-harmonic $E_{THG}^{3\omega} \propto \chi^{(3)}(E_{probe}^\omega)^3$ of the probe at all delays (Δt), and a Four-Wave Mixing (FWM) signal $E_{FWM}^{3\omega} \propto \chi^{(3)}(E_{probe}^\omega)^*(E_{pump}^{2\omega})^2$ at the same frequency when the pump and the probe overlapped in time (Fig. 4.12) (see Appendix C). To separate these signals spatially, we intersected pump and probe beams at a small angle ($\sim 2^\circ$), so that THG and FWM

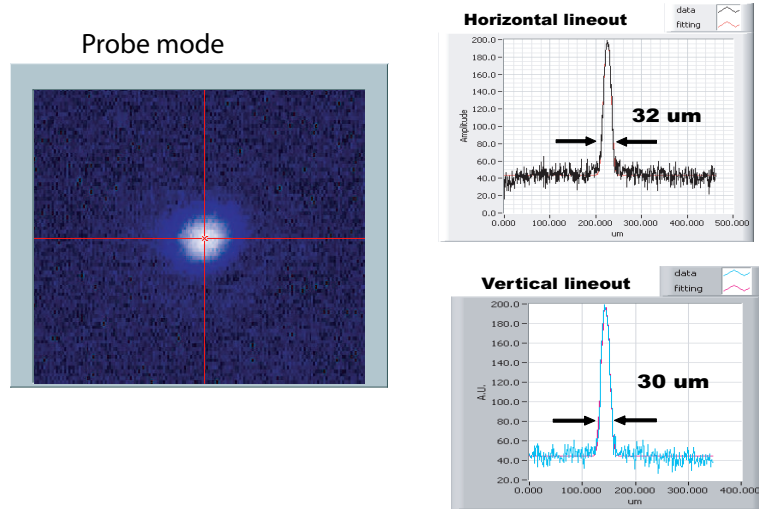


Figure 4.11: Measured probe mode.

signals propagated in different directions governed by momentum conservation. The FWM signal was then blocked after the interaction region. Pump and probe passed through an off-center chord (about 2 mm away from the jet center) of the circular gas jet profile 2.5 mm from the nozzle, with path length ~ 1 mm matched to the length of the pump-probe overlap (see Fig. 4.13). In this configuration probe defocusing by its self-created plasma lens and pump-induced probe refraction [21, 22, 69], were both negligible. A Mach-Zehnder interferometer (see Fig. 4.8 and 4.13) measured average atomic density $\sim 10^{18} \text{ cm}^{-3}$ at about 2 mm away from the jet center. The THG light was collected and focused onto a spectrometer slit using an $f/4$ lens. A large aperture (~ 1 cm) photo-multiplier tube (PMT - 1P28B from Burle) with quantum efficiency 13 % at 266nm collected all the dispersed light at the output of the spectrometer. A 265 nm bandpass filter placed in front of the PMT helped discriminate other colors. The PMT signal was amplified ($\times 5$) in a fast pre-amplifier, then averaged using a digitizing oscilloscope. In addition to THG, we measured the time-resolved probe absorption using a $f/4$ probe collecting lens, a red glass filter,

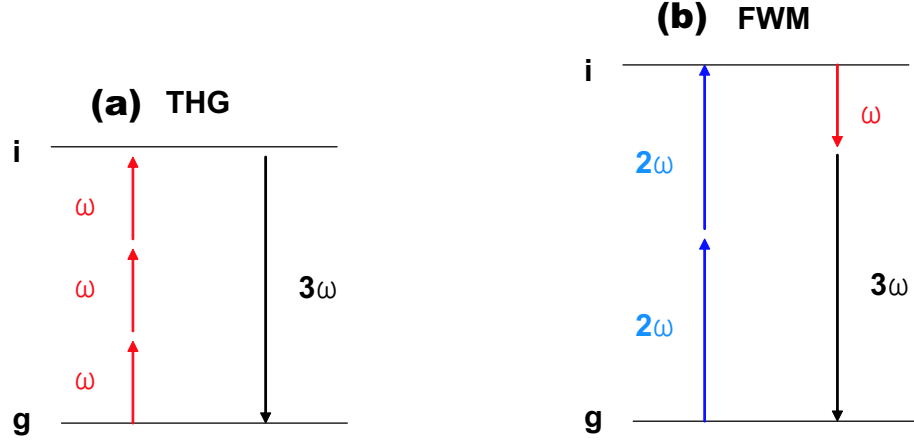


Figure 4.12: (a) THG: three probe (ω) photons are absorbed and one 3ω photon is generated. (b) FWM: two pump (2ω) photons are absorbed and one ω probe photon, one 3ω photon are created.

and energy meter. We also imaged probe modes from the gas jet exit onto a CCD camera (see Fig. 4.19) to check for self-focusing or defocusing.

Figure 4.14(a) shows the THG and probe absorption measurement when the probe was weak ($2 \times 10^{13} \text{ W/cm}^2$). There is a short duration enhancement of the THG when the pump starts to ionize the clusters and residual gases ($\Delta t_{delay} \sim -150 \text{ fs}$), compared with a broad absorption resonance at later delays. After the early delay enhancement, the THG from the clustered plasmas is smaller than from the non-ionized medium. The signal was averaged over 300 shots. To check the signals near $\Delta t=0$ were cluster-related, we performed a control experiment with same geometry using He (unclustering gas). No time-dependent 3ω signal was observed within experimental error (Fig. 4.14(b)). In contrast, He FWM signal was clearly observed in a collinear geometry (Fig. 4.14(c)).

We performed a probe intensity scan with the fixed pump intensity (10^{15} W/cm^2) (Fig. 4.15 (a)). As I_{probe} increased, the peak at $\Delta t < 0$ saturated (Fig. 4.15 (a), left), and another short duration peak at $\Delta t \sim 260 \text{ fs}$ appeared and rapidly grew

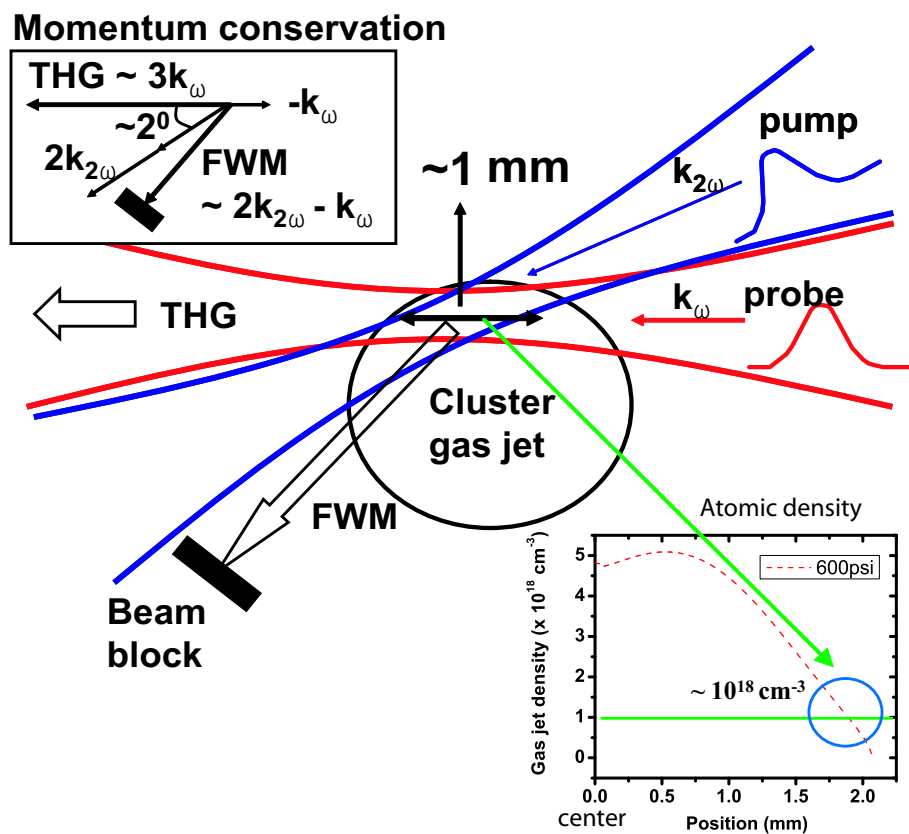


Figure 4.13: Non-collinear pump-probe geometry and momentum conservation.

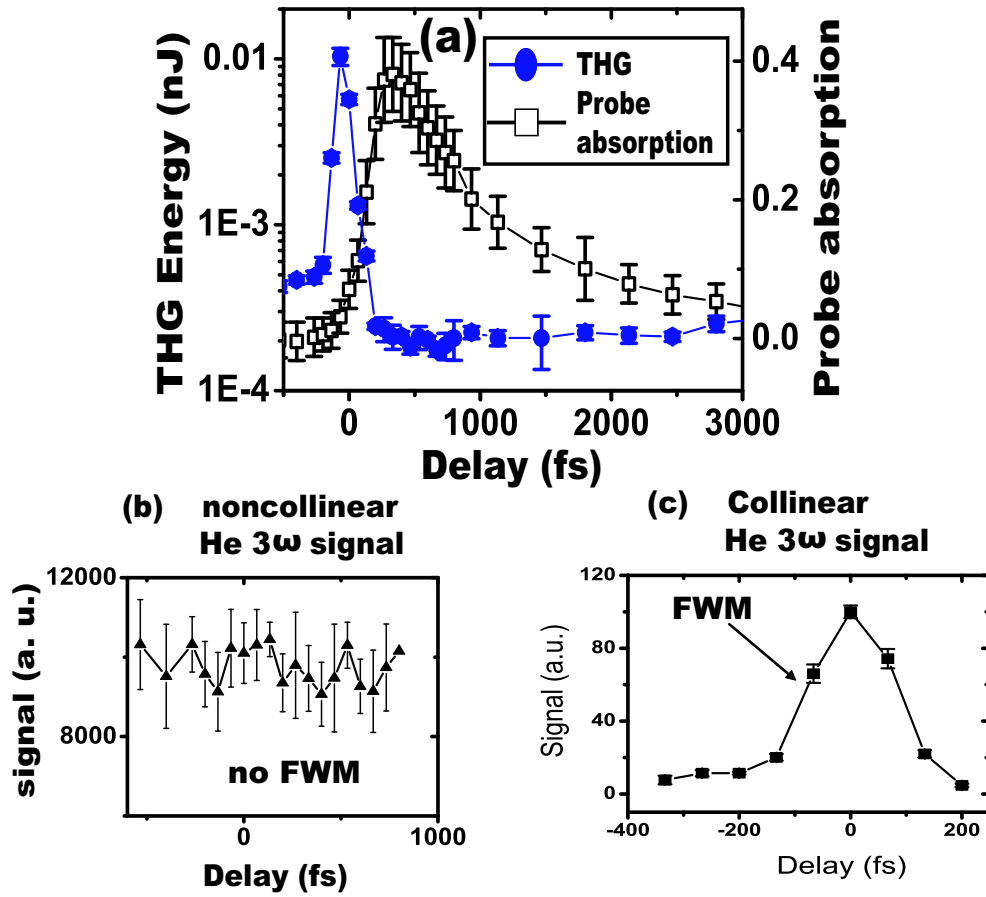


Figure 4.14: (a) Pump-weak probe THG vs absorption with 20nm average radius clusters. (b) Helium (160 psi) 3ω signal-check with $I_{pump} \sim I_{probe} \sim 8 \times 10^{14}$ W/cm². (c) Collinear Helium (200psi) 3ω signal-check.

(Fig. 4.15 (a), right). The former peak scaled as I_{probe}^3 when $I_{probe} < 10^{14}$ W/cm² (Ar ionization threshold), but saturated as probe self-ionization occurred (Fig. 4.15 (b)). The delayed peak, on the other hand, scaled as I_{probe}^3 without saturation up to $I_{probe} = 10^{15}$ W/cm² (Fig. 4.15 (c)) because of fast ionization completion by the pump [14, 20] and began to saturate only at higher probe intensities. Abrupt termination of the delayed THG peak at $\Delta t > 300$ fs is evidently caused by the sharp rise of probe absorption (Fig. 4.16).

We tried the pump-probe experiment at the center of the jet where the jet thickness ~ 4 mm, determined by interferometry and Rayleigh scattering measurements (see Fig. 4.2 and 4.8), greatly exceeds the length (~ 1 mm) of the pump-probe overlap region. Here the pump intensity was 1.5×10^{15} W/cm² and the probe intensity was 2.6×10^{14} W/cm². The probe-generated TH signals quickly decreased as ionization in the gas jet started ($\Delta t \approx -100$ fs) (Fig. 4.17 and 4.18), then reached a minimum when the maximum of the probe absorption occurred, then slowly increased as the probe absorption decreased. Clearly the THG signal simply tracks absorption. Strikingly, we could not see any TH signal enhancement in this configuration. We believe that probe propagation in the 3 mm long region of unpumped gas may have been significantly disturbed by self-focusing or defocusing. We did not check this hypothesis directly for the experiments performed at jet center. However, we did check carefully for probe self-focusing in the off-jet-center geometry, in which strong resonant enhancement of THG was discovered. This was done by imaging the probe from the output of the gas jet onto a CCD (Fig. 4.19). Pump-induced probe focusing in the gas jet could contribute to probe intensity increase and thus to an enhancement of the third harmonic signal unrelated to nonlinear Mie resonance.. According to time-resolved beam size analysis (Fig. 4.20(a)), there is a small probe focusing effect (~ 10 % decrease) between 0 fs and 300 fs, followed by gradual defocusing. Here W_y is the spot size in the direction of pump polarization. Overall,

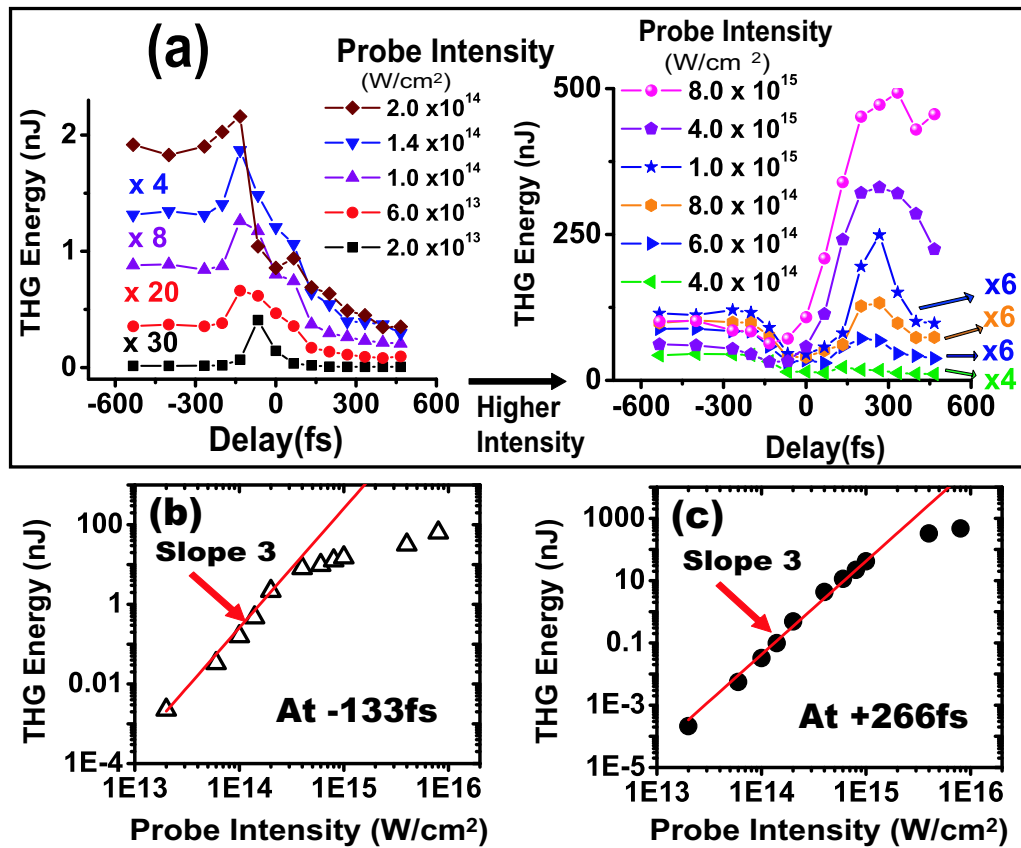


Figure 4.15: (a) Time-dependent, probe THG from jet of 20nm average radius Ar clusters ionized and heated by pump at intensity 10^{15} W/cm², for various probe intensities with parallel pump and probe polarizations. (b) Power law dependence of early THG peak. (c) Power law dependence of delayed THG peak.

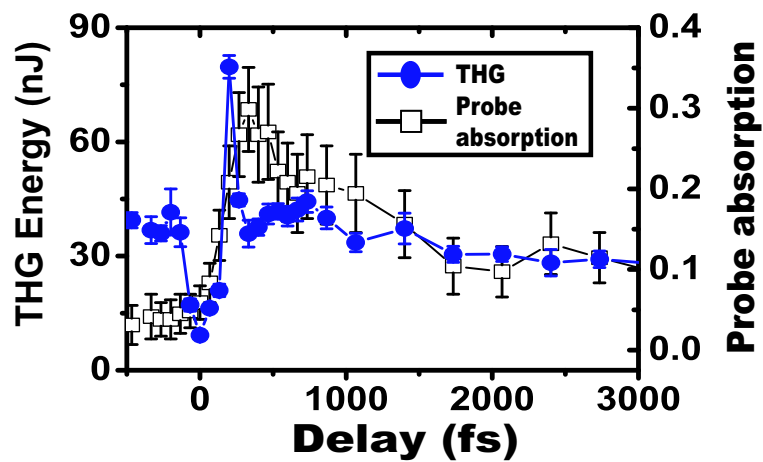


Figure 4.16: Pump-strong probe THG vs absorption with the probe intensity 10^{15} W/cm².

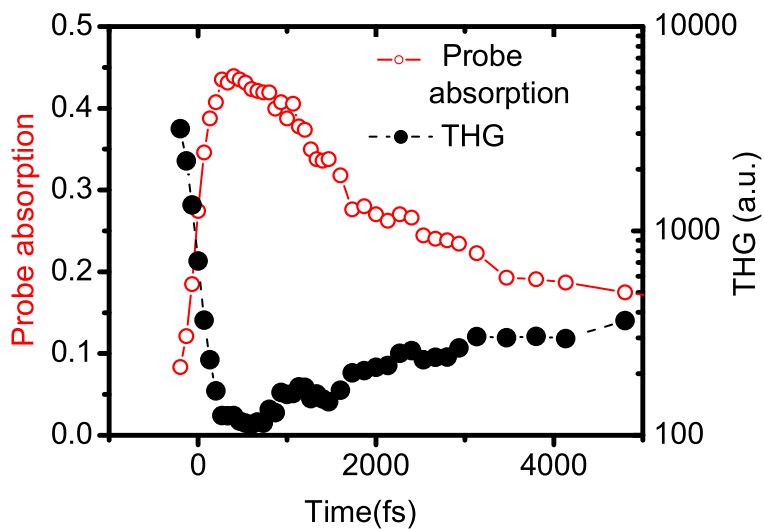


Figure 4.17: Pump-probe THG vs absorption with 20nm argon clusters (600 psi backing pressure) at the jet center.

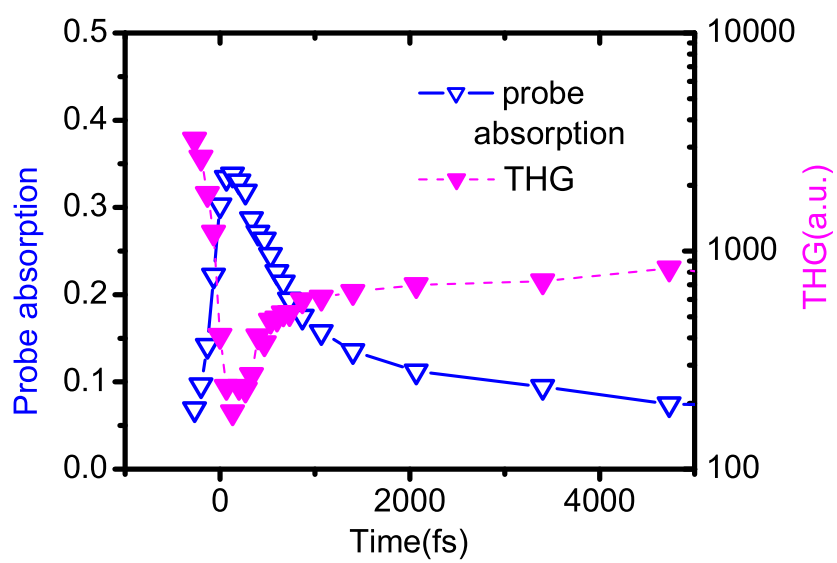


Figure 4.18: Pump-probe THG vs absorption with 10nm argon clusters (200 psi backing pressure) at the jet center.

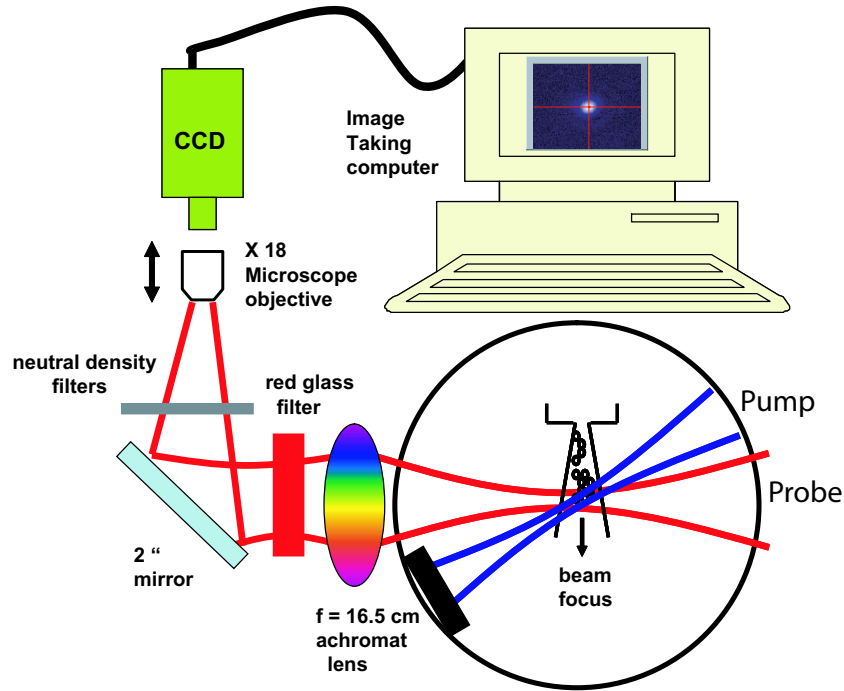
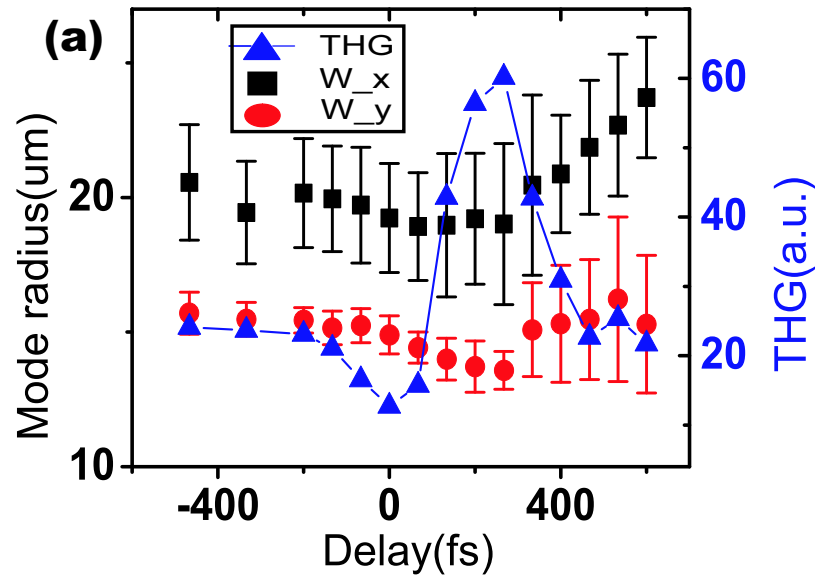


Figure 4.19: Probe mode measurement set-up.

the time scale agrees with the data taken by other groups [22, 69] even though the effect was small because of the short path length ($\sim 1\text{mm}$) at the edge of the jet plume. Although defocusing (Fig. 4.20(a)) partially contributes to the drop in THG for $\Delta t > 300\text{ fs}$, the strong THG enhancement at $\Delta t \simeq 260\text{ fs}$ cannot be explained by the 10 % probe focusing. This slight focusing is more than compensated by the absorption increase during the same time. As a result, probe intensity $\Delta t \simeq 260\text{ fs}$ is actually weaker than for $\Delta t \leq 0\text{ fs}$. THG enhancement is clearly caused by a nonlinear Mie resonance, increased coherence length, or both.

Although we used a large aperture ($\sim 1\text{ cm}$) PMT, there is a possibility of not collecting all the generated THG if ionization-induced frequency shifts occur. Fig. 4.21 shows a normalized THG spectrum at different delays. When the jet medium underwent ionization ($\Delta t = -66\text{ fs}$), there was induced a small blue shift



(b) Probe mode images

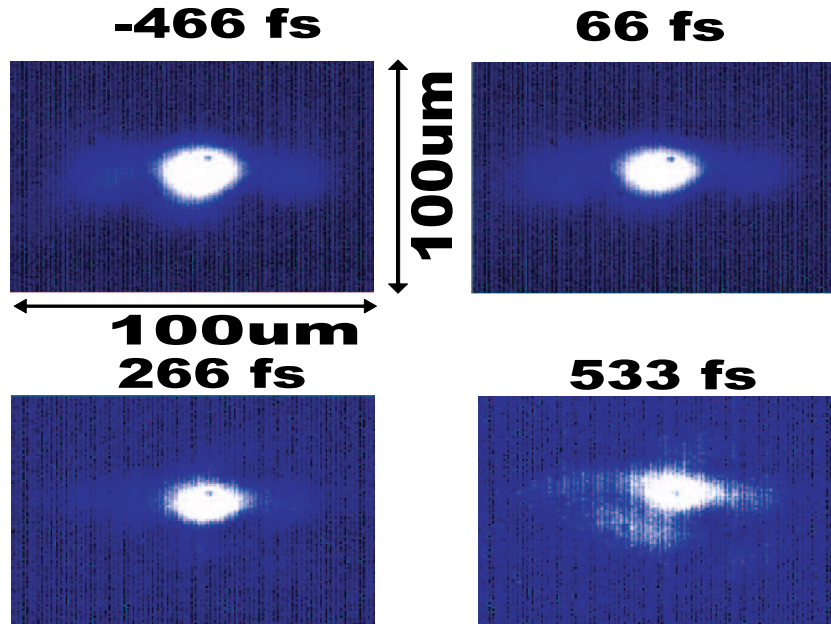


Figure 4.20: Time-resolved probe refraction measurements from the 20 nm clustered jet. The peak intensity was $1.0 \times 10^{15} \text{ W/cm}^2$ for both pump and probe. (a) Beam radius change. (b) Examples of probe modes.

($\Delta\lambda \sim 1$ nm) in the third harmonic spectrum, caused by the rapid decrease in index of refraction [70]. Assuming a uniform medium, the transient wavelength shift in the clustered jet ionization is [24]

$$d\lambda = (cL\lambda) \frac{d}{dt} \left(2\pi n_c \gamma_c(t) - \frac{1}{2} \frac{n_{p.coro}(t)}{n_{cr}} \right), \quad (4.13)$$

where c is the speed of light, L is the medium length, $n_{p.coro}$ is the coronal plasma density from unclustered monomer gases, and $n_{cr} = m_e \omega^2 / 4\pi e^2$ is the critical plasma density. In an unclustered gas, a blue-shift occurs only during ionization ($n_c=0$, $dn_{p.coro}(t)/dt > 0$). However, the increase of cluster polarizability (γ_c) during cluster expansion (see Chapter 2) induces a red-shift in the probe-generated THG spectrum ($\Delta t = 200$ fs). At longer delays, the spectrum shifts back toward the original wavelength, indicating a slowing of γ_c dynamics (see $\Delta t = 600$ fs spectrum). The spectral red-shift is, therefore, an unique property of expanding clusters.

4.3 Analysis: comparison with simulation results

To analyze the experimental data, we performed cluster jet simulations using the modified nanoplasma model [23] which predicts the linear cluster polarizability correctly (see Chapter 2). First, in order to determine the ratio of clusters and monomer gases, I calculated the probe absorption after excitation by the pump (400 nm, 100 fs, $I_{pump} = 1 \times 10^{15} W/cm^2$) by

$$A = 1 - \exp(-\alpha L), \quad (4.14)$$

where α is the absorption coefficient by

$$\alpha = 2 \frac{\omega}{c} \left(2\pi n_c \text{Im} \left(\frac{\varepsilon_c - 1}{\varepsilon_c + 2} \right) r_c^3 \right), \quad (4.15)$$

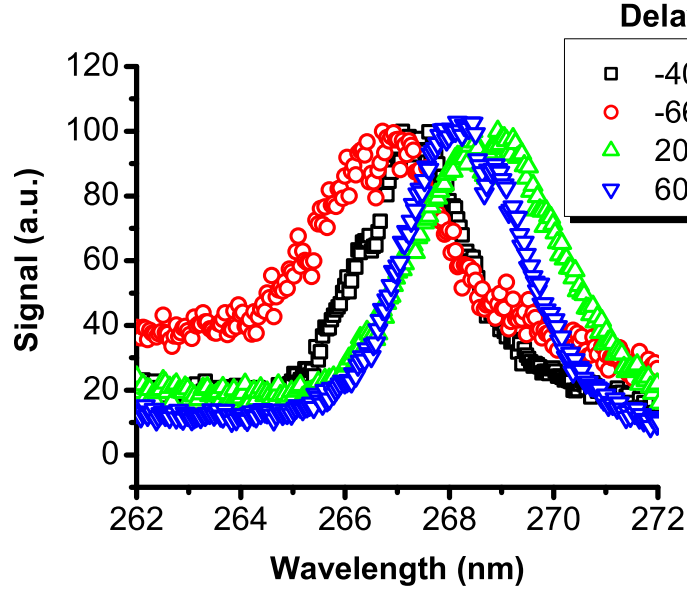


Figure 4.21: Time-resolved THG spectrum from the 20nm clustered jet. The pump and the probe peak intensity was $1.0 \times 10^{15} \text{ W/cm}^2$.

and $L = 1 \text{ mm}$ is the gas jet length. Therefore, ignoring the small absorption from the monomer gases, the cluster density (n_c) determines the probe absorption. Fig. 4.22 compares the probe absorption data with 20 nm radius clusters when the probe was weak ($I_{probe} = 2 \times 10^{13} \text{ W/cm}^2$) (open squares) with the absorption calculation using the model (red solid curve) when the ratio of monomer/cluster density was 92 % monomers, 8 % clusters. Here I assigned 100 a.m.u for the ion mass. The calculation shows a good fit of the observed data for $\Delta t \leq 1 \text{ ps}$. Considering that the power-meter measurement underestimated the absorption compared with the CCD measurement (compare the power-meter measurement (Fig. 4.16) and CCD measurement (Fig. 4.27)), we expect that the fraction of clusters in the jet is approximately between 10 and 20%, which confirms that the gas jet is mostly composed of unclustered gas and matches well with the measurement by Dorchie

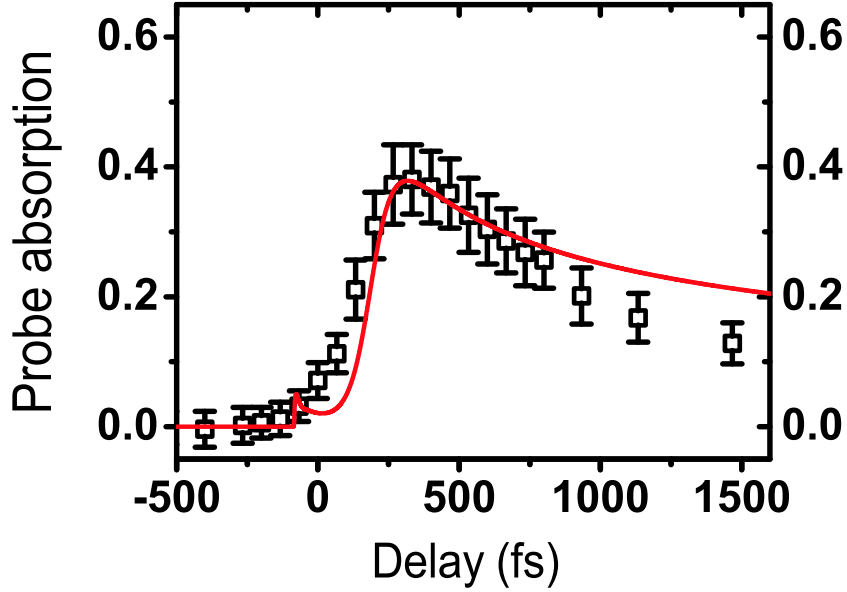


Figure 4.22: Probe absorption data (open squares) and calculation (red solid curve) when the ratio of monomer/cluster density was 92 % monomers, 8 % clusters.

et al. [31]. I will calculate the third harmonics, assuming 15% of clusters in the jet.

For probe-generated THG calculation, we included heating and ionization by both pump and probe [71]. In the two color calculation, the laser electric field is given

$$E(t) = E_{pump}(t) + E_{probe}(t) = E_1(t) \exp(i\omega_1 t) + E_2(t + \Delta t) \exp(i\omega_2(t + \Delta t)), \quad (4.16)$$

where ω_1 (ω_2) is the pump (probe) laser frequency, and Δt is the delay between the pump and probe. The cluster electric field is then calculated by

$$E_c = E_{c.pump}(t) + E_{c.probe}(t) = \frac{3E_{pump}(t)}{|\varepsilon_{c.pump} + 2|} + \frac{3E_{probe}(t)}{|\varepsilon_{c.probe} + 2|}. \quad (4.17)$$

Here $\varepsilon_{c.pump}, c.probe$ are calculated for each frequency (see Eq. 2.29). In particular, I

used a weighted collisional frequency which can be written

$$\nu(t) = \frac{15}{T_e^{1/4}(t)} \left(\frac{\omega_1 I_{pump}(t) + \omega_2 I_{probe}(t)}{I_{pump}(t) + I_{probe}(t)} \right), \quad (4.18)$$

where $I_{pump}(t)$ ($I_{probe}(t)$) is the pump (probe) laser intensity. The Bremsstrahlung heating was calculated by

$$\frac{\partial U}{\partial t} = \frac{\omega_1}{8\pi} \text{Im}(\varepsilon_{c.pump}) |E_{c.pump}|^2 + \frac{\omega_2}{8\pi} \text{Im}(\varepsilon_{c.probe}) |E_{c.probe}|^2. \quad (4.19)$$

The probe generated THG field due to $\chi^{(3)}$ in the jet (see Eq. 2.28), then, is [72]

$$J_{3\omega}(L) \equiv \frac{(e^{i\Delta k L - 3\beta^\omega L} - e^{-\beta^{3\omega} L})}{(i\Delta k - (3\beta^\omega - \beta^{3\omega}))}, \quad (4.20)$$

$$E^{3\omega}(L) = \frac{i2\pi(3\omega)^2}{c^2 k_{3\omega}} \chi^{(3)} J_{3\omega}(L) E_{probe}^3, \quad (4.21)$$

where L is the gas jet length (1 mm), Δk is the phase mismatch between 800 nm and 266 nm, and β^ω and $\beta^{3\omega}$ are imaginary wavenumbers for 800 nm and 266 nm. Here we defined $J_{3\omega}(L)$ as the phase matching function including absorption, which becomes the phase matching function for a loose focusing case ($\left[\frac{\exp(i\Delta k L) - 1}{i\Delta k} \right]$) if the absorption is neglected ($\beta^\omega = \beta^{3\omega} = 0$) [38, 72].

Before evaluating Eq. 4.21, I briefly consider another source of THG, not included explicitly in Eq. 4.21, introduced by Brunel [73]: the current from electrons undergoing tunneling ionization from unclustered gas atoms. Because tunneling ionization peaks sharply twice in each laser cycle (Fig. 4.23), the electron density (n_e) has second-harmonic content. Since the quiver velocity v_e oscillates at the laser frequency, the free electron current density $J = -n_e e v_e$ has third-harmonic content. The wave equation for the third-harmonic field $E_{ic}^{3\omega}$ generated by this ionization

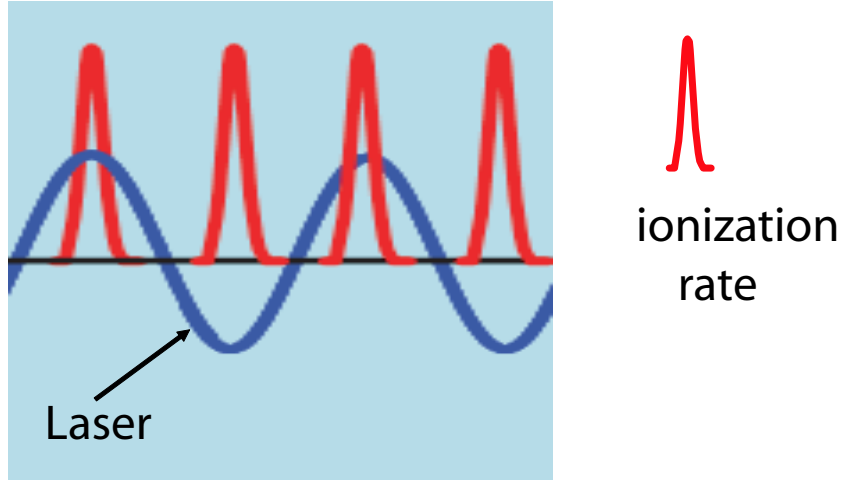


Figure 4.23: Ionization rate. Ionization occurs twice in each laser cycle.

current is then

$$\nabla \times (\nabla \times E_{ic}^{3\omega}) + \frac{1}{c^2} \frac{\partial^2 E_{ic}^{3\omega}}{\partial t^2} + \underbrace{\frac{4\pi}{c^2} \frac{\partial J}{\partial t}}_{\text{harmonic source}} = 0. \quad (4.22)$$

Brunel showed that $E_{ic}^{3\omega}$ is

$$E_{ic}^{3\omega} = -\frac{P k_L}{24\pi} \frac{n_g}{n_c} \left[\frac{\exp(i\Delta k_{i.c} L) - 1}{i\Delta k_{i.c}} \right] \times \left[\exp\left(-\frac{3}{\zeta}\right) + 0.5 \exp\left(-\frac{12}{\zeta}\right) \right] E_0, \quad (4.23)$$

Here k_L is the ionizing laser wave number, P is the probability of ionization over one laser cycle ($P \approx \int_0^{2\pi/\omega_L} w(t) dt$) with $w(t)$ the ionization rate, n_g is the monomer gas density, n_c is the laser critical density, $\Delta k_{i.c}$ is the ionization current phase mismatch $\Delta k_{i.c} \approx -k_L n_p / n_c$ with n_p plasma density, and $\zeta = E_a / E_0$ with E_a the atomic electric field (5.1×10^9 V/m) and E_0 the incident probe field. I included ionization currents from all charge states using an adiabatic approximation of ADK

ionization rates [74]. In that case,

$$P = 2\sqrt{3\pi} \frac{\omega_a}{\omega_L} \left(\frac{4eZ^3}{n^*} \right)^\beta \left(\frac{eZ^2}{2\pi n^*} \right) \left(\frac{E_a}{E_0} \right)^\beta \zeta^{-\frac{1}{2}} \exp\left(-\frac{2}{3}\zeta\right), \quad (4.24)$$

where ω_a is the atomic frequency ($4.1 \times 10^{16} \text{ s}^{-1}$), ω_L is the laser frequency, e is $\exp(1)$, Z is the charge state of the ion, n^* is the effective principal quantum number ($n^* = Z(I_p/I_h)^{-0.5}$), I_p is the ionization potential in eV , I_h is the ionization potential of hydrogen (13.6 eV), and β is $2n^* - 1$. I used the phase matching function Eq. 4.20, replacing Δk with the ionization current phase mismatch ($\Delta k_{i.c}$). Fig. 4.24 shows that calculated THG energy of ionization currents from the gas jet irradiated by a single 800 nm, 100 fs laser pulse with different intensities. Above Ar ionization threshold ($\sim 10^{14} \text{ W/cm}^2$), the THG energy from the ionization currents quickly increases but saturates at higher intensity. The overall efficiency of THG from ionization currents is very low ($< 10^{-7}$). We can therefore conclude that THG from ionization currents is small compared to THG from clusters described by Eq. 4.21 (see Fig. 4.15).

The total TH field is the sum of $E^{3\omega}$ (Eq. 4.21) and $E_{ic}^{3\omega}$ (Eq.4.23). They were calculated as follows. First, given pump and probe intensities and delay, I simulated the gas jet-two (pump+probe) color interaction self-consistently using the Runge-Kutta step size control method [30] to evaluate the linear optical properties $\beta^{\omega,3\omega}$, Δk , etc. Then, from these numbers, I calculated the third harmonic generated by the probe in each time-step using Eqs. 4.21 and 4.23. The microscopic nonlinearity parameter ζ/r^2 (see Eq. 2.25) that enters $\chi^{(3)}$ was held constant for simplicity as time was stepped, and was adjusted empirically for best overall fit to the delay peak. Then, I used the Trapezoidal rule [30] to integrate the probe-generated THG. Fig. 4.25(a) shows the result of the calculation of probe-generated THG energy vs. delay (Δt) for the experimental range of probe intensity. The result is hardly changed if the ionization currents contribution is neglected as discuss. The simulation cor-

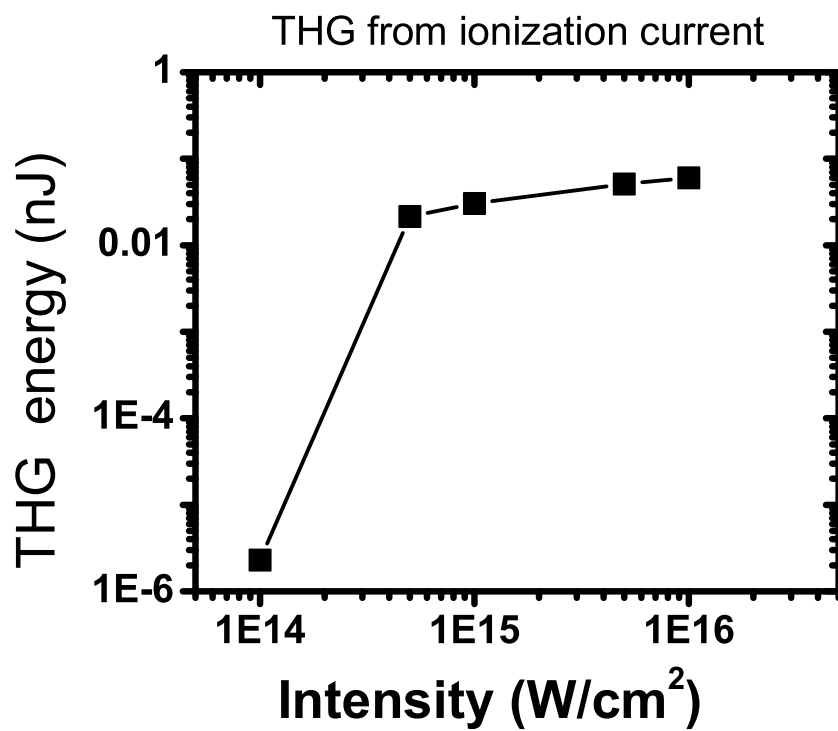


Figure 4.24: Calculation of ionization currents of monomer gases from the gas jet ($0.85 \times 10^{18} \text{ cm}^{-3}$ monomer + $0.15 \times 10^{18} \text{ cm}^{-3}$ clustered gas) irradiated by a single 800 nm, 100 fs laser pulse with different intensities.

rectly reproduces the nearly unsaturated growth of the delayed THG peak (see Fig. 4.25(b)), showing weak saturation with $I_{probe} \geq 4 \times 10^{15} W/cm^2$. The high intensity probe ($I_{probe} \geq 4 \times 10^{15} W/cm^2 > I_{pump}$) ionizes residual gas ions left unionized by the pump, and thus increases phase mismatch. The resulting decreased coherence length accounts for partial THG saturation. Additional saturation is caused by the increased ionization-induced defocusing of the probe, but this was not included in the calculation. The weak saturation observed as $I_{probe} \rightarrow 10^{16} W/cm^2$ may be fundamental to THG of expanding clusters. However we have not ruled out the possibility that it is an artifact caused by pre-expansion of clusters by weak pre-pulses in the laser system.

Heating by the probe makes the linear polarizability and the $\chi^{(3)}$ of the clustered jet increase slowly as the probe intensity increases. Therefore, the calculated THG grows as $I_{probe}^{3.72}$ (see Fig. 4.25(b)) instead of I_{probe}^3 . Here, to reproduce the observed THG, we put $\varsigma/r^2 \approx 50r_c^{-2}$, which is a much bigger anharmonic constant compared with the theoretical predictions based on the uniformly expanding clusters [28, 27]. This shows that the scale length r of electron and/or ion density nonuniformity responsible for THG is much less than the cluster radius r_c . The ponderomotive force effect due to a non-uniform electron density gradient for large clusters [20, 75] can be an important factor reducing this scale length. Near resonance, the ponderomotive force, which is not considered in this model or in Ref. [27], becomes significant at a local critical surface and produces nonlinear electron motion with strong harmonic components. Although we assumed the anharmonic strength being constant in the calculation, if the ponderomotive force of the probe involves, it can also vary for different probe intensities.

In Chapter 2, I discussed that the coherence length of the jet increases almost simultaneously with the third harmonic resonance of the cluster. Fig. 4.26 shows that $|J_{3\omega}(L)|^2$ decreases sharply from 0.01 cm^2 (square of the interaction length)

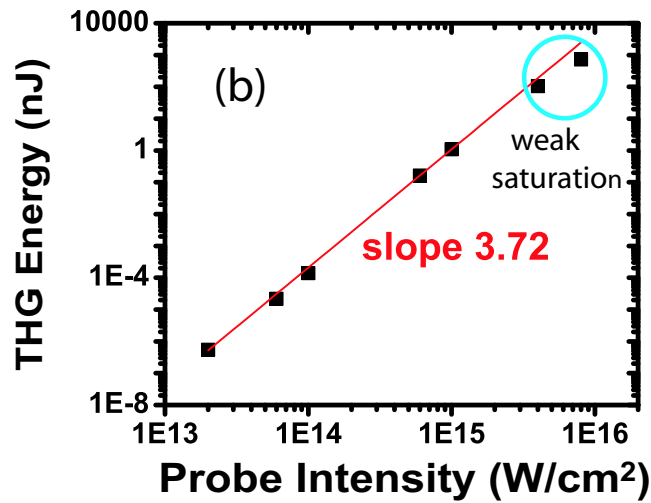
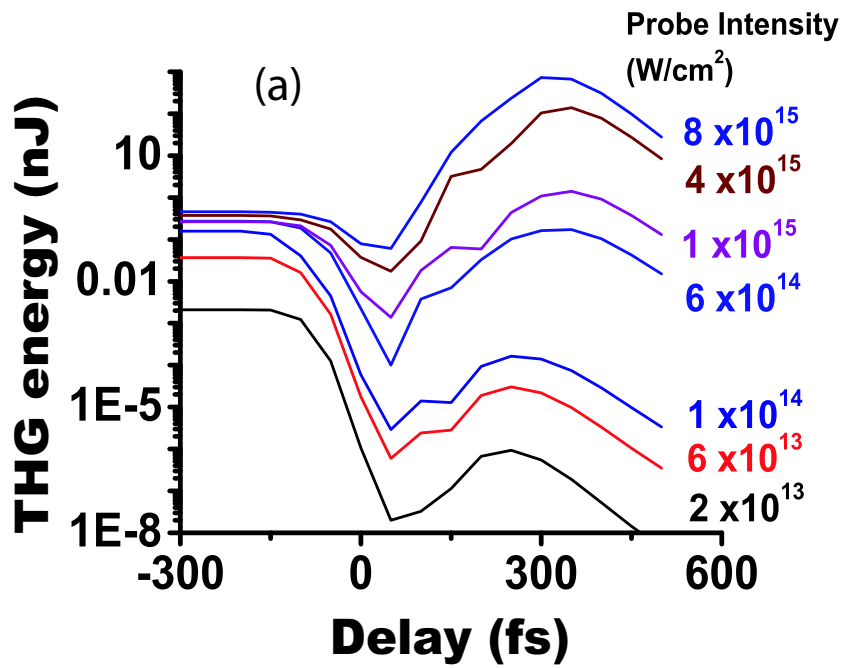


Figure 4.25: THG simulation considering both ionization and heating by the probe. (a) Time dependent THG by 800nm probe pulses of indicated intensities. (b) Probe intensity dependence of calculated THG at $\Delta t = 300$ fs.

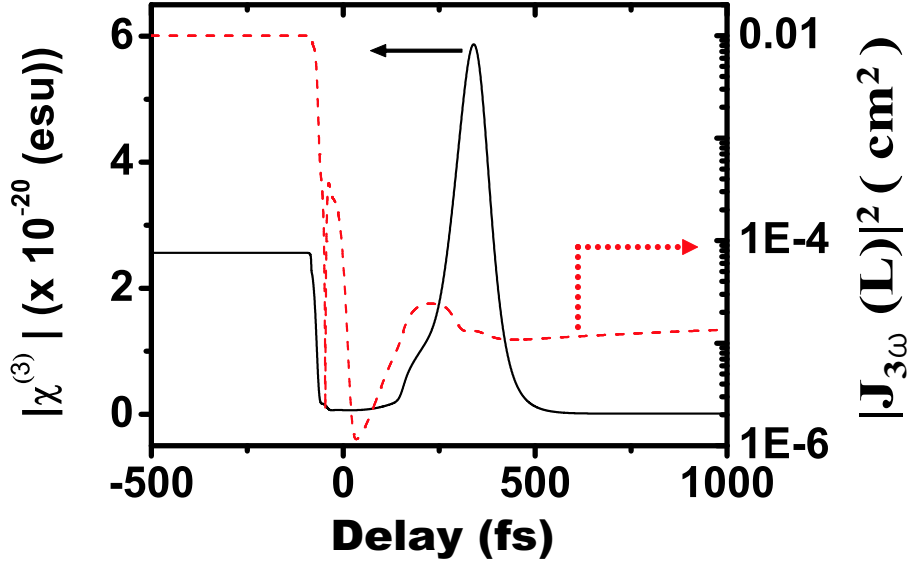


Figure 4.26: Time dependent $|J_{3\omega}(L)|^2$ (dashed curve) and $|\chi^{(3)}|$ (solid curve) with $I_{probe} = 10^{15}W/cm^2$ and $\Delta t = 300$ fs after the pump excitation ($I_{pump} = 10^{15}W/cm^2$, 400 nm), considering ionization and heating by both pump and probe.

upon ionization. Thus, the ionized medium is less phase-matched than unionized gas jet. However, $|J_{3\omega}(L)|^2$ increases locally near at $\Delta \simeq 200$ fs, when $n_{jet}(3\omega)$ and $n_{jet}(\omega)$ reconverge. This increase thus contributes to the delayed THG enhancement combined with the $|\chi^{(3)}|$ resonance. The calculations show that $n_{jet}(3\omega)$ and $n_{jet}(\omega)$ can be equal near at $\Delta \simeq 200$ fs, resulting in perfect phase-matching, with higher cluster/monomer gas ratio, possibly in a cryogenic argon jet [41, 42], which will be discussed briefly in the final chapter.

As shown in Figs. 4.15 and 4.25, the model predicts about 2 orders of magnitude smaller THG than the experimental data at negative delays when only the probe affected the jet medium. We think that one of the possible reasons is due to the early THG resonance enhancement which was observed with the weak probe (see Fig. 4.14). Although the model cannot predicts the $\chi^{(3)}$ resonance at $\Delta t \simeq -100$ fs, it seems that there is an additional resonance when ionization starts to occur

and the cluster electron density sweeps quickly through ω and 3ω resonances. The enhancement with the weak probe is about 2 orders of magnitude compared with the unionized medium, which would contribute to the probe generated THG with higher intensities ($I_{probe} > 10^{14}W/cm^2$) in $\Delta t \leq -100$ fs - *i.e.*- the early resonance occurs within the probe pulse temporal profile, which generate more THG than the calculation.

Generally, even for a pure gaseous medium undergoing ionization, calculation for high harmonics is very difficult [76]. For example, Liu *et al.* [77] measured the I^3 power law dependence of THG, using laser pulses which completely ionized hydrogen gases in a cell target. There, the contribution from the ionization current should be saturated due to complete ionization of hydrogen at higher than saturation intensity ($I_s \sim 2 \times 10^{14}W/cm^2$) and it is not clear what factors contributed to the THG enhancement with $I > I_s$. Other experimental results [40] also indicate the difficulty in theoretical predictions for the harmonic generation from the ionizing gases. A very sophisticated THG model is needed to explain the data more correctly.

In summary, simulations show that the nonlinear susceptibility $\chi^{(3)}$ of the individual clusters and the coherence length of the clustered plasma medium are optimized nearly simultaneously as the pre-heated clusters expand, and both contribute to the observed THG enhancement.

4.4 Anisotropy of THG from a clustered plasma.

So far we have considered experiments and calculation only for co-polarized pump and probe pulses. THG experiments with variable angle between pump and probe polarization are excellent ways to detect transient anisotropy in the expansion of the clusters. Fig. 4.27 clearly indicates that the perpendicular case shows more enhancement of THG than the parallel case. The anisotropy in time-integrated production of ions and electrons from Coulombically exploding (*i.e.* fully ionized)

small clusters has been reported and theoretically analyzed [19, 78, 79]. But, to our knowledge, this is the first measurement of harmonic generation anisotropy from hydrodynamically expanding (weakly ionized, but strongly heated) clusters. Femtosecond harmonic generation (HG) has the unique capability to time-resolve transient anisotropy, and to characterize anisotropy in clustered plasmas that are too dense for electrons and ions to escape [72]. In comparison, no anisotropy was observed in time-resolved linear absorption (see Fig. 4.27) within experimental error. Here, the absorption data was taken from the imaged probe modes by averaging 50 shots (see Fig. 4.19) and the anisotropy measurements were averaged over 100 shots. The anisotropy in THG was observed at higher intensities (Fig. 4.28), too. This illustrates a general principle of nonlinear optics that HG more sensitively probes material anisotropy than linear optics [72]. The maximum conversion efficiency was about 7×10^{-4} with probe peak intensity 4.0×10^{15} W/cm² and the conversion efficiency saturated at higher intensities as in the case of parallel polarization (see Fig. 4.15(c)).

We also performed an optical Kerr effect (polarization rotation effect) [72] in the clustered medium (Fig. 4.29). The input polarization was rotated by 45° with respect to the pump polarization. We put a cube polarizer to separate two probe polarization components (parallel and perpendicular to the pump polarization) and measured transmitted probe signals using photodiodes. As shown in Fig. 4.30, no visible probe polarization rotation was observed with experimental error.

Breizman *et al.* [29] suggested a physical mechanism for anisotropic hydrodynamic expansion of weakly ionized, laser-heated clusters: polarization-dependent vacuum heating [80, 81] by the pump accompanied by collisional absorption should generate an anisotropic electron pressure that is higher along the pump field axis. As a result, ion acceleration driven by this pressure becomes anisotropic, causing the expanding cluster to become ellipsoidal with major radius along the pump field.

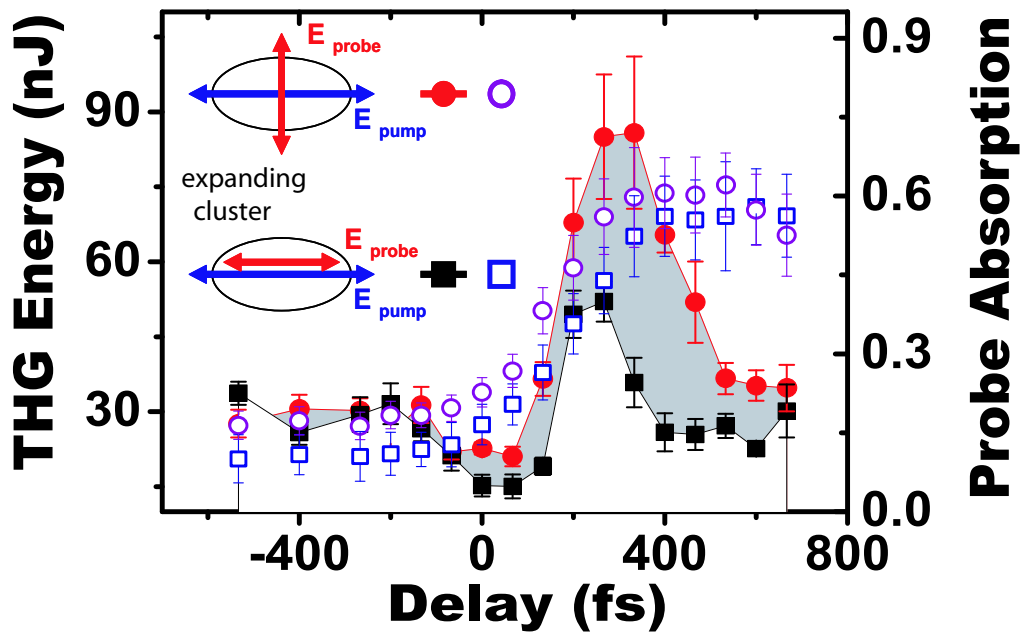


Figure 4.27: THG anisotropy in hydrodynamically expanding clusters from 600 psi backing pressure with parallel (filled squares) or perpendicular (filled circles) polarizations. Each THG data point represents an average over 100 shots. Probe absorption was same for parallel (open squares) and perpendicular (open circles) pump and probe polarization. Each absorption data point was taken using imaged probe modes onto a CCD camera with 50 shot averages.

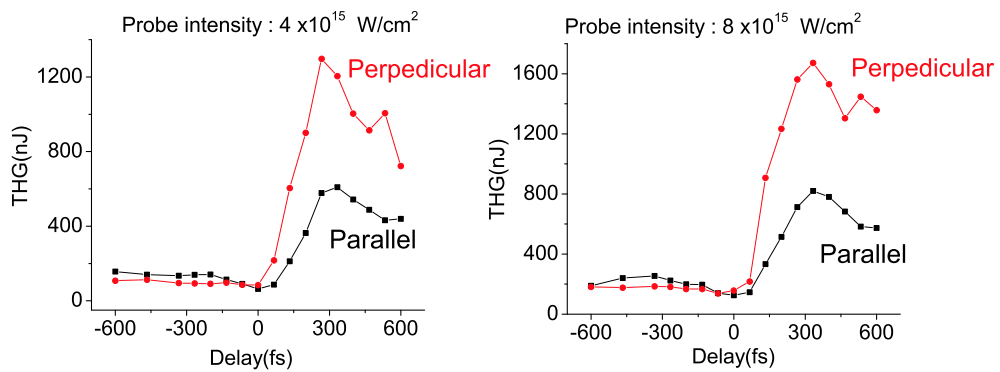


Figure 4.28: THG anisotropy in higher intensities.

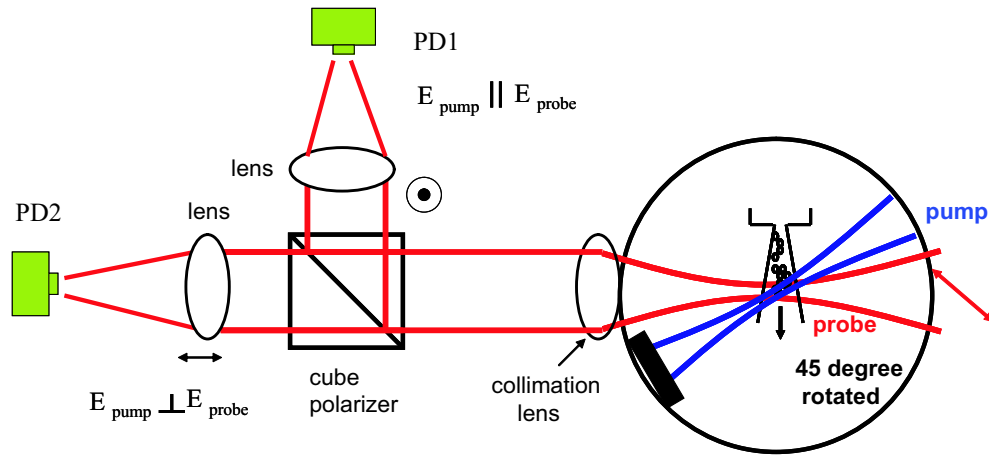


Figure 4.29: Optical Kerr effect measurement set-up.

Electrons in the cluster will experience a stronger nonlinear force because of stronger gradients along the minor axis with smaller radius (Eq. 2.25: $b \propto \omega_p^2/r_c^2$). Therefore, the perpendicularly-polarized probe will generate more THG. The ponderomotive force should also be stronger along the minor axis because of a steeper electron density gradient.

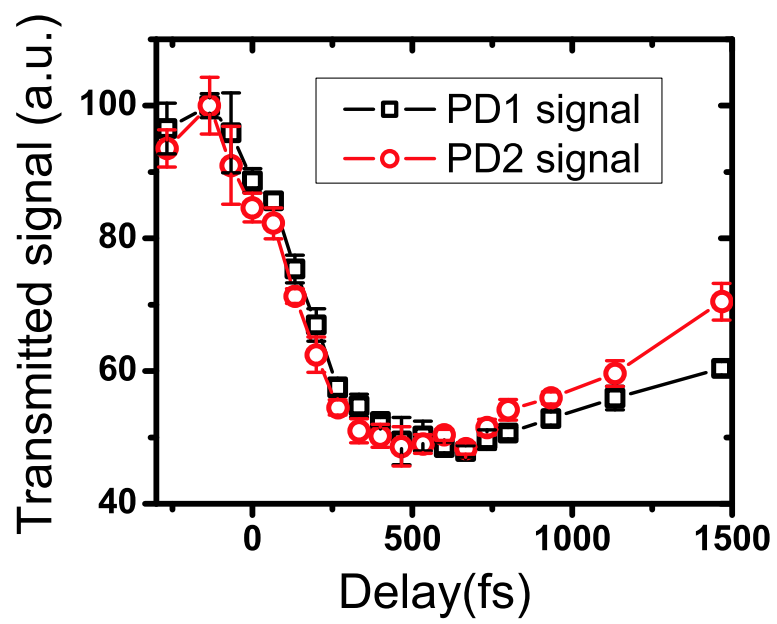


Figure 4.30: Kerr effect data.

Chapter 5

Conclusions and Future experiments

In conclusion, we studied delayed enhancement of THG from a noble gas jet containing clusters that are expanding hydrodynamically in response to ultrashort pump pulse excitation. THG polarization dependence shows the clusters expand anisotropically, while I_{probe} dependence shows little saturation up to $I_{probe} \sim 10^{16} W/cm^2$. Modeling shows transient increases of cluster $\chi^{(3)}$ and phase-match factor $J_{3\omega}(L)$ including absorption both contribute to the delayed enhancement. To enhance the phase-matching, the ratio of clusters/monomers should be higher as discussed briefly. Xe clusters (better clustering gas) or cryogenically cooled Ar clusters [41, 42] are expected to achieve this goal. Figs. 5.1 and 5.2 show that the phase-matching can be achieved with higher ratio clusters/monomers ($\geq 70\%$). I calculated assuming gas jet density $1 \times 10^{18} \text{ cm}^{-3}$. Generating 80 nm clusters is possible using the cryogenic cooling. Although the increase of absorption because of higher cluster density may inhibit the harmonic generation, phase-matching occurs before maximum absorption. Therefore, we may be able to see the perfectly phase-matched third harmonic using the time-resolved technique.

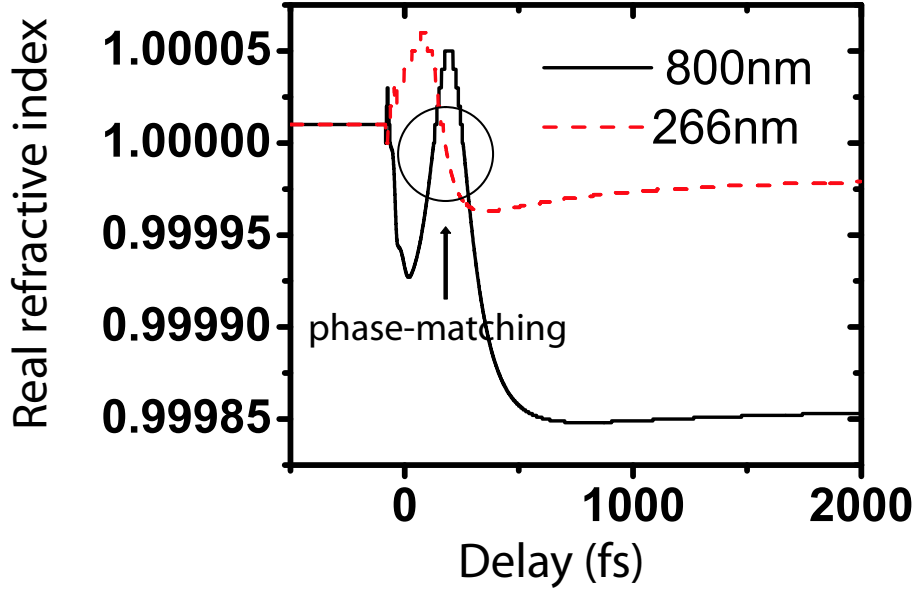


Figure 5.1: Phase matching calculation with 80 % of 20 nm radius clusters and 20 % of monomers in $1 \times 10^{18} \text{ cm}^{-3}$ density argon gas jet.

We are currently exploring scalability of these effects to higher-order harmonic generation. For $n > 3$, enhancements of $\chi^{(n)}$ and $J_{n\omega}(L)$ are expected at slightly earlier Δt , where probe absorption is weaker. Enhancement of $J_{n\omega}(L)$ is expected up to high order ($n \sim 100$) [25, 26]. As with THG, fully phase-matched high-order HG is also expected in jets with higher cluster/monomer ratio. Delayed resonant enhancement of $\chi^{(n)}$ is expected at least up to $\omega_p^{max}/\sqrt{3} = n\omega$ [29] (i.e. $n \sim 10$ for 800 nm fundamental), and possibly much higher, since resonant denominators of order $< n$ contribute to $\chi^{(n)}$. Indeed harmonics of order $n\omega \gg \omega_p$ are observed from solid targets [82].

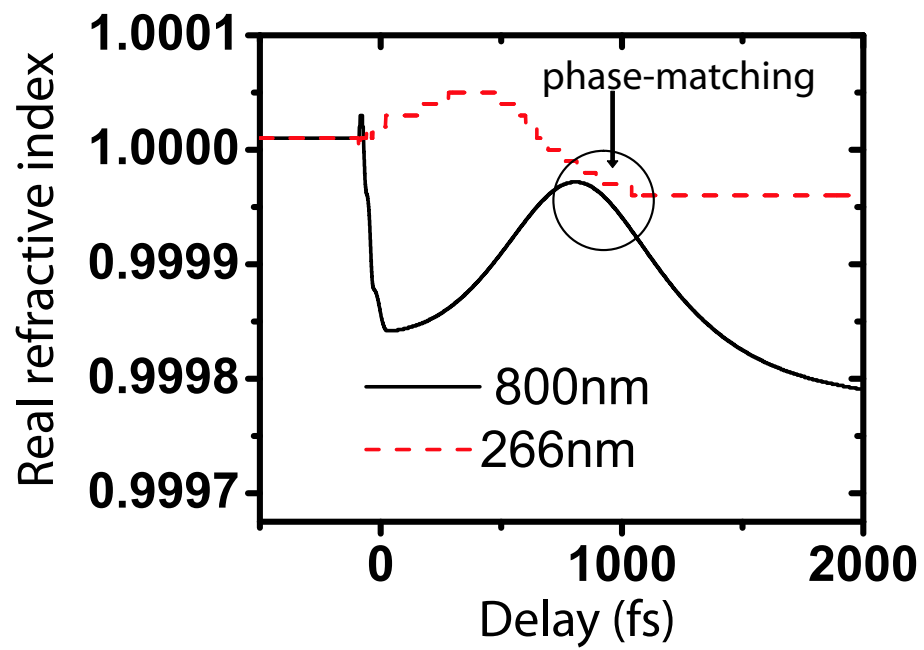


Figure 5.2: Phase matching calculation with 70 % of 80 nm radius clusters and 30 % of monomers in $1 \times 10^{18} \text{ cm}^{-3}$ density argon gas jet.

Appendix A

Theory of Kerr-lens mode locking

A.1 Introduction

Kerr-lens mode locking (KLM) occurs due to self-focusing effect that is produced by the nonlinear index change in the Kerr medium (laser crystal) or an additional loss modulation medium such as a hard aperture [49]. Especially, it was proposed that an intra-cavity aperture is necessary to achieve the intensity dependent loss modulation [83, 84]. However, several groups also showed experimentally that KLM is even possible without the intra-cavity aperture [85, 86, 87, 88, 89]. Here I present the theoretical calculation of KLM based on our homemade oscillator. In section 2, I will apply Ref. [84] to our oscillator to find a sub-resonator configuration in which KLM stably occurs. In section 3, I will present the calculated beam size in the cavity both for the continuous (CW) and KLM, using a numerical self-consistent rule (NSCR) [84, 91]. Mode-size calculation for the mode-locked beam is important to get a good quality TEM₀₀ mode and to collimate the beam after output coupler properly.

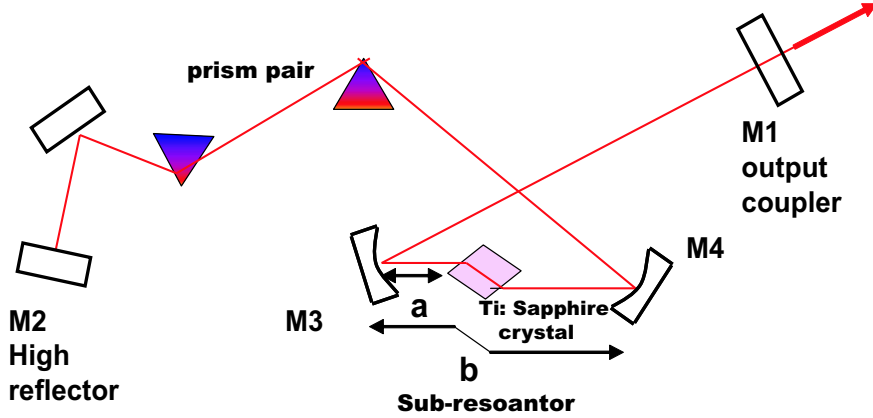


Figure A.1: Typical Kerr-lens modelocking (KLM) oscillator configuration.

A.2 KLM zone

The most important parameter for KLM is so called Kerr-lens sensitivity which is defined as the derivative of the beam size with respect to vanishing beam power [84]

$$\delta = \left(\frac{1}{2w} \frac{dw}{dp} \right)_{p \rightarrow 0}, \quad (\text{A.1})$$

where w is the spot size, p is the intracavity laser power. For KLM operation, an aperture needs to be placed at the position where δ is **negative** and **large in magnitude**. Figure A.1 shows a typical Brewster cut Ti:Sapphire laser cavity. Due to astigmatism produced by the Brewster interface, elliptical Gaussian beam propagation should be considered. According to Ref. [84], the Kerr-lens sensitivity in a tangential plane (x: parallel to an optical table) at M1 (output coupler) can be expressed,

$$\delta_{1x} = -\frac{1}{n} \left(\frac{1 - S_y^2}{1 - S_x^2} \right)^{1/4} \int_0^l \left| \frac{\overline{B}_x}{\overline{B}_y} \right|^{1/2} \frac{B_{2x} D_{2x} S_x + B_{1x} D_{1x}}{\overline{B}_x^2} d\zeta, \quad (\text{A.2})$$

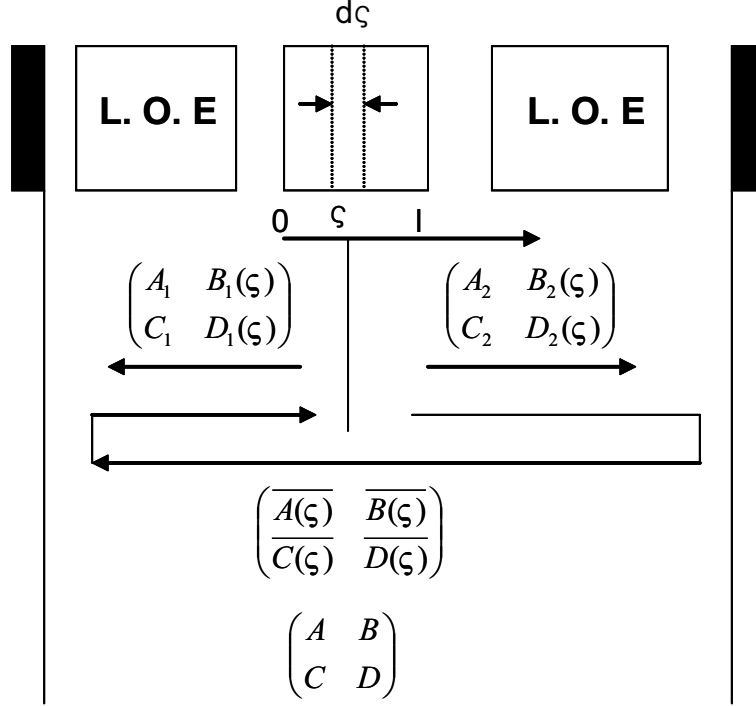
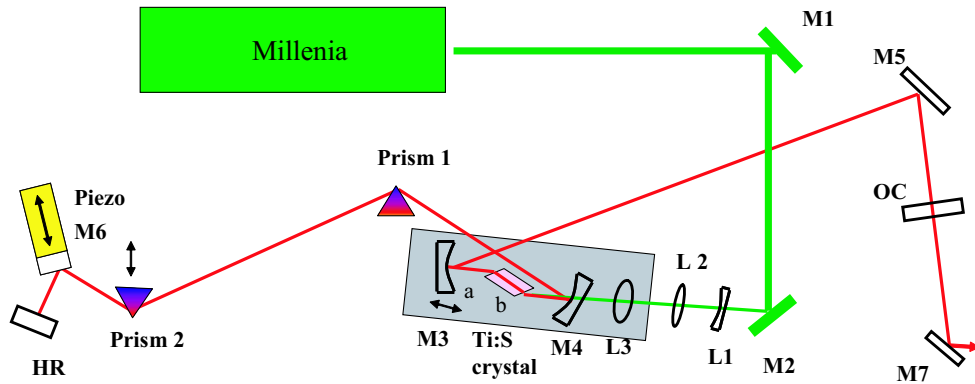


Figure A.2: KLM resonator configuration and ABCD matrices for the formula A.2

where $S_x = A_x D_x + B_x C_x$, and other matrix elements are given in Fig. A.2. Here the arrow indicates the direction to which ABCD matrices [90] are applied and L. O. E represents linear optical elements in the cavity. For the sagittal plane (y), x and y are simply exchanged.

I applied this formula to our oscillator (see Fig.A.3) to get the contour lines of the Kerr-lens sensitivity at the output coupler both for the tangential plane (Fig.A.4 (a)) and sagittal plane (Fig.A.4 (b)). As is shown in the graphs, the Kerr-lens sensitivity in the tangential plane is generally larger than the one in the sagittal plane, which means that a vertical slit to cut the beam in the horizontal direction is preferable than a horizontal slit for KLM. And the Kerr-lens sensitivity is smaller in other place than the end mirrors [83]. However, experimentally, we are not using



Rough measurement of beam path distance when mode-locked.

HR-M6 : 2.3, M6-Prism2 : 5.5, Prism1-Prism2 : 83.5, Prism-M3 : 18.4, M4-M5 : 64.3, M5-OC : 10.5 M4-the interface of the crystal (a) : 4.6, M3-the other interface : 5.2

*Note the unit is cm..

Figure A.3: Distance measurement in the our KLM cavity.

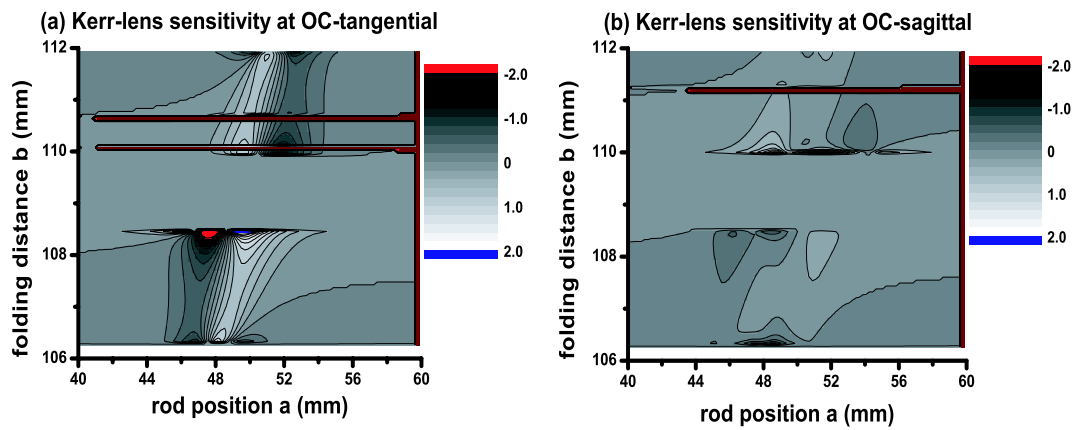


Figure A.4: Kerr-Lens Sensitivity calculation for (a) tangential plane and (b) sagittal plane.

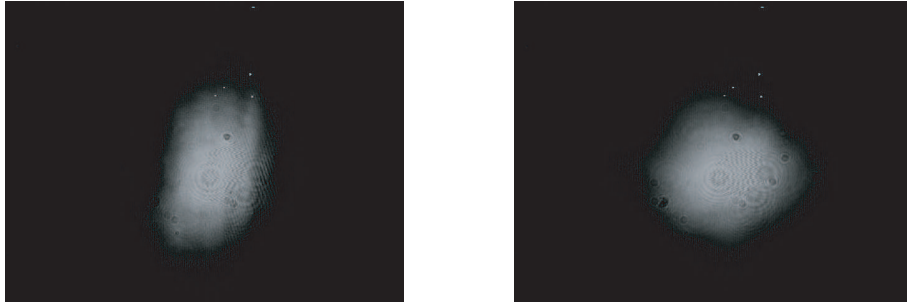


Figure A.5: (a) CW oval-shape mode (b) Modelocked round mode.

any kind of slit for KLM. We are following the method in Ref. [83]; we first align the cavity for the maximum CW power, and then we move the M3 to see an vertically oval-shaped CW mode. A slight perturbation in the prism initiates modelocking with a TEM_{00} mode [85] (see Fig. A.5). The CW mode is oval-shaped because it is the combination of TEM_{00} and TEM_{01} [88, 89]. In the cavity configuration in which the KLM is possible, there is a competition between the CW mode and mode-locked mode and by applying a small perturbation (tapping one of prims) in the cavity, the KLM mode which overlaps more efficiently with the pump, survives eventually. We realized that the prism pair plays a role of the aperture because it's generally difficult to get modelocking without clipping at the tips of prisms (It was possible for some configurations, I will discuss it in the next section) .

A.3 Beam size calculation in the oscillator cavity

Mode-size calculation is critical for finding a beam that is well compensated against astigmatism. To calculate the beam size in the cavity using NSCR, an astigmatic beam is propagated through the linear section of the cavity according to ABCD matrix relation and propagated through the Kerr-medium using a numerical solution of coupled differential equations. I reasonably guessed initial beam spot sizes in the

tangential and sagittal plane at the end mirror, and the beam was propagated back and forth until a self-consistent solution is reached [84, 91]. For the differential equations for the Kerr medium, I used the Refs. [83] and [92], in which the gain guiding effect as well as the Kerr-lens effect are included. The differential equations are expressed as

$$\frac{d\rho_{x/y}}{dz} + \rho_{x/y}^2 - \left(\frac{\lambda}{n\pi w_{x/y}}\right)^2 = -\left(\frac{\lambda}{n\pi}\right) p \frac{|\alpha_x \alpha_y|^2 \exp(2G)}{w_{x/y}^2 w_x w_y} \quad (\text{A.3})$$

$$\frac{dw_{x/y}}{dz} - \rho_{x/y} w_{x/y} = \frac{g w_{x/y}^3 w_{px} w_{py}}{2(w_{x/y}^2 + w_{px}^2) \sqrt{(w_x^2 + w_{px}^2)(w_y^2 + w_{py}^2)}} \quad (\text{A.4})$$

$$\frac{dG}{dz} = \frac{g}{2} \frac{w_{px} w_{py}}{\sqrt{(w_x^2 + w_{px}^2)(w_y^2 + w_{py}^2)}} \left(\frac{2w_x^2 + w_{px}^2}{w_x^2 + w_{px}^2} + \frac{2w_y^2 + w_{py}^2}{w_y^2 + w_{py}^2} \right) \quad (\text{A.5})$$

$$\frac{d\alpha_{x/y}}{dz} = -\left(\frac{1}{R_{x/y}} + i\frac{\lambda}{n\pi w_{x/y}^2}\right) \alpha_{x/y} = -\left(\rho_{x/y} + i\frac{\lambda}{n\pi w_{x/y}^2}\right) \alpha_{x/y} \quad (\text{A.6})$$

, with $\frac{1}{R_{x/y}} \equiv \rho_{x/y}$,

where z , x and y are the axial, sagittal, and tangential coordinates inside the Kerr-gain medium respectively, $\alpha = \alpha_x \alpha_y$ is the complex amplitude factor, w_x, w_y are spot sizes, ρ_x, ρ_y are the inverse of the radii of curvatures of the beam, w_p is the pump beam size which is assumed as a constant in the medium, g is the saturated-gain coefficient, p is the normalized power with respect to the critical power, G is the averaged gain, k is the wave number, and $\kappa = n_2 k / n$ is the Kerr coefficient.

To compare the gain effect and the Kerr-lens effect on the mode size, I first ignored the gain ($g = G = 0$) with $p = 0.55$. I put $a = 45.5$ cm, $b = 108$ cm (see Fig. A.1) and assumed $\alpha_x = \alpha_y = 1$, which is equivalent to the calculation in the Ref. [84], in which the gain was ignored. Fig. A.6 and A.7 show the radii of the continuous (CW) and modelocked (ML) beams in the cavity, considering only the

Kerr-lens effect. As shown, the astigmatism is well compensated for modelocking operation.

However, in this configuration, we have almost no clipping at the tip of the prism, which indicates no aperture is needed for KLM. There should be a Gaussian soft aperture effect by the gain guiding in the crystal, which plays a role of the loss modulation which is necessary for KLM operation. Due to the gain guiding, the curvature of the Gaussian beam does not necessarily vanish at end mirrors which are flat, and the beam size inside the cavity depends on the direction of propagation [83]. Fig. A.8, A.9 and A.10 show the beam radii in the cavity including both the Kerr-lensing and gain effects. The gain guiding effect is not so large with given parameters ($a= 45.5$ cm, $b= 108$ cm, $p= 0.55$, $w_{px} = w_{py} = 50 \mu$ m, $g = 0.015$ mm⁻¹) and the Kerr-lens effect seems to be more important, which does not fully explain the loss modulation by the Gaussian soft aperture.

A.4 Conclusion

For KLM operation, it was discussed that the self-focusing combined with the gain guiding plays an essential role. Consideration of not only these effects but also the dispersion compensation [93, 94] by two prisms is needed for a complete design of KLM oscillators.

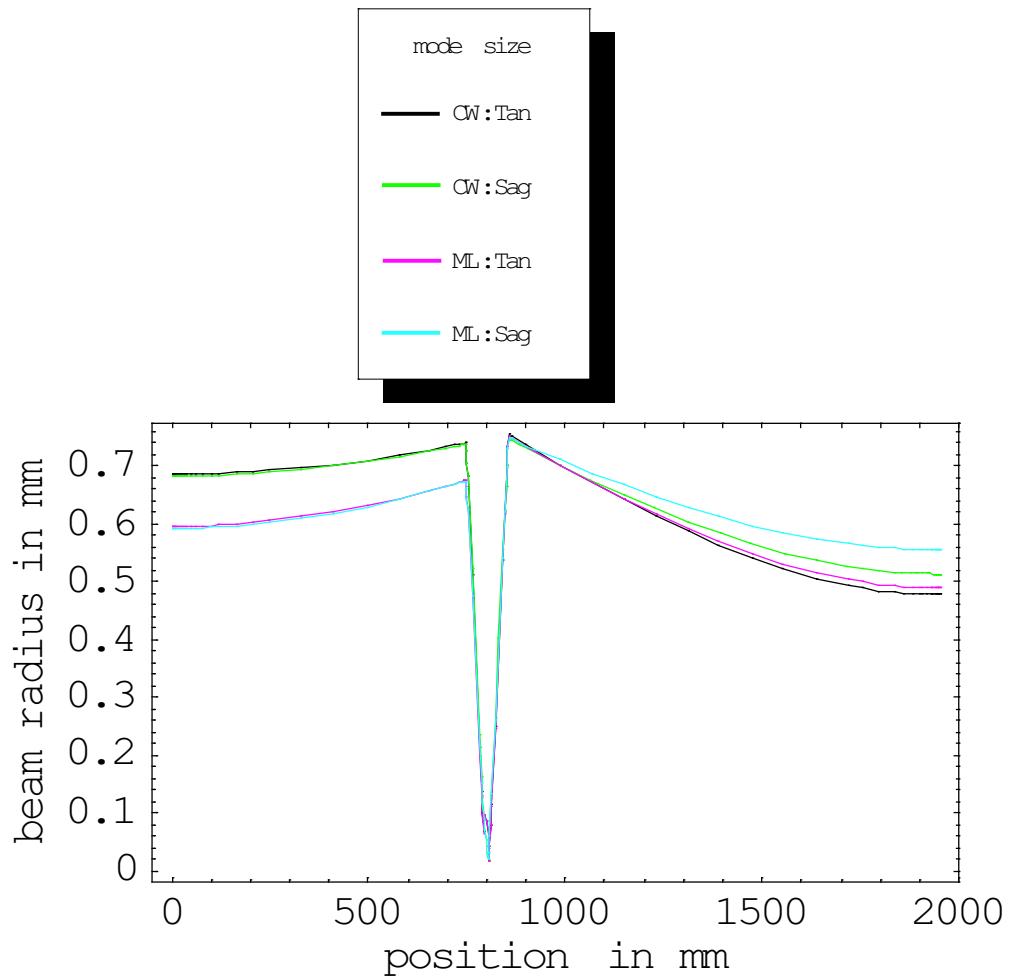


Figure A.6: Beam radii for CW and KLM without gain guiding; 0 is the outcoupler position.

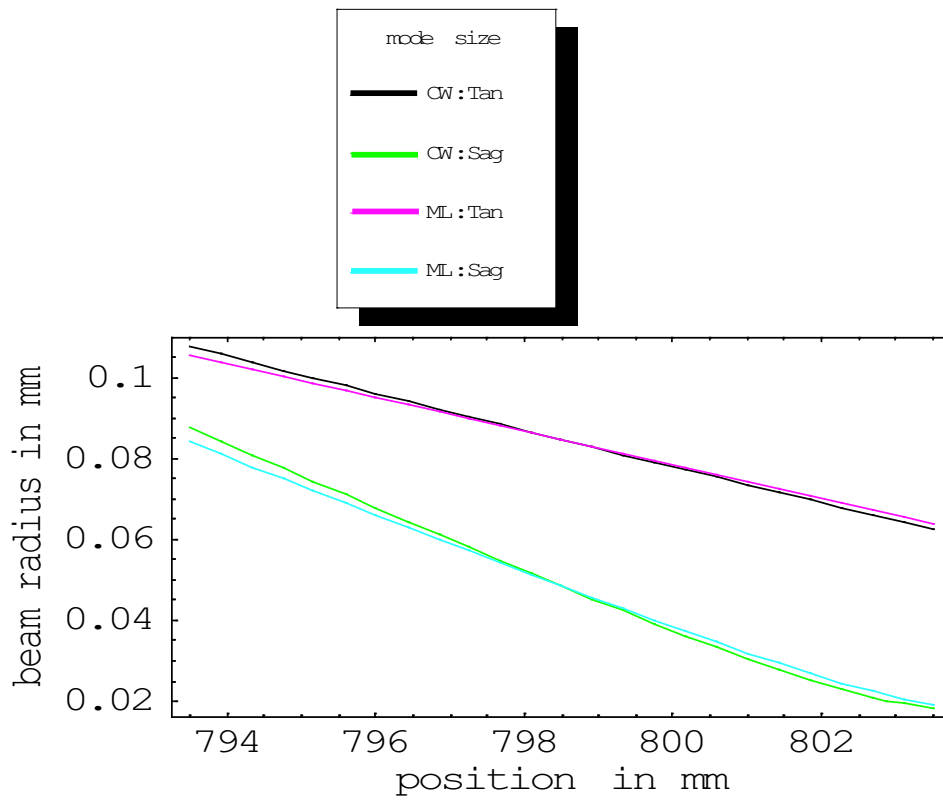


Figure A.7: Beam radii inside the Kerr medium with the same parameter as in Fig. A.6.

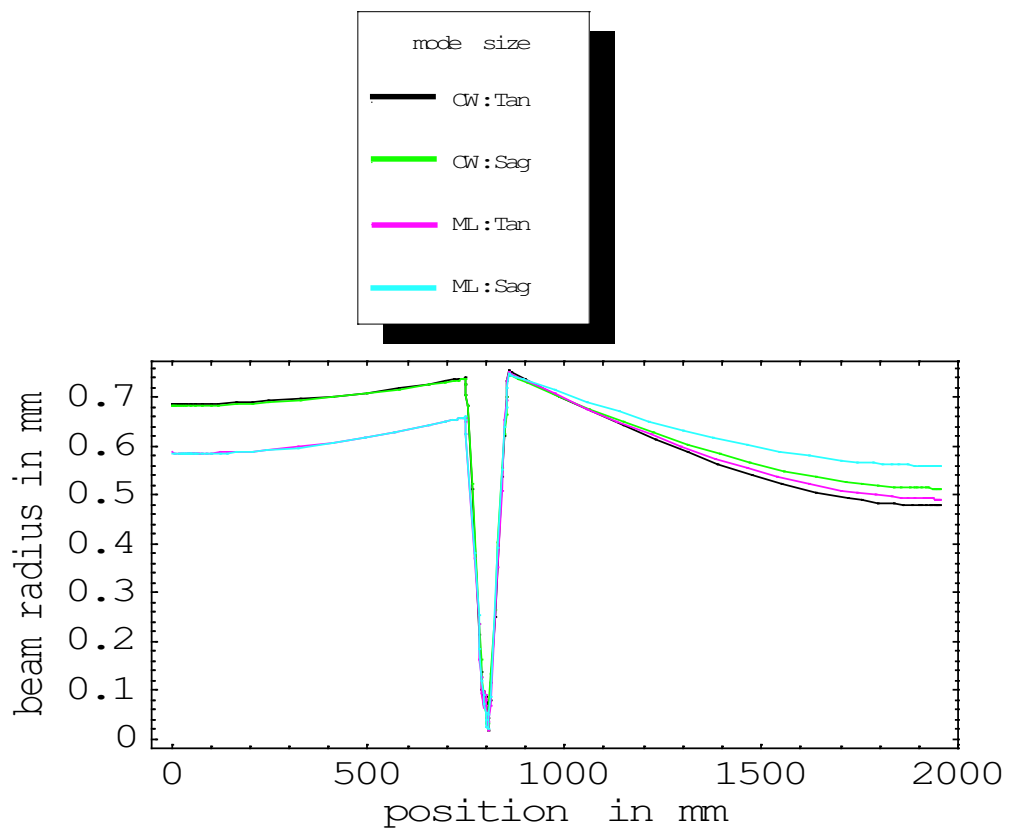


Figure A.8: Beam radii for CW and KLM with gain guiding; 0 is the output coupler position.

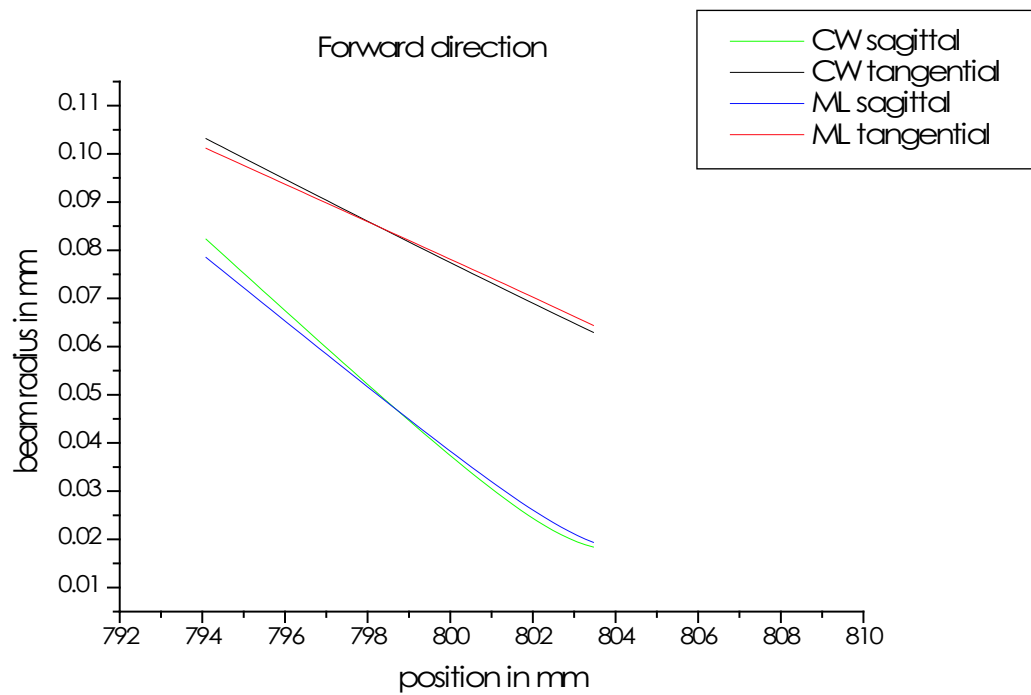


Figure A.9: Beam radii with gain in the forward direction inside the Kerr medium.

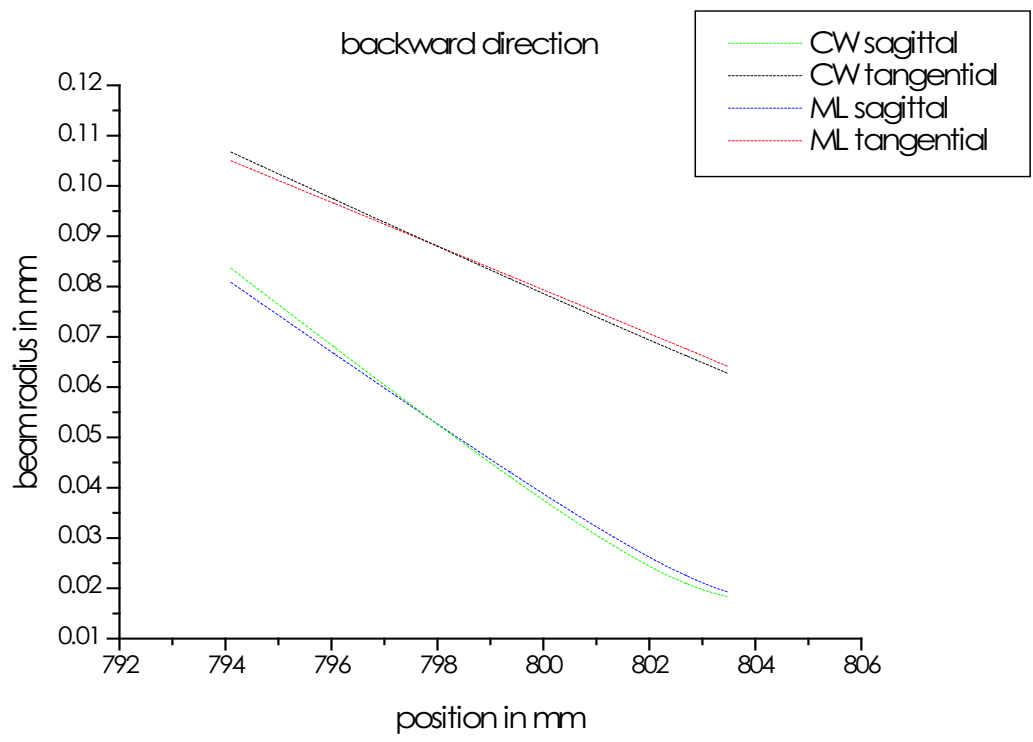


Figure A.10: Beam radii with gain in the backward direction inside the Kerr medium.

Appendix B

Atomic density and index of refraction in a clustered jet

Clusters and monomers gases both contribute to the real refractive index of a gas jet. Then, the index is

$$n_{jet} = 1 + 2\pi N_g \alpha_g + 2\pi N_c \gamma_c, \quad (\text{B.1})$$

where N_g the Ar gas density, α_g is the atomic Ar polarizability, N_c is the cluster density, and γ_c is the single cluster polarizability. The gas polarizability α_g according to the Clausius-Mossoti equation is [15]

$$\alpha_g = \frac{3}{4\pi N} \left(\frac{\varepsilon_g - 1}{\varepsilon_g + 2} \right), \quad (\text{B.2})$$

where N is the atomic density at standard temperature and pressure ($2.69 \times 10^{19} \text{ cm}^{-3}$), and ε_g is the Ar gas dielectric constant. The cluster dipole polarizability γ_c is [15]

$$\gamma_c = r_c^3 \left(\frac{\varepsilon_c - 1}{\varepsilon_c + 2} \right), \quad (\text{B.3})$$

where r_c is the cluster radius, and ε_c is the cluster dielectric constant [15, 38]

$$\varepsilon_c = \frac{8\pi N_{Ar.s}\alpha_g + 3}{3 - 4\pi N_{Ar.s}\alpha_g}, \quad (\text{B.4})$$

where $N_{Ar.s}$ is the solid Ar density ($\sim 2 \times 10^{22} \text{ cm}^{-3}$). Then, the cluster polarizability γ_c becomes

$$\gamma_c = r_c^3 \left(\frac{\frac{8\pi N_{Ar.s}\alpha_g + 3}{3 - 4\pi N_{Ar.s}\alpha_g} - 1}{\frac{8\pi N_{Ar.s}\alpha_g + 3}{3 - 4\pi N_{Ar.s}\alpha_g} + 2} \right) = r_c^3 \frac{12\pi N_{Ar.s}\alpha_g}{9} = \frac{4\pi}{3} r_c^3 N_{Ar.s}\alpha_g = N_{\#}\alpha_g, \quad (\text{B.5})$$

where $N_{\#}$ is the number of monomers in the cluster. Introducing the total atomic density (N_{total}), the residual gas density (N_g) and the cluster density (N_c) can be defined as

$$N_g = f_{gas} N_{total}, \quad (\text{B.6})$$

$$N_c = (1 - f_{gas}) N_{total} / N_{\#}, \quad (\text{B.7})$$

where f_{gas} ($0 \leq f_{gas} \leq 1$) is the gas fraction in the jet. Therefore, the refractive index is

$$\begin{aligned} n_{jet} &= 1 + 2\pi f_{gas} N_{total} \alpha_g + 2\pi \frac{(1 - f_{gas}) N_{total}}{N_{\#}} \alpha_g N_{\#}, \\ &= 1 + 2\pi N_{total} \alpha_g (1 - f_{gas} + f_{gas}) = 1 + 2\pi N_{total} \alpha_g, \end{aligned} \quad (\text{B.8})$$

Therefore, Mach-Zehnder interferometry measurement gives the (total) atomic density (gas+cluster) in the jet.

Appendix C

pump-probe experiments using a different nozzle

During preamplifier upgrade, we performed a time-resolved experiments using a nozzle with 750 μm orifice and 45° half expansion angle. We first measured probe (800 nm, 100 fs) absorption of exploding clusters ionized by 400nm pump pulses. The pump was generated by a 3 mm thick type-I KDP crystal and based on a group velocity walk-off ($\Delta t \sim L/|v_2^{-1} - v_1^{-1}|$, where $v_{1,2}$ is the group velocity for (800, 400) nm) in a thick crystal [49], we estimated the pump pulse about 210 fs. For subsonic nozzles, the modified Hagen parameter is (compare Eq. 4.1) [14]

$$\Gamma^* = k \frac{(d/\tan \alpha)^{0.85}}{T_0^{2.29}} P_0. \quad (\text{C.1})$$

Then, using the cluster size equation (Eq. 4.2), cluster radii were estimated 12, 16, 20 nm for 400, 600, 800 psi backing pressures. The peak intensity was about 1×10^{16} W/cm² for pump and 2×10^{16} W/cm² for probe. Fig. C.1 shows that larger clusters (larger backing pressure) absorbed more probe energy and reached linear Mie resonances later than smaller clusters as discussed in Chapter 2.

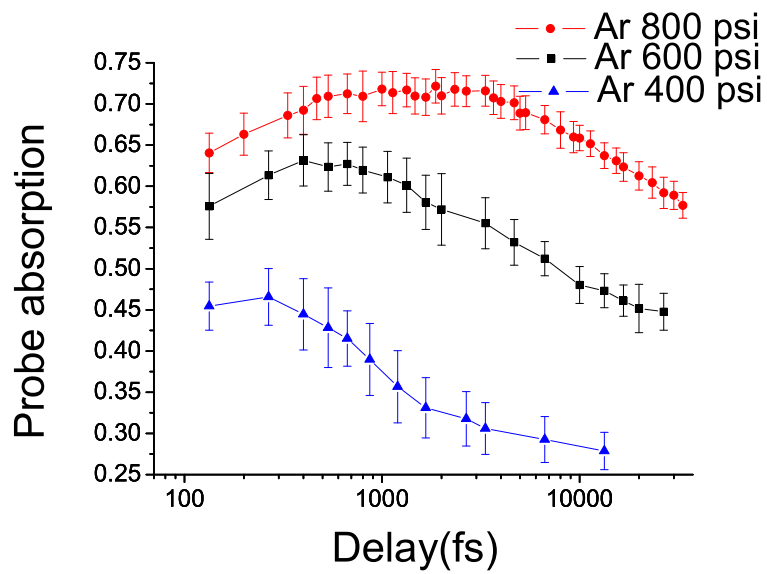


Figure C.1: Collinear pump (400nm)-probe (800nm) absorption using a subsonic nozzle. The peak intensity was about 1×10^{16} W/cm² for pump and 2×10^{16} W/cm² for probe. Cluster radii were 12, 16, 20 nm for 400, 600, 800 psi backing pressures.

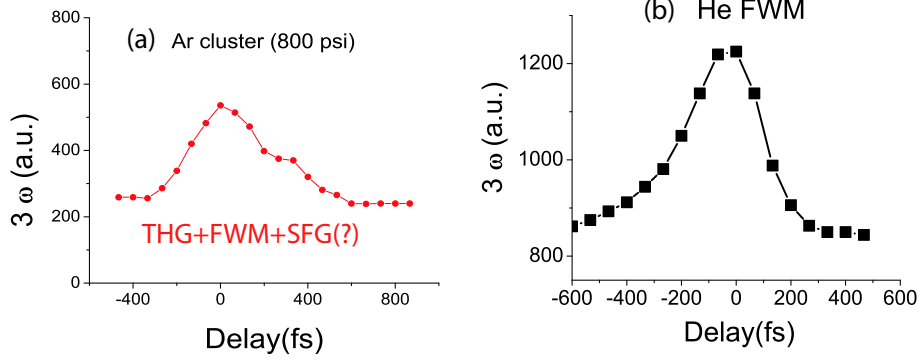


Figure C.2: Collinear pump (400nm)-probe (800nm) 3ω measurements. (a) Ar cluster (800psi) 3ω measurement shows a wide temporal peak near at $\Delta t = 0$. The peak is combination of Third Harmonic Generation (THG), Four Wave Mixing (FWM), and Sum Frequency Generation (SFG). The peak intensity was 1.5×10^{14} W/cm² for pump and 1.5×10^{13} W/cm² for probe. (b) Reference Helium (800 psi-unclustering gas) FWM signal near at $\Delta t = 0$. The peak intensity was 5×10^{13} W/cm² for 400nm and 1×10^{13} W/cm² for 800nm.

When we extended the collinear pump-probe scheme to a third-harmonic experiment, there was a temporally wide peak near at $\Delta t = 0$ (Fig. C.2(a)). The peak is composed of three signals: (1) probe-generated THG signal $E_{THG}^{3\omega} \propto \chi^{(3)}(E_{probe}^\omega)^3$ at all Δt , (2) Four Wave Mixing (FWM) signal $E_{FWM}^{3\omega} \propto \chi^{(3)}(E_{probe}^\omega)^*(E_{pump}^{2\omega})^2$ at $\Delta t \sim 0$, (3) Possible Sum Frequency Generation (SFG) $E_{SFG}^{3\omega} \propto \chi^{(2)}(E_{probe}^\omega)(E_{pump}^{2\omega})$ at $\Delta t \sim 0$ because of ionization induced symmetry breaking in centrosymmetric clusters. We used a helium gas (unclustering gas) as a reference for FWM as well as finding a zero delay. Fig. C.2(b) confirms that there was contribution from the FWM of Ar clusters. Therefore, we could not verify that there was a nonlinear Mie resonance from exploding Ar clusters and/or phase matching from a clustered jet. It was also unclear about SFG contribution from Ar clusters.

To separate three signals spatially, we used a noncollinear pump-probe geometry at a small angle ($\sim 1.7^\circ$), so that THG, FWM and SFG signals propagated in different directions by momentum conservation (Fig C.3). Most of the FWM signal

was blocked not to be incident on a detector grating.

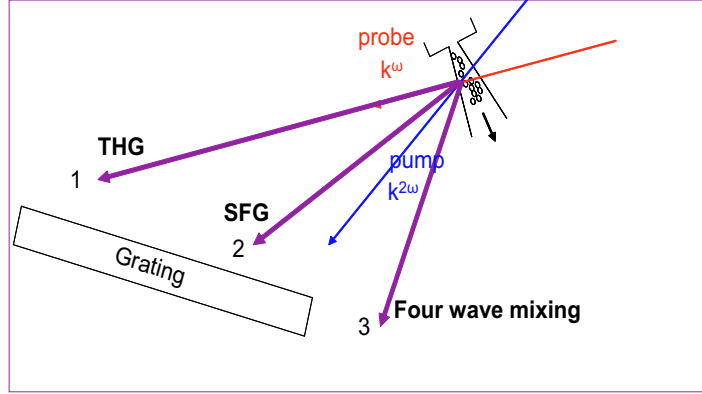


Figure C.3: Noncollinear pump (400nm)-probe (800nm) geometry to separate FWM, SFG, and THG signals spatially using momentum conservation.

Fig. C.4 shows results of pump intensity scan of the probe-generated THG from Ar clusters (800psi). Surprisingly, there were two peaks near at $\Delta t=0$ and $\Delta t=250$ fs when pump intensity was lower than Ar optical ionization threshold ($\sim 1 \times 10^{14}$ W/cm²) (Figs. C.4(a) and (b)). We think that the zero delay peak is from SFG and the second peak at $\Delta t=250$ fs is from the nonlinear Mie resonance and/or phase matching enhancement. However, we cannot completely rule out the possibility of the FWM signal leak at $\Delta t \sim 0$ from Ar clusters. When we increased the pump intensity further, the peak at $\Delta t = 250$ fs disappeared and the zero delay peak became wider (Figs. C.4(c), (d) and (e)), suggesting that two peaks combined. We attribute this effect to faster cluster expansion, therefore the earlier 3ω resonance because of heating by higher pump intensity and/or phase matching change because of optical ionization of Ar monomers.

However there was a reproducibility problem in this experiment. Two peaks were temporally separated only with pump intensity that can hardly ionize Ar monomer gases. By contrast, we expect that Ar clusters possibly ionized by the multiphoton process [72] were ionized more due to local solid density and started

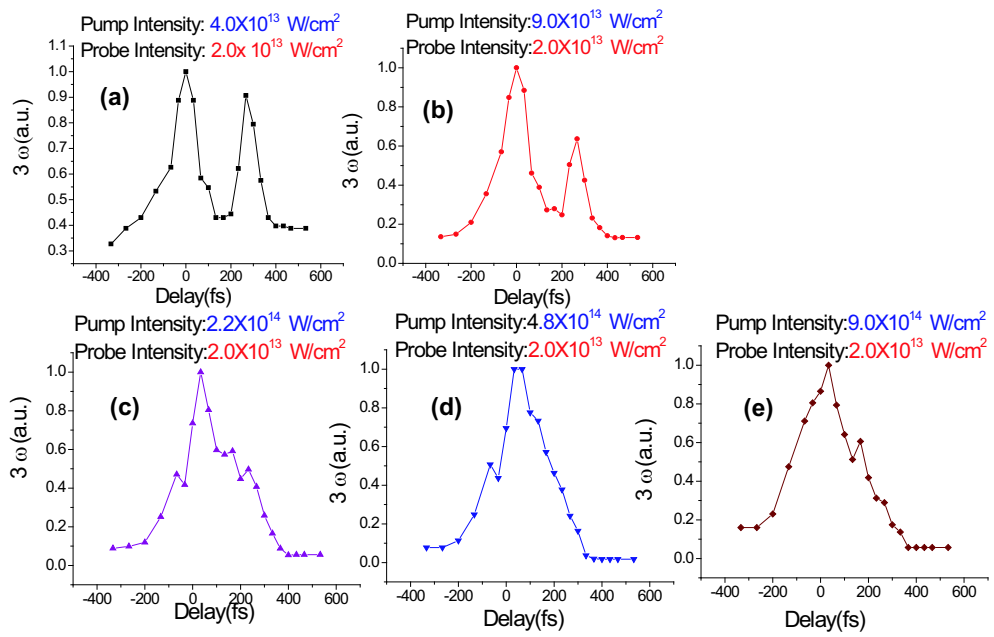


Figure C.4: Noncollinear THG pump intensity scan results using Ar clusters (800 psi).

to expand extremely slowly. Then, they could reach the nonlinear Mie resonance and/or temporal phase matching. As discussed in Chapters 2 and 4, phase matching condition is worse when dominant monomers in a gas jet are ionized and form plasma. Therefore, by weakly ionizing clusters without or negligible monomer ionization, we can expect the temporal THG enhancement because of cluster expansion dynamics. Based on difficulty in reproducing the results and their variation depending on alignment, we think that phase matching was strongly involved. However we don't have a good model of laser-cluster interaction in this pump range.

Appendix D

Two-beam second-harmonic generation from a clustered gas jet

Figliozzi *et al.* [95] demonstrated enhanced Second Harmonic Generation (SHG) from centrosymmetric Si nanocrystals using two noncollinear, orthogonally polarized fundamental beams. The enhancement is because of a nonlocal dipole term which is proportional to $(\vec{E} \cdot \nabla)\vec{E}$. This two-beam method was successfully applied to generate enhanced quadrupolar SHG from isotropic glass samples [96]. We performed the two-beam SHG experiment in a clustered gas jet. As a preliminary check, we first reproduced experimental results by Sun *et al.* [96] using glass samples. Two orthogonally polarized 800 nm pulses with an intersection angle $\sim 25^\circ$ were overlapped at approximately 3 cm away from each focus to increase an interaction volume and to prevent damage of glass samples (Fig. D.1). The peak intensity was 5×10^{11} W/cm² for each beam and a two-beam interaction length was about 1.5 mm. We put a PMT with a 400nm bandpass filter to detect SHG. Fig. D.2 shows lateral position scan of two-beam SHG using a 0.9 mm Corning glass sample

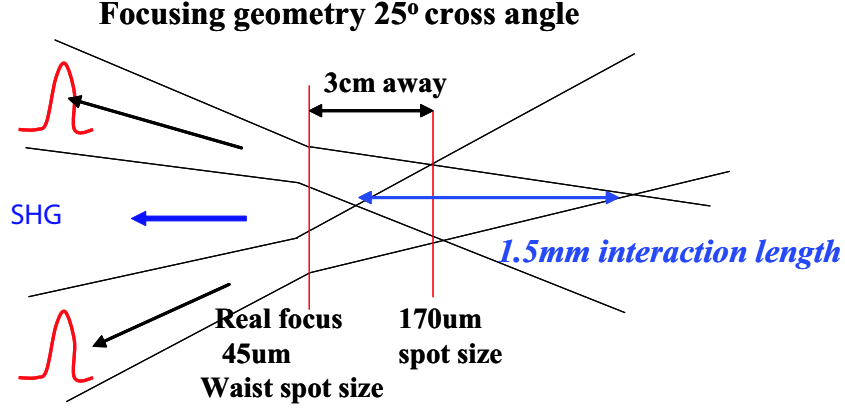


Figure D.1: Two-beam SHG experimental set-up using glass samples. Both fundamental beam (800 nm, 100 fs) intensity was 5×10^{11} W/cm².

((a)) and a 3 mm unknown glass sample ((b)). In case of the 0.9 mm sample, the SH signal was maximum when the two-beam overlap (1.5 mm length) is near the center of the sample. By contrast, two local maxima existed for the thicker sample (3 mm) when the overlap is near at the front surface and the back surface. It is because of phase matching difference and the result matched well with the result of Sun *et.al* [96] for a tight focusing case. We believe that SHG from the back surface was stronger than from the front surface because of SHG absorption in the glass sample.

SHG from individual spherical particles scales approximately as r_c^6 [97], therefore SHG intensity from a sample scales as $N_c^2 r_c^6 I_\omega^2$, where N_c is the cluster density, r_c is the cluster radius and I_ω is the fundamental beam intensity. Then, using relation $N_c \sim 1/r_c^3$, SHG should approximately scale as $n_{atom}^2 I_\omega^2$, where n_{atom} is the average atomic density of the sample. To compensate for 3 orders of magnitude difference in density between the glass sample ($\sim 10^{22}$ cm⁻³) and the clustered jet ($< 10^{19}$ cm⁻³ see Fig. 4.8) and detect observable numbers of SH photons (≥ 10 photons/pulse) from a clustered gas jet, we should increase the laser intensity

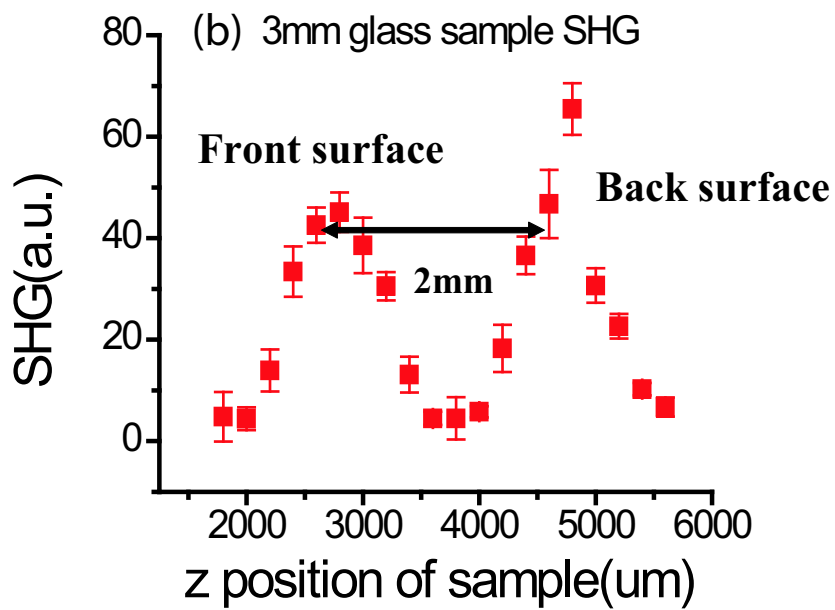
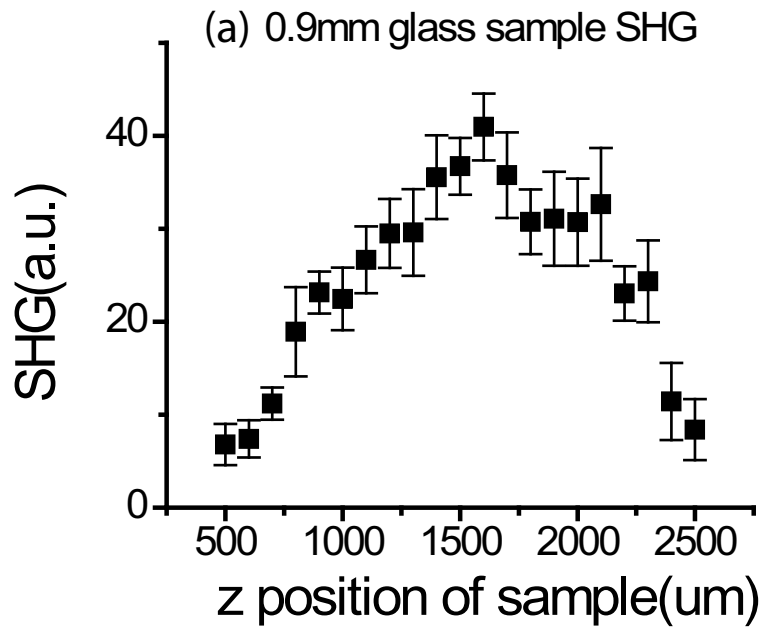


Figure D.2: Position scan of two-beam SHG using glass samples. (a) 0.9 mm corning glass sample. (b) 3 mm unknown glass sample.

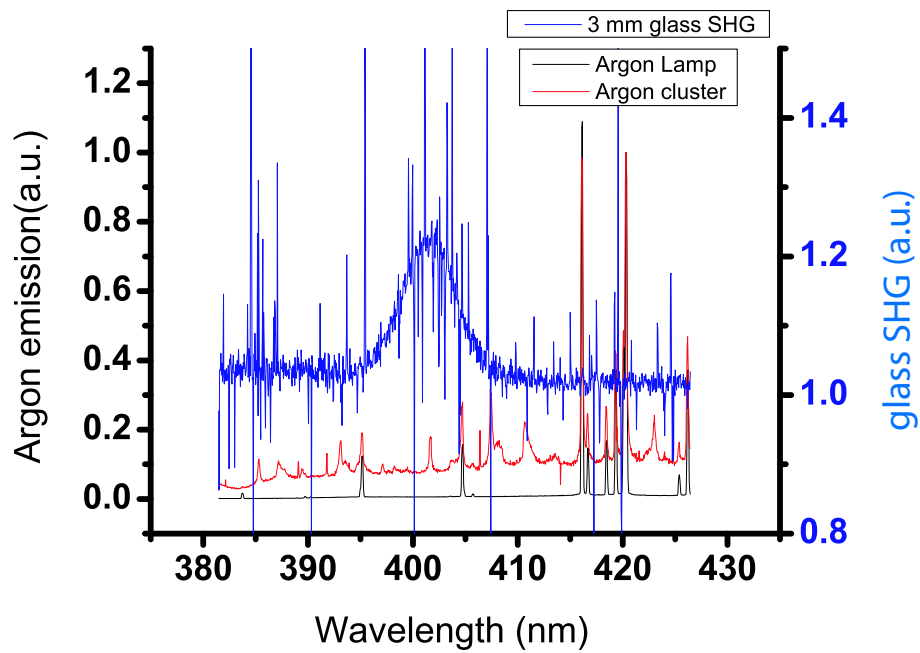


Figure D.3: Two-beam SHG spectrum from a glass sample (blue curve) and 24 nm radius argon clusters (red curve). Ar lamp emission lines (black curve) compares fluorescence from Ar clusters. Both fundamental beam (800 nm, 100 fs) intensity was $3 \times 10^{13} \text{ W/cm}^2$. For SHG from the glass sample, we used the fundamental intensity at $5 \times 10^{11} \text{ W/cm}^2$

by 3 orders of magnitude. However, we could not achieve that intensity ($>1 \times 10^{14} \text{ W/cm}^2$) because we increased the interaction volume by using enlarged beams ($I_{max} \sim 3 \times 10^{13} \text{ W/cm}^2$). Therefore, we integrated signals for more than 100 shots using a spectrometer and a nitrogen-cooled CCD camera. As shown in Fig. D.3, compared with SHG from the glass sample, there was no observable SHG from clusters and fluorescence light always dominated. We opened an input slit of the spectrometer more than 2 mm to collect weak SHG signals from the glass sample, therefore wavelength resolution of the spectrometer became poor and a possible fringe pattern in SHG due to phase matching was not clearly visible [95]. Although we even ionized clusters using a pump pulse ($I_{pump} \leq 1 \times 10^{14} \text{ W/cm}^2$), then a time-resolved two-beam method was used to achieve nonlinear Mie resonances from expanding clusters, we could not see any SH signal because the strong fluorescence and recombination light dominated from a clustered plasma. The density of the jet medium was too low to see the enhanced SHG.

Bibliography

- [1] A. LHuillier and P. Balcou, Phys. Rev. Lett. **70**, 774, 1993.
- [2] J. J. Macklin, J. D. Kmetec, and C. L. Gordon III , Phys. Rev. Lett. **70**, 766, 1993.
- [3] T. Ditmire, J. K. Crane, H. Nguyen, L. B. DaSilva, and M. D. Perry, Phys. Rev. A **51**, 902, 1995.
- [4] R. L. Carman, C. K. Rhodes, and R. F. Benjamin, Phys. Rev. A **24**, 2649, 1981.
- [5] B. Bezzerides, R. D. Jones, and D. W. Forslund, Phys. Rev. Lett. **49**, 202, 1982.
- [6] T. D. Donnelly, T. Ditmire, K. Neuman, M. D. Perry, and R. W. Falcone, Phys. Rev. Lett. **76**, 2472, 1996.
- [7] Zenghu Chang, Andy Rundquist, Haiwen Wang, Margaret M. Murnane, and Henry C. Kapteyn, Phys. Rev. Lett. **79**, 2967, 1997.
- [8] M. Schnrer, Ch. Spielmann, P. Wobrauschek, C. Streli, N. H. Burnett, C. Kan, K. Ferencz, R. Koppitsch, Z. Cheng, T. Brabec, and F. Krausz, Phys. Rev. Lett. **80**, 3236, 1998.
- [9] P. Agostini and L. F. DiMauro, Rep. Prog. Phys. **67**, 813, 2004.
- [10] J. L. Krause, K. J. Schafer, and K. C. Kulander, , Phys. Rev. Lett. **68**, 3535, 1992.

- [11] P. B. Corkum, Phys. Rev. Lett. **71**, 1994, 1993.
- [12] W. L. Kruer, *The physics of laser plasm interactions*, (Addison-Wesley, Redwood City, 1988).
- [13] O. F. Hagen, Rev. Sci. Instrum. **63**, 2374, 1992.
- [14] T. Ditmire, T. Donnelly, A. M. Rubenchik, R. W. Falcone, and M. D. Perry, Phys. Rev. A **53**, 3379, 1996.
- [15] J. D. Jackson, *Classical Electrodynamics*, (Wiley, New York, 1975).
- [16] J. Zweiback, T. Ditmire, and M. D. Perry, Phys. Rev. A **59**, 3166, 1999.
- [17] J. Zweiback, T. Ditmire, and M. D. Perry, Opt. Express **6**, 236, 2000.
- [18] T. Ditmire, J. W. G. Tisch, E. Springate, M. B. Mason, N. Hay, R. A. Smith, J. P. Marangos and M. H. R. Hutchinson, Nature **386**, 54, 1997.
- [19] Y. L. Shao, T. Ditmire, J. W. G. Tisch, E. Springate, J. P. Marangos, and M. H. R. Hutchinson, Phys. Rev. Lett. **77**, 3343, 1996.
- [20] H. M. Milchberg, S. J. McNaught, and E. Parra, Phys. Rev. E **64**, 56402, 2001.
- [21] K.Y. Kim, I. Alexeev, E. Parra, and H.M. Milchberg, Phys. Rev. Lett. **90**, 23401, 2003.
- [22] I. Alexeev, T.M. Antonsen, K.Y. Kim, and H.M. Milchberg, Phys. Rev. Lett. **90**, 103402, 2003.
- [23] Ayush Gupta, T. M. Antonsen Jr., and H. M. Milchberg, Phys. Rev. E. **70**, 046410, 2004.
- [24] K. Y. Kim, I. Alexeev, T. M. Antonsen, A. Gupta, V. Kumarappan, and H. M. Milchberg, Phys. Rev. A. **71**, 011201, 2005.

- [25] T. Tajima, Y Kishimoto, and M. C. Downer, *Phys. Plasmas*. **6**, 3759, 1999.
- [26] John W. G. Tisch, *Phys. Rev. A*. **62**, 41802, 2000.
- [27] Mykhailo V. Fomyts'kyi, Boris N. Breizman, Alexey V. Arefiev, and Charles Chiu , *Phys. Plasmas*. **11**, 3349, 2004.
- [28] S. Fomichev, S. Popruzhenko, D. Zaretsky, and W. Becker , *Opt. Express*. **11**, 2433, 2003.
- [29] Boris N. Breizman, Alexey V. Arefiev, and Mykhailo V. Fomyts'kyi, *Phys. Plasmas*. **12**, 056706, 2005.
- [30] W. H. Press, S. A. Teukolsky, W. T. Vettering, and B. P. Flannery, *Numerical Recipes in C*, (Cambridge University Press, New York, 1992).
- [31] F. Dorchies, F. Blasco, T. Caillaud, J. Stevefelt, C. Stenz, A. S. Boldarev, and V. A. Gasilov, *Phys. Rev. A*. **68**, 023201 (2003).
- [32] T. Ditmire, E. Springate, J. W. G. Tisch, Y. L. Shao, M. B. Mason, N. Hay, J. P. Marangos, and M. H. R. Hutchinson, *Phys. Rev. A* **57**, 369, 1998.
- [33] M. V. Ammosov, N. B. Delone, and V. P. Krainov, *Sov. Phys. JETP* **64**, 1191, 1986.
- [34] W. Lotz, *Z. Phys.* **216**, 241, 1968.
- [35] V. P. Silin, *Sov. Phys. JETP* **20**, 1510, 1965.
- [36] F. F. Chen, *Plasma Physics and Controlled Fusion*, (Plenum, New York, 1984).
- [37] Jiangsheng Liu, Ruxin Li, Pinpin Zhu, Zhizhan Xu, and Jingru Liu, *Phys. Rev. A* **64**, 33426, 2001.
- [38] R. Boyd, *Nonlinear Optics*, (Academic Press, San Diego, 1992).

- [39] E. Dawes, Phys. Rev. **169**, 47, 1968.
- [40] W. P. Leemans, C. E. Clayton, W. B. Mori, K. A. Marsh P. K. Kaw, A. Dyson, C. Joshi, and J. M. Wallace, Phys. Rev. A. **46**, 1091, 1992.
- [41] R. A. Smith, T. Ditmire, and J. W. G. Tisch, Rev. Sci. Instrum. **69**, 3798, 1998.
- [42] E. Parra, S. J. McNaught, and H. M. Milchberg, Rev. Sci. Instrum. **73**, 468, 2002.
- [43] D. Strickland, and G. Mourou, Opt. Commun. **56**, 219, 1985.
- [44] P. Maine, D. Strickland, P. Bado, M. Pessot, and G. Mourou, IEEE J. Quantum Electron. **24**, 398, 1988.
- [45] M. Pessot, D. Strickland, and G. Mourou, Opt. Commun. **62**, 419, 1987.
- [46] M. Pessot, J. Squier, P. Bado, G. Mourou and D. J. Harter, IEEE J. Quantum Electron. **25**, 61, 1988.
- [47] S. Backus, C. G. Durfee III, M. M. Murnane, and H. C. Kapteyn, Rev. Sci. Instrum. **69**, 1207, 1998.
- [48] E.W. Gaul, *Fully Ionized Helium Waveguides for Laser Wakefiled Acceleration: Ph. D Dissertation*, (University of Texas at Austin, 2000).
- [49] J. C. Diels, and W. Rudolph, *Ultrafast Laser Pulse Phenomena*, (Academic Press, San Diego, 1996).
- [50] R. L. Fork, O. E. Martinez, and J. P. Gordon, Opt. Lett. **9**, 150, 1984.
- [51] O. E. Martinez, J. P. Gordon, and R. L. Fork, J. Opt. Soc. Am. B **1**, 1003, 1984.

- [52] B. E. Lemoff, and C. P. J. Barty, *Opt. Lett.* **18**, 1651, 1993.
- [53] E. Hecht, *Optics*, (Addison Wesley, San Francisco, 2002).
- [54] L. M. Franz, and J. S. Nodvik, *J. Appl. Phys.* **34**, 2346, 1963.
- [55] W. H. Lowdermilk, and J. E. Murray, *J. Appl. Phys.* **51**, 2436, 1980.
- [56] W. Koechner, *Solid-state Laser Engineering*, (Springer, Berlin, 1999).
- [57] R. Weber, B. Neuenschwander, and H. P. Weber, *Optical Materials* **11**, 245, 1999.
- [58] H. Kogelnik, *Bell Syst. Tech. J.* **44**, 455, 1965.
- [59] J. Wörmer, V. Guzielski, J. Stapelfeldt and T. möller, *Chem. Phys. Lett.* **159**, 321, 1989.
- [60] H. P. Birkhofer, H. Haberland, M. Winterer, and D. R. Worsnop, *Ber. Bunsenges. Phys. Chem.* **88**, 207, 1984.
- [61] J. W. Keto, Hong Cai, Martin Kykta, Chen Lei, Thomas möller, and Georg Zimmerer, *J. Chem. Phys.* **107**, 6080, 1997.
- [62] V. Malka, C. Coulaud, J. P. Geindre, V. Lopez, Z. Najmudin, D. Neely, and F. Amiranoff, *Rev. Sci. Instrum.* **71**, 2329, 2000.
- [63] V. Malka, C. Coulaud, J. P. Geindre, V. Lopez, Z. Najmudin, D. Neely, and F. Amiranoff, *Rev. Sci. Instrum.* **71**, 2329, 2000.
- [64] Kjell Bockasten, *J. Opt. Soc. Am.* **51**, 943, 1961.
- [65] R. Illingworth, and R. K. Thareja, *J. Phys. E: Sci. Instrum.* **14**, 147, 1981.
- [66] K. Y. Kim, V. Kumarappan, and H. M. Milchberg, *Appl. Phys. Lett.* **83**, 3210, 2003.

- [67] R. Karnbach, M. Joppien, J. Stapelfeldt, J. Wörmer and T. möller, *Rev. Sci. Instrum.* **64**, 2838, 1993.
- [68] J. W. Keto, *personal communication*, 2005.
- [69] H.-H. Chu, H.-E. Tsai, Y.-F. Xiao, C.-H. Lee, J.-Y. Lin, J. Wang, and S.-Y. Chen, *Phys. Rev. E.* **69**, 035403, 2004.
- [70] C. W. Siders, N. C. Turner III, M. C. Downer, A. Babine, A. Stepanov, and A. Sergeev, *J. Opt. Soc. Am. B.* **13**, 330, 1996.
- [71] E. Springate *et al.*, *Phys. Rev. A.* **61**, 044101 (2000).
- [72] Y. R. Shen, *The Principles of Nonlinear Optics*, (Wiley, New York, 1984).
- [73] F. Brunel, *J. Opt. Soc. Am. B.* **7**, 521, 1990.
- [74] N. E. Andreev, M. E. Veisman, and M. V. Chegotov, *Sov. Phys. JETP* **97**, 554, 2003.
- [75] T. Taguchi, T. M. Antonsen, and H. M. Milchberg, *Phys. Rev. Lett.* **92**, 205003, 2004.
- [76] A. L'Huillier, L. A. Lompre, G. Mainfray, and C. Manus, in *Atoms in Intense Laser Fields* edited by Mihai Gavrila, (Academic Press, Boston, 1992).
- [77] X. Lie, D. Umstadter, E. Esarey, and A. Ting, *IEEE Trans. Plas. Sci.* **21**, 90, 1993.
- [78] V. Kumarappan, M. Krishnamurthy, and D. Mathur, *Phys. Rev. Lett.* **87**, 085005, 2001.
- [79] K. Ishikawa, and T. Blenski, *Phys. Rev. A.* **62**, 063204, 2000.
- [80] F. Brunel, *Phys. Rev. Lett.* **59**, 52, 1987.

- [81] M. K. Grimes *et al.*, Phys. Rev. Lett. **80**, 4010, 1999.
- [82] B. Dromey, M. Zepf, A. Gopal, K. Lancaster, M. S. Wei, K. Krushelnick, M. Tataraki, N. Vakakis, S. Moustazis, R. Kodama, M. Tampo, C. Stoeckl, R. Clarke, H. Habara, D. Neely, S. Karsch and P. Norreys, Nature physics, **2**, 456, 2006.
- [83] J. Herrmann, J. Opt. Soc. Am. B **11**, 498, 1994.
- [84] V. Magni, G. Cerullo, S. De Silvestri, and A. Monguzzi, J. Opt. Soc. Am. B **12**, 476, 1995.
- [85] M. T. Asaki, C. Huang, D. Garvey, J. Zhou, H. C. Kapteyn, and M. M. Murnane, Opt. Lett. **18**, 977, 1993.
- [86] C. Huang, M. T. Asaki, S. Backus, M. M. Murnane, and H. C. Kapteyn, Opt. Lett. **17**, 1289, 1992.
- [87] J. Zhou, G. Taft, C. Huang, D. Garvey, M. M. Murnane, and H. C. Kapteyn, Opt. Lett. **19**, 1149, 1994.
- [88] M. Lai, Opt. Lett. **19**, 722, 1994.
- [89] D. G. Juang, Y. C. Chen, S. H. Hsu, K. H. Lin, and W. F. Hsieh, J. Opt. Soc. Am. B **14**, 2116, 1997.
- [90] A. E. Siegman, *Lasers*, (University Science Books, California, 1986).
- [91] R. E. Bridges, R. W. Boyd, and G. P. Agrawal, Opt. Lett. **18**, 2026, 1993.
- [92] S. Gatz, and J. Herrmann, Opt. Lett. **20**, 825, 1995.
- [93] K. H. Lin, and W. F. Hsieh, J. Opt. Soc. Am. B **13**, 1786, 1996.
- [94] C. Spielmann, P. F. Curley, T. Brabec, and F. Krausz, IEEE J. of Quantum Electron **30**, 1100, 1994.

- [95] P. Figliozzi, L. Sun, Y. Jiang, N. Matlis, B. Mattern, M. C. Downer, S. P. Withrow, C.W. White, W. L. Mochan, and B. S. Mendoza, Phys. Rev. Lett. **94**, 047401, 2005.
- [96] L. Sun, P. Figliozzi, Y. Q. An, M. C. Downer, W. L. Mochan, and B. S. Mendoza, Opt. Lett. **30**, 2287, 2005.
- [97] J. I. Dadap, J. Shan, K. B. Eisenthal, and T. F. Heinz, Phys. Rev. Lett. **83**, 4045, 1999.

Vita

Bonggu Shim was born in Anyang city, South Korea, on July 11, 1971, the son of jonggak Shim and Soja Kim. He received the Bachelor of Science degree in Physics from Seoul National University with Honors (Cum Laude) in 1997. Except mandatory military service between 1992 and 1993, he was actively involved in sports, music activities as well as studying physics and math. In 1997, he entered the University of Texas at Austin to attend the graduate school in Physics. Later, joining the Femtosecond Spectroscopy Laboratory, he has studied the experimental, computational laser-plasma interaction and participated in building a terawatt laser system under supervision of Dr. Michael C. Downer. He got married to Youjung Lee in 2005.

Permanent Address: 1636 West 6th Street C
Austin, Texas, 78703

This dissertation was typeset with $\text{\LaTeX} 2_{\epsilon}$ ¹ by the author.

¹ $\text{\LaTeX} 2_{\epsilon}$ is an extension of \LaTeX . \LaTeX is a collection of macros for \TeX . \TeX is a trademark of the American Mathematical Society. The macros used in formatting this dissertation were written by Dinesh Das, Department of Computer Sciences, The University of Texas at Austin, and extended by Bert Kay, James A. Bednar, and Ayman El-Khashab.